



Investigation of Passive Control Devices for Potential Application to a Launch Vehicle Structure to Reduce the Interior Noise Levels During Launch

Final Report for Stage 3A

Prepared For: AFOSR
Contract Number: F6256299M9179

Prepared by: Dr. Carl Olsard
Mr Rick C. Morgans
Dr. Anthony C. Zander
Professor Colin H. Hansen
Address: Department of Mechanical Engineering
The University of Adelaide
SA 5005
Australia

Contents

1	Executive Summary	4
2	Introduction	6
2.1	Background	6
2.2	Objectives	6
3	Modelling	12
3.1	Introduction	12
3.2	Tuned Mass Dampers	12
3.3	Helmholtz Resonators	15
3.4	Fully Coupled Model with Helmholtz Resonators and Tuned Mass Dampers	20
3.5	Acoustic Potential Energy	21
3.6	Boeing Cylinder	22
3.7	Cylinder Loading	22
4	Genetic Algorithms	30
4.1	Introduction	30
4.2	Condor Software	31
4.3	Synchronous Genetic Algorithm	32
4.4	Asynchronous Genetic Algorithm	32
5	Results	35
5.1	Testing of the GA Optimisation	35
5.1.1	Two PVADs Attached to a Large Box	35
5.1.2	Five PVADs Attached to the Boeing Cylinder	38
5.2	Performance vs Number of PVADs	40
5.3	Fixed Location and Free Parameters of 20 PVADs	50
5.4	Performance vs Volume of Helmholtz Resonators	54
5.5	Separating the Helmholtz Resonators and Tuned Mass Dampers	56
5.6	Robust Design	61
5.6.1	Performance vs Temperature	61
5.6.2	Performance vs Thickness of Shell	64
5.6.3	Performance vs Acoustic Damping	66
5.6.4	Performance with Highly Damped PVADs	68
5.6.5	Summary of Robust Designs	68

6	Conclusions	71
6.1	Summary	71
6.2	Future Work	71
6.2.1	Pseudo-static correction term	71
6.2.2	Modal Analysis	72
6.2.3	Revised Coding of the Genetic Algorithm	72
6.2.4	Validity of Modal Coupling with High Modal Density	72
6.3	Plans	73
6.3.1	Stage 3B	73
6.3.2	Stage 4	74
A	Dirac Delta Function Properties	75
B	PC Specifications of the Condor Pool	77
C	Symbols	78
C.1	Acronyms	78
C.2	List of Symbols	79
D	Checking the Models	80
D.1	Introduction	80
D.2	Tuned Mass Dampers	80
D.3	Helmholtz Resonators	88
D.3.1	Application of the acoustic load to the fluid	88
D.3.2	Single Helmholtz resonator	95
D.3.3	Two Helmholtz resonators	100
D.3.4	Multiple Helmholtz resonators	104
D.3.5	Placement of the device on the interior of the cavity	111
D.4	Fully Coupled Model	115
D.5	Calculation of Acoustic Potential Energy	121

Chapter 1

Executive Summary

The work described here is directed at optimising passive vibration and acoustic devices to minimise the transmission of low frequency rocket motor noise into structures that represent launch vehicle fairings. The work was divided into three stages and this report describes the results for the third stage of the work.

In the stage 1 study, the optimal configuration of a Passive Vibro-Acoustic Device (PVAD) mounted to the interior of a small cylinder was investigated. The PVAD consisted of an acoustic absorber and a vibration absorber (Tuned Mass Damper, TMD) in the one device, and it was mounted to a flexible aluminum panel used as the cylinder end cap. A mathematical framework was developed that used the modal analysis results from a finite element model to calculate the interior acoustic pressure and structural vibration levels, using a modal coupling method. The study found that the optimal PVAD design used the TMD essentially as a mass, as the uncoupled resonance frequency of the TMD was just below the upper bound of the frequency band of interest and that the optimal loudspeaker diaphragm configuration was highly lossy so that it reduced the modal amplitude of a single acoustic mode.

The objectives of the stage 2 task were to transfer the techniques developed in the stage 1 task to the optimisation of structures that more realistically represent real launch vehicles; in particular, a large composite cylinder under construction at Boeing, and a Representative Small Launch Vehicle Fairing (RSLVF). The modal coupling framework was extended to include the effects of the PVADs. A Genetic Algorithm was used to find optimum parameters for the PVADs that would reduce a cost function, the interior acoustic potential energy in this case. It was found that the calculation of the cost function took an excessive length of time, and attempts were made at reducing the calculation time by reducing the number of modes in the analysis. Vibration and acoustic modes that did not significantly contribute to the acoustic potential energy were removed from the matrices, which decreased the calculation time. However, this action resulted in a reduction in the number of possible optimum configurations where the vibro-acoustic energy would be re-arranged into poor radiating modes.

The work that was completed in this stage addresses some of the limitations found in stage 2.

- The mathematics for the coupling of the passive vibro-acoustic devices to the vibro-acoustic system was re-formulated. The new framework is easily extendable to multi-degree of freedom absorbers, which enables the inclusion of torsional vibration

for the tuned mass dampers, and multi-resonance Helmholtz resonators. This work was anticipated to commence in stage 4.

- A distributed computing network was created using the faculty's computing pool. The use of this computing network was vital for the optimisation work that was conducted in this stage. It takes about 6 minutes to calculate the cost function on a single 3.0 GHz Pentium PC. Most of the optimisations conducted in this stage of work involved conducting 18,000 cost function evaluations. Using a single computer this would have taken about 75 days per optimisation. The use of the faculty's distributed computing network reduced the calculation time to about 3 days - 25 times faster than using a single computer.
- Several analyses were conducted to investigate the sensitivity of the interior noise reduction to parameters such as shell thickness, air temperature, acoustic damping, total mass and volume of the passive vibro-acoustic devices. The results show that increasing the interior acoustic damping provides the greatest noise reduction compared to any method examined in this report.
- The genetic algorithm that was used for the optimisation in stage 2 used an integer representation for the chromosomes. The conclusion from the work was that an integer representation limited the evolution process, and that a binary string representation should be used. In this stage, a binary string representation was used, which does not appear to stunt the evolution process. The genetic algorithms developed in this stage were modified for use with the distributed computing network.

Chapter 2

Introduction

2.1 Background

The work discussed in the following report was undertaken as a result of the work done by Dr. Steve Griffin of the Air Force Research Lab at Kirtland AFB, New Mexico during his participation in the AFOSR Windows on Science program at the University of Adelaide, South Australia in 1998. The previous work involved an investigation of the application of active feedback control of launch vehicle structural vibration using radiation mode vibration levels as the cost function to minimise interior noise levels and led to the publication of three papers. The small benefit of active control, compared to the passive effect of the un-excited actuators attached to the structure has been the impetus behind the work conducted here, which is directed at optimising the passive effect of vibration reducing devices. The current work was divided into three stages and this report is primarily intended to provide the results for the third stage of the work.

2.2 Objectives

The following list contains the work plan of for Stage 3A (from 15 October 2002) shown in *italics*, and following each task is a bulleted list describing the work that was done.

1. Improve the Efficiency and Validity of the Design Optimisation Process.

The first task will be to update, document and simplify the fairing model code. This is required because; the modal model export routines are incompatible with the version of ANSYS used in undergraduate teaching (V6.1); the existing code is undocumented, making the operation difficult for new users; and the existing code structure makes modifications (such as multi-degree of freedom resonators) difficult.

Work completed:

- The routines for exporting the data from ANSYS V6.0 were re-written for ANSYS V7.0, and the documentation of the Matlab code was improved.
- The Matlab code was re-written to make use of structures - similar to objects in C++.

At the conclusion of Stage 2 of the project, it was shown that a Genetic Algorithm (GA) technique was able to optimise the placement and design parameters of Passive Vibro-Acoustic Devices (PVADs) in a model of a payload fairing. The payload fairing model used Finite Element Analysis (FEA) and modal coupling, together with a 'modal threshold' technique to remove modes that do not contribute to sound transmission, to improve the speed of simulation by 3 orders of magnitude over traditional fully coupled FEA (ANSYS).

However, it was found that the overall speed of the optimisation technique was excessively slow and of the order of 1 month on a Intel P3 800 MHz Computer. This was attributed mainly to the inefficient implementation of the GA, but other avenues for potential speed improvement were identified. The work in Stage 3A of the project will involve the application of various techniques to speed up the optimisation process to turn it into a useful scientific tool. An ideal target for the optimisation tool speed would be an 8-12 hour time frame, so that it can be run overnight. This target is not guaranteed, but the aim is to work for 5 months, working on tasks that appear to be most promising in improving speed. The work in this task will be restricted to the current Boeing cylinder model, but as the techniques used are general, they can be applied to all subsequent investigations.

Work completed:

- In Stage 2, the 'modal threshold' technique was used to eliminate modes that did not couple well from the structure to the acoustic cavity. By removing these inefficient radiation modes, the size of the matrices was reduced, and hence the response was calculated faster than if the poor radiation modes had been included in the matrices. However, by removing these modes one is reducing the search space. One possibility for noise reduction is that the parameters of the PVADs cause modal re-arrangement; that vibration energy is shifted from vibration modes that are efficient radiators into modes that are inefficient radiators. If the inefficient modes are removed from the matrices, then the GA will not be able to determine if modal rearrangement is a potential optimum. Hence for the Stage 3A work, the inefficient radiation modes are included in the matrices.

The most likely speed gain will be from an improved implementation of a GA, as this will reduce the number of different fairing model calculations required to produce an overall solution. The GA used in the previous stage was adapted from existing general code used to optimise the position of secondary sources in the active control of sound in enclosed spaces. Subsequent research has indicated that whilst this form of GA may be excellent for the 'device positioning' optimisation problem, it may not be the best choice for the 'parameter tuning' problem. Several alternate GA forms (such as binary encoded, real encoded, hybrid or micro) will be implemented and tested for the specific type of optimisation problem encountered.

Work completed:

- The GA that was used in Stage 2 used an integer representation of the chromosomes. One of the outcomes of the Stage 2 work was that in the future, one should use a binary representation for the chromosomes. In the work presented here, a publicly available GA toolbox for Matlab was used and the chromosomes were encoded as a binary string. The use of the binary string was an improvement over the integer

representation, which appeared to stagnate during optimisation, and was not the case with a binary representation.

If the GA code is found to run too slowly, then the code will be made to run in parallel using a distributed computing technique. Multiple computers throughout the department will be utilised. This will be implemented using remote procedure calls, and the speed gain should be proportional to the number of computers used.

Work completed:

- Following on from the recommendations at the end of the Stage 2 report, a parallel computing network was created using the faculty's computing pool and the publicly available Condor software. The computing pool has approximately 120 Pentium PC's available for cost function evaluations. Several parallel GA programs were developed that made use of the computing pool. The use of this parallel computing network reduced the time to evaluate the cost function by more than 20 times, compared using a single computer. The performance decrease caused by including the poor radiation modes in the matrices was offset by using the parallel computing network.
- The remote procedure calls cannot be easily implemented with the Condor software, and would be a software development project in itself. Hence this aspect was not attempted.

Another speed gain can be found by using fewer variables in the optimisation process. The results from the previous stages explained why the optimisation process tried to minimise the acoustic mass of the acoustic absorber, and maximise the mass of the structural absorber. By fixing the structural mass to a given budget, and the acoustic mass to values that can be physically achieved, the optimisation search space is greatly reduced.

Reducing the number of fairing model evaluations is likely to see the most speed improvement. In addition, reducing the time taken for an individual fairing model evaluation will help in the speed up task. Various approaches will be taken:

1. *The 'modal threshold' technique used previously to remove modes that do not contribute to sound transmission was found to work well. This technique needs to be further investigated to examine its limitations, and guidelines for its use need to be put in place.*
2. *A Matlab compiler is available to turn Matlab code into executable code. The compiler will be procured and tested to determine the speed gains from this approach.*
3. *If required, and if time permits, then a re-evaluation of the modal coupling technique will be undertaken. It may be possible to recast the modal coupling code to perform a coupled eigenvalue analysis, giving the coupled natural frequencies. This would allow the evaluation of the cost function to occur at only the natural frequencies rather than over a closely spaced range of frequencies, saving computing time.*

Work completed:

- As described previously, the ‘modal threshold’ technique eliminates potential optimum solutions and was not used in the Stage 3 work, as the limitations exceed the usefulness of this technique.
- The MATLAB compiler was purchased and used to compile the modal coupling software into stand-alone executable code. It was found that the stand-alone compiled version took about the same time to solve as the Just-In-Time compiler used in the interactive Matlab environment. However, the benefit of using the Matlab compiler to generate a stand-alone executable file is that the file can be distributed to each of the ‘slave’ PC’s that were used in the parallel computing network. If the modal coupling software had not been compiled, then one Matlab license must be held by each ‘slave’ computer during the calculation.
- About 2 weeks was spent attempting to develop alternative modal coupling software that takes less time to evaluate the cost function. The matrices used in the current modal coupling software are $N \times M$, where N is the number of nodes in the finite element model, and M is the number of acoustic modes. The number of nodes N is usually much greater than the number of modes M . Several papers exist that show the matrices formed for vibro-acoustic modal coupling can be reduced to $M \times M$, which means the matrices are smaller, and hence the time taken to invert the matrices is much quicker than inverting matrices with dimensions of $N \times N$. This work is incomplete and needs further investigation.
- Most of the time was spent reformulating and testing the mathematics and software implementation of the coupling of the PVADs to the vibro-acoustic system. The new mathematical framework is easily extendable to multiple-degree of freedom resonators, which was a task due to commence only in Stage 4.

Part of this task will be to generate a loading condition that excites non-axisymmetric modes. A plane wave incident at an angle, as used by Virginia Tech researchers [1] in their analytical modelling work, would be adequate for this.

Work completed:

- It was hoped that a more detailed loading condition would be available from work that is being conducted in parallel to this project at the University of Adelaide. However due to time constraints, an alternative loading condition was used, where a plane wave was incident on the cylinder, 90° to the axis of the cylinder.

(estimated duration: 5 months)

2. Boeing Cylinder Optimal and Sub-optimal Performance Evaluation.

Once the optimisation tool has been improved, the reduction of interior noise levels will be investigated for different design approaches for the Boeing cylinder. Performance will be assessed as a function of noise reduction, approximate added weight and required volume.

Work completed:

- optimisations were conducted for 10, 20 and 30 PVADs, where each Tuned Mass Damper weighed $0.45\text{kg} = 1\text{lb}$. The acoustic potential energy within the cylinder is plotted as a function of the number of PVADs, which is directly proportional to the mass, and the total volume occupied by all the PVADs.

A sensitivity analysis will be done to determine the sensitivity/robustness of the PVAD approach to changes in the structural dynamics and acoustics (resonance frequency and modal damping) as well as the local temperature. This sensitivity analysis will cover the range of variation expected in a normal launch vehicle structure.

Work completed:

- An optimisation was conducted for 20 PVADs arranged into 5 rings with 4 PVADs per ring, with the air temperature at 20°C .
- Using the parameters for the 20 PVADs obtained from the optimisation, the acoustic potential energy for the same configuration was calculated when the temperature was 0°C and 40°C .
- The acoustic potential energy within the cylinder was calculated for the nominal thickness, and ± 1 mm from the nominal thickness. Varying the shell thickness has the effect of varying the resonance frequencies of the structure.
- Using the parameters for the 20 PVADs obtained from the optimisation, the acoustic potential energy for the same configuration was calculated when the damping was varied from 2% to 10%.

In addition to investigating at the performance of PVADs, which represent vibration and acoustic absorbers at the same location, the possible benefit of separating them will be investigated. This will allow the acoustic absorbers to be at different locations to the vibration absorbers and it will be useful to determine whether there is a performance improvement for the same total added mass and volume.

Work completed:

- Using the parameters for the 20 PVADs obtained from the optimisation when the locations of the PVADs were fixed into 5 rings with 4 PVADs per ring, another optimisation was done where the locations of the HRs and the TMDs were not coincident.

It is possible that sub-optimal configurations, which have a slightly poorer performance, may be less sensitive to changes in the structural dynamics and acoustics than optimal absorber configurations. The sensitivity/robustness of sub-optimal configurations will thus be evaluated and the performance-to-cost (mass and volume) trade-space will also be evaluated.

(estimated duration: 4 months)

Work completed:

- This task is the same as described previously, which addresses the robustness of the design, such that the attenuation from the PVADs should be insensitive to variations in air temperature, and manufacturing and assembly tolerances.
- The performance-to-cost (mass and volume) was also addressed in a previous task.

3. Stage 3A report

(estimated duration: 1 month)

Work completed:

- This document describes the work that was completed for Stage 3A.

Chapter 3

Modelling

3.1 Introduction

In the previous two stages of work, mathematical models and software were developed to predict the sound pressure level inside an acoustic enclosure with flexible walls. A Finite Element model was created of the acoustic cavity and surrounding structure. A modal analysis was conducted on the structure uncoupled from the acoustic space, and a modal analysis was conducted on the acoustic space with rigid wall boundary conditions. The results from the two modal analyses were combined using a Matlab script to calculate the coupled response of the vibro-acoustic system. The Matlab code calculates the modal participation factors for the structure and the acoustic cavity, which can be used to calculate the acoustic pressure, or structural vibration at any node within the model. The modal participation factors can also be used to calculate the acoustic potential energy within the cavity, which was the cost function used in the optimisation.

A mathematical model was developed in Stage 2 to incorporate Helmholtz Resonators (HRs), and Tuned Mass Dampers (TMDs) into the modal coupling software. The devices were modelled as systems with one degree of freedom. The method of coupling the TMD to the vibro-acoustic model considered the damper as an equivalent mass-spring system in the acoustic domain and applied the derived impedance to the acoustic cavity. Similarly, the HR was converted into an equivalent structural mass-spring system, and an equivalent impedance was applied to the structural domain. This counter-intuitive concept is not easily extendable to multi-modal systems, which was the impetus for reformulating the method in this current stage. The mathematical framework developed here is easily extendable to multiple degree of freedom resonators, which means that torsional vibration can be considered for the TMDs, and multi-resonance HRs can be modelled.

3.2 Tuned Mass Dampers

A TMD is a device consisting of a spring and mass, whose resonance frequency is usually adjusted to coincide with a particular resonance frequency of structural vibration. The purpose of a TMD is to reduction vibration levels on the structural boundary enclosing the cavity with the intention of reducing the sound transmission. However, alternative uses for such a device include tuning it to an acoustic resonance frequency of a cavity, or even attempting to shift the energy of one vibration mode into another vibration mode

that has less ability to radiate sound into the cavity.

In ANSYS, an extension / compression spring is modelled using a COMBIN14 element, and the mass is modelled using a MASS21 element, which has only mass and no rotational inertia terms.

The method used to model the coupling of the TMD to the structure is similar to the method described in Ref [2] Chapter 9. The advantage of using this formulation, compared to the method used in Stage 2, is that it is extendable to multiple degree of freedom TMDs (can include 3 translational and 3 rotational degrees of freedom for motion, or multi-modal dampers), and multi-modal resonators.

The Stage 1 report [3] described the modal participation factors for the velocity of the structure are given by Eq. (46), which is

$$\mathbf{v} = \mathbf{Z}_b \mathbf{Z}_q^{-1} \mathbf{Q} + \mathbf{Z}_I^{-1} \mathbf{F} \quad (3.1)$$

where \mathbf{v} is the modal participation factor for velocity, \mathbf{Z}_b is the interior acoustic to structure transfer function, \mathbf{Z}_q is the acoustic modal input impedance matrix that couples the interior volume velocity sources and the regeneration of sound from sources to the structure back to the cavity, \mathbf{Q} is the modal volume velocity sources inside the cavity, \mathbf{Z}_I is structural modal input impedance matrix, and \mathbf{F} is the modal force applied to the structure.

Note that in the previous work [3–5] the modal participation factor for velocity \mathbf{v} , actually describes the displacement of the structure, and an additional $j\omega$ term is included in the formulation to convert it to velocity (see Eq. (12) in Ref [3]).

For the moment, we shall only consider the structural response due to forces applied to the structure, and ignore any cross-coupling, hence we are only interested in the last term in Eq. (3.1). This equation can be re-arranged to

$$\mathbf{Z}_I \mathbf{v} = \mathbf{F} \quad (3.2)$$

where the modal force comprises the external forces applied to the structure \mathbf{F}_{ext} and the forces due to the TMDs \mathbf{F}_{TMD} . Hence the force applied to the structure can be written as $\mathbf{F} = \mathbf{F}_{\text{ext}} + \mathbf{F}_{\text{TMD}}$.

A model of a TMD is shown in Figure 3.1, where m_1 is the mass of the damper, k_1 is the stiffness, F_1 is the harmonic force directly applied to the mass, which is typically zero, F_c is the force at the attachment point between the spring and the structure. Note at this stage the model does not have any damping included; however damping terms can be added later without complication. The equations of motion for the TMD can be written succinctly in matrix form as

$$\begin{bmatrix} k_1 - m_1 \omega^2 & -k_1 \\ -k_1 & k_1 \end{bmatrix} \begin{bmatrix} x_1 \\ x_c \end{bmatrix} = \begin{bmatrix} F_1 \\ F_c \end{bmatrix} \quad (3.3)$$

where k_1 is the spring stiffness, m_1 is the mass, F_1 is the force applied directly to the TMD which is usually $F_1 = 0$, ω is the driving frequency in radians / sec, x_1 is the displacement of the TMD, x_c is the displacement of the connection of the isolator to the structure, and F_c is the force applied by the structure to the TMD, which is equal and opposite to the force from the spring.

One can assume that at the point of attachment, the displacement of the structure and the position of the end of the spring are the same. If the dynamics of the structure

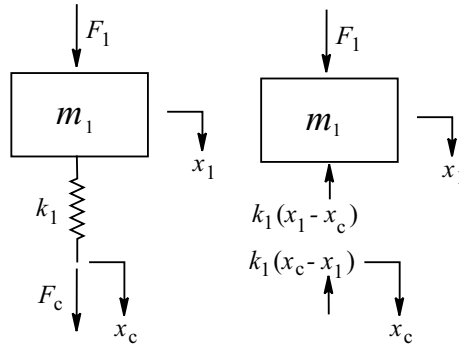


FIG. 3.1: Model of a one degree of spring-mass system, to be used as a Tuned Vibration Damper (TMD).

are introduced into Eq. (3.3), then the equations of motion can be written as

$$\begin{bmatrix} Z_0 + k_1 & -k_1[\boldsymbol{\psi}_1] \\ -[\boldsymbol{\psi}_1]^T k_1 & \mathbf{Z}_I + [\boldsymbol{\psi}_1]^T k_1 [\boldsymbol{\psi}_1] \end{bmatrix} \begin{bmatrix} x_1 \\ \mathbf{v} \end{bmatrix} = \begin{bmatrix} \mathbf{0} \\ \mathbf{F}_{\text{ext}} \end{bmatrix} \quad (3.4)$$

where $[\boldsymbol{\psi}_1]$ is the structural mode shape vector evaluated at the connection point of the TMD, T is the matrix transpose operator, and $Z_0 = -\omega^2 m_1$ is the impedance of the TMD. Note that the matrix $[\boldsymbol{\Psi}]$ contains all the mode shapes for all the nodes and has dimensions $(N_s \text{ nodes} \times N_s)$, the number of structural nodes \times the number of structural modes. Hence, each row of the matrix contains N_s entries for the normal structural displacement at each mode, and so the vector $[\boldsymbol{\psi}_1]$ has dimensions $(1 \times N_s)$. Eq. (3.4) can be extended to the general case, where there are multiple TMDs, and is given by [2, 6]

$$\begin{bmatrix} \mathbf{A}_{11} & \mathbf{A}_{12} \\ \mathbf{A}_{21} & \mathbf{A}_{22} \end{bmatrix} \begin{bmatrix} \mathbf{D}_0 \\ \mathbf{v} \end{bmatrix} = \begin{bmatrix} \mathbf{0} \\ \mathbf{F}_{\text{ext}} \end{bmatrix} \quad (3.5)$$

where \mathbf{A}_{11} is a $(N_{\text{TMD}} \times N_{\text{TMD}})$ matrix that has elements only on the main diagonal of

$$\mathbf{A}_{11} = \begin{bmatrix} k_1^{\text{TMD}} - m_1^{\text{TMD}} \omega^2 & & \\ & \ddots & \\ & & k_J^{\text{TMD}} - m_J^{\text{TMD}} \omega^2 \end{bmatrix} \quad (3.6)$$

\mathbf{A}_{12} is a $(N_{\text{TMD}} \times N_s)$ matrix given by

$$\mathbf{A}_{12} = \begin{bmatrix} -k_1^{\text{TMD}} \boldsymbol{\psi}_{11} & \cdots & -k_1^{\text{TMD}} \boldsymbol{\psi}_{1N_s} \\ \vdots & \ddots & \vdots \\ -k_J^{\text{TMD}} \boldsymbol{\psi}_{J1} & \cdots & -k_J^{\text{TMD}} \boldsymbol{\psi}_{JN_s} \end{bmatrix} \quad (3.7)$$

\mathbf{A}_{21} is a $(N_s \times N_{\text{TMD}})$ matrix given by

$$\mathbf{A}_{21} = \begin{bmatrix} -[\boldsymbol{\psi}_{11}]^T k_1^{\text{TMD}} & \cdots & -[\boldsymbol{\psi}_{J1}]^T k_J^{\text{TMD}} \\ \vdots & \ddots & \vdots \\ -[\boldsymbol{\psi}_{1N_s}]^T k_1^{\text{TMD}} & \cdots & -[\boldsymbol{\psi}_{JN_s}]^T k_J^{\text{TMD}} \end{bmatrix} \quad (3.8)$$

\mathbf{A}_{22} is a $(N_s \times N_s)$ matrix given by

$$\mathbf{A}_{22} = \mathbf{Z}_I + [\boldsymbol{\psi}_j]^T k_j^{\text{TMD}} [\boldsymbol{\psi}_j] \quad (3.9)$$

where $[\psi_j]$ is the mode shape vector at the J th attachment point of the TMD to the structure, m_j^{TMD} and k_j^{TMD} are the mass and stiffness of the J th TMD.

In this mathematical framework one can model the TMDs as 6-DOF devices that can vibrate along 3 translational axes, and 3 rotational axes, as shown in Ref [2, 6]. It is possible to include the effect of moments on the structure by converting them into force - moment couples, as shown in Appendix A.

The equations derived thus far have not included damping terms. Damping can be included by using a structural loss factor, so that the stiffness value for the TMD becomes a complex number. Hence the complex stiffness can be written as $k_j^{\text{TMD}} = k_j^{\text{TMD}}(1 + j\eta)$, where η is the structural loss factor.

The modal participation factors for the structure can be calculated and the displacement of the TMDs are calculated by pre-multiplying Eq. (3.5) by the inverse of the \mathbf{A} matrix. Once these factors have been found, the response of the structure at any nodal location can be calculated.

The mathematical model described above was realised in Matlab and is compared with an equivalent ANSYS model in Appendix D.2.

3.3 Helmholtz Resonators

A Helmholtz resonator is used to reduce the noise inside cavity by presenting an impedance change to the cavity. A Helmholtz resonator is a volume of fluid attached by a small neck to a larger cavity or a duct, that acts to attenuate noise in an acoustic space by ‘dissipating’ energy, as shown in Figure 3.2. The volume of fluid in the neck of the resonator acts as mass, and the large volume of fluid acts as a compliant spring. Hence one can think of a Helmholtz resonator as a piston attached to a cavity, with the dynamics of an equivalent mass-spring system, as shown in Figure 3.3.

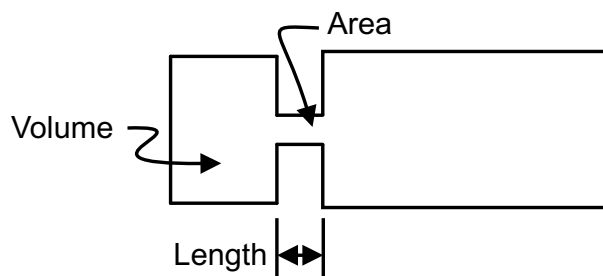


FIG. 3.2: Helmholtz resonator attached to a cavity.

The mathematical framework derived here for the Helmholtz resonator is very similar to the framework derived for the TMD described in section 3.2.

The modelling of Helmholtz resonators involves creating a mathematical model of these devices, and developing an independent method to check that the mathematical model correctly predicts the response. It was decided early in the project that ANSYS would be used to conduct a full fluid-structure interaction analysis and the results would be compared with the results from the Matlab code of the modal coupling theory.

The development of the framework for the Helmholtz resonator was conducted in 3 stages as follows:

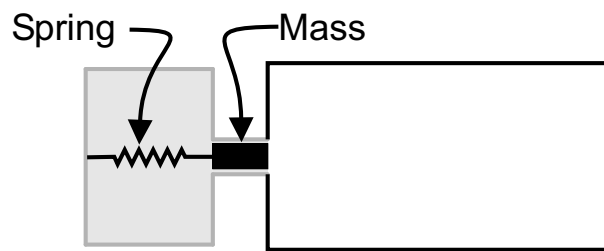


FIG. 3.3: A Helmholtz resonator attached to a cavity can be thought of as a mass-spring system.

Applying a Volume Velocity to the Cavity The first stage was to develop methods in ANSYS to apply a volume velocity to a model of a large cavity. An equivalent mathematical model that used modal summation (which is used in the modal coupling method used in this work) was developed and compared with the predictions made using ANSYS. Two methods were developed in ANSYS to model the application of a volume velocity source to a large cavity. The first involves using elements that are capable of coupling a fluid and structure - Fluid-Structure Interaction (FSI) elements. The second method is to apply a volume acceleration source boundary condition to a node, called a FLOW condition in ANSYS, which is the time derivative of a volume velocity source, a familiar term to acousticians. Comparisons were made between these three methods: the Matlab modal coupling software, a FLOW boundary condition in ANSYS, and using 4 Fluid-Structure Interaction (FSI) elements in ANSYS. The results are described in Appendix D.3.1, and shows that each method applies a slightly different load to the cavity and that the number of modes included in the analysis is an important consideration.

Modelling the Mass-Spring System As described previously, a HR can be mathematically modelled as a mass - spring system. In ANSYS, the HR can be modelled using 4 FSI elements that are attached to the acoustic elements of a large cavity, with the central node having a point mass element, and the mass is connected to an elastic spring. A more detailed explanation of this modelling method is included later in this section. Appendix D.3.2 contains the results of the comparison of a single HR attached to a large cavity predicted using the Matlab modal coupling software and ANSYS. The results show that both methods predict the same sound pressure level inside the large cavity, and hence the Matlab modal coupling software correctly predicts the response of the system.

Multiple Helmholtz Resonators Once the single HR case was tested, multiple HRs were modelled. Appendix D.3.3 and D.3.4 show the comparison of the sound pressure level inside a large cavity with two and three HRs attached to the cavity, respectively, predicted using ANSYS and the Matlab modal coupling software. The results show that both methods predict the same values, which means that the Matlab modal coupling software correctly predicts the response of the system.

Note that in ANSYS, a FLOW boundary condition can be applied to an acoustic cavity to provide an acoustic excitation source. This FLOW boundary condition can be converted into an equivalent volume velocity source, Q , for use in the Matlab modal

coupling software using the following expression

$$Q = \frac{\text{FLOW}}{j\omega\rho} \quad (3.10)$$

where ρ is the density of the gas.

The pressure inside the cavity for the coupled equations of motion derived previously [3, Eq. (45)] is

$$\mathbf{p} = \mathbf{Z}_q^{-1}\mathbf{Q} + \mathbf{Z}_a\mathbf{Z}_I^{-1}\mathbf{F} \quad (3.11)$$

where \mathbf{Z}_a is structure to acoustic interior transfer function, and all the remaining terms have been described in section 3.2. The terms on the right hand side of Eq. (3.11) relate to the transfer of energy from the structure to the acoustic cavity. For the moment we shall ignore these terms and develop the equations for Helmholtz resonators attached to the acoustic cavity. The modal volume velocity sources inside the cavity comprise the point sources from Helmholtz resonator, \mathbf{Q}_J^{HR} , and from internal sources such as speakers or other noise generating devices $\mathbf{Q}_K^{\text{int}}$; hence the total volume velocity inside the cavity is given by

$$\mathbf{Q}^T = \sum_{J=1}^{N_{\text{HR}}} \mathbf{Q}_J^{\text{HR}} + \sum_{K=1}^{N_{\text{int}}} \mathbf{Q}_K^{\text{int}} \quad (3.12)$$

where N_{HR} is the number of Helmholtz resonators, and N_{int} is the number of interior acoustic sources. Note that the volume velocity terms are modal amplitudes such that

$$\mathbf{Q}_K^{\text{int}} = q_K^{\text{int}}[\phi_K] \quad (3.13)$$

where q_K^{int} is the amplitude of the K th internal volume velocity source, and $[\phi_K]$ is the vector of the acoustic mode shape at the location of the K th internal volume velocity source. Eq. (3.11) can be re-arranged into (omitting the cross coupling terms for the moment)

$$\mathbf{Z}_q\mathbf{p} = \mathbf{Q}^T \quad (3.14)$$

The equation of motion for a simple mass-spring system shown in Figure 3.4 is

$$-\omega^2mx = F - kx \quad (3.15)$$

where F is the force applied by the back pressure from the cavity, k is the equivalent spring stiffness of the compliant volume, and m is the equivalent mass of the volume of fluid inside the neck of the resonator. These terms are given by [7]

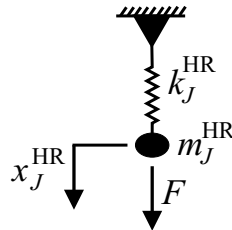


FIG. 3.4: A Helmholtz resonator attached to a cavity can be thought of as a mass-spring system.

$$F = P_J A_J^{\text{HR}} \quad (3.16)$$

$$k = \frac{\rho c^2 A_{\text{neck}}^2}{V_{\text{HR}}} \quad (3.17)$$

$$m = \rho A_{\text{neck}} L_{\text{eff}} \quad (3.18)$$

where A_J^{HR} is the area associated with the node attaching the spring to the acoustic cavity, P_J is the nodal pressure at the attachment point, V_{HR} is the volume of the Helmholtz resonator, A_{neck} is the cross sectional area of the neck, L_{eff} is the effective length of the neck given by $L_{\text{eff}} = L_{\text{neck}} + 1.7a$, where L_{neck} is the length of the neck, and a is the radius of the neck.

The equations that govern the acoustic behaviour of the cavity are given by

$$\mathbf{Z}_q \mathbf{p} = \sum_{J=1}^{N_{\text{HR}}} \mathbf{Q}_J^{\text{HR}} + \sum_{K=1}^{N_{\text{int}}} \mathbf{Q}_K^{\text{int}} \quad (3.19)$$

where

$$\mathbf{Q}_J^{\text{HR}} = j\omega A_J^{\text{HR}} [\phi_J]^T \quad (3.20)$$

In the ANSYS software, a Helmholtz resonator can be modelled as a spring for the compliant volume (COMBIN14 element), with the displacement fixed at one end, and the other end attached to a node that is a part of the 4 Fluid-Structure Interaction (FSI) elements, as shown in Figure 3.5. The FSI elements have 4 degrees of freedom: displacements along the x, y, z axes and pressure. The displacements for all the nodes on the exterior of the elements were fixed, and only the central node attached to the spring was allowed to move. This effectively creates a piston that can move the fluid and generate a volume velocity sound source.

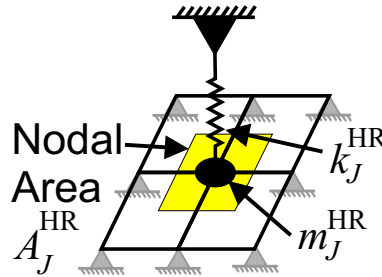


FIG. 3.5: Model of a Helmholtz resonator in ANSYS showing the mass, spring, and the 4 FSI elements.

The equations of motion for the HR can be written succinctly in matrix form as

$$\begin{bmatrix} k_J^{\text{HR}} - m_J^{\text{HR}} \omega^2 & -A_J^{\text{HR}} \phi_J \\ -j\omega A_J^{\text{HR}} [\phi_J]^T & \mathbf{Z}_q \end{bmatrix} \begin{bmatrix} x_J^{\text{HR}} \\ \mathbf{p} \end{bmatrix} = \begin{bmatrix} \mathbf{0} \\ \mathbf{Q}_{\text{int}} \end{bmatrix} \quad (3.21)$$

These equations can be modified from the case of a single Helmholtz resonator to multiple Helmholtz resonators attached to the cavity. Eq. (3.21) is expanded to

$$\begin{bmatrix} \mathbf{B}_{11} & \mathbf{B}_{12} \\ \mathbf{B}_{21} & \mathbf{B}_{22} \end{bmatrix} \begin{bmatrix} \mathbf{x}^{\text{HR}} \\ \mathbf{p} \end{bmatrix} = \begin{bmatrix} \mathbf{0} \\ \mathbf{Q}_{\text{int}} \end{bmatrix} \quad (3.22)$$

where \mathbf{B}_{11} is a $(N_{\text{HR}} \times N_{\text{HR}})$ diagonal matrix that has entries of

$$\mathbf{B}_{11} = \begin{bmatrix} k_1^{\text{HR}} - m_1^{\text{HR}}\omega^2 & & \\ & \ddots & \\ & & k_J^{\text{HR}} - m_J^{\text{HR}}\omega^2 \end{bmatrix} \quad (3.23)$$

\mathbf{B}_{12} is a $(N_{\text{HR}} \times N_c)$ matrix given by

$$\mathbf{B}_{12} = \begin{bmatrix} -A_1^{\text{HR}}\phi_{11} & \cdots & -A_1^{\text{HR}}\phi_{1N_c} \\ \vdots & \ddots & \vdots \\ -A_J^{\text{HR}}\phi_{J1} & \cdots & -A_J^{\text{HR}}\phi_{JN_c} \end{bmatrix} \quad (3.24)$$

\mathbf{B}_{21} is a $(N_c \times N_{\text{HR}})$ matrix given by

$$\mathbf{B}_{21} = \begin{bmatrix} -j\omega A_1^{\text{HR}}[\phi_{11}]^T & \cdots & -j\omega A_J^{\text{HR}}[\phi_{J1}]^T \\ \vdots & \ddots & \vdots \\ -j\omega A_1^{\text{HR}}[\phi_{1N_c}]^T & \cdots & -j\omega A_J^{\text{HR}}[\phi_{JN_c}]^T \end{bmatrix} \quad (3.25)$$

\mathbf{B}_{22} is a $(N_c \times N_c)$ matrix given by

$$\mathbf{B}_{22} = \mathbf{Z}_q \quad (3.26)$$

It is possible to extend the use of this model to cover the case where the area of the throat of the Helmholtz resonator covers several nodes, as shown in Figure 3.6. The

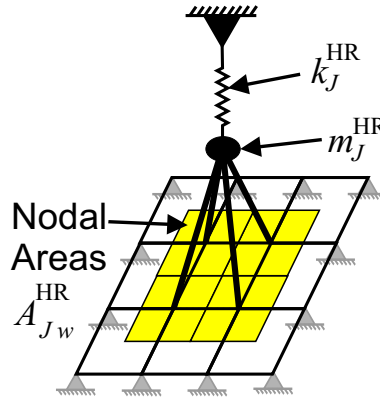


FIG. 3.6: Model of a Helmholtz resonator with several nodes contributing to the pressure impinging on the throat of the resonator.

pressure exerted by the cavity on the throat of the resonator is the sum of the nodal pressure times the area associated with each node, hence Eqs. (3.24) and (3.25) become

$$\mathbf{B}_{12} = - \sum_{J=1}^{N_{\text{HR}}} \sum_{w=1}^{N_{\text{nodes}}} A_{Jw}^{\text{HR}} \phi_{Jw} \quad (3.27)$$

$$\mathbf{B}_{21} = -j\omega \sum_{J=1}^{N_{\text{HR}}} \sum_{w=1}^{N_{\text{nodes}}} A_{Jw}^{\text{HR}} [\phi_{Jw}]^T \quad (3.28)$$

where A_{Jw}^{HR} is the nodal area associated with the throat of the resonator, and there are a total of $w = 1, \dots, N_{\text{nodes}}$ nodal areas that comprise the total area across the throat of the J th Helmholtz resonator. Similarly, ϕ_{Jw} is the acoustic mode shape at the w th node that is a part of the J th resonator.

The mathematical model described above was realised in Matlab, and was compared with an equivalent ANSYS model. The comparison is described in Appendix D.3 and shows that both methods predict the same values, which means that the Matlab modal coupling software correctly predicts the response of the system.

3.4 Fully Coupled Model with Helmholtz Resonators and Tuned Mass Dampers

Section 3.2 described a mathematical model to couple TMDs to a structure, and section 3.3 described a mathematical model to couple HRs to an acoustic cavity. The next step is to develop a mathematical model to couple both the TMDs and HRs to a vibro-acoustic system, which is described in this section. The fully coupled vibro-acoustic model will account for the influence of the TMDs on the structural vibration and the acoustic response, and will account for the the influence of the HRs on the acoustic response and the structural vibration.

Taking Eqs. (45) and (46) from the Stage 2 report, and re-arranging them gives

$$\mathbf{Z}_q \mathbf{p} = \mathbf{Q} + \mathbf{Z}_q \mathbf{Z}_a \mathbf{Z}_I^{-1} \mathbf{F} \quad (3.29)$$

$$\mathbf{Z}_I \mathbf{v} = \mathbf{F} + \mathbf{Z}_I \mathbf{Z}_b \mathbf{Z}_q^{-1} \mathbf{Q} \quad (3.30)$$

The coupled equations of motion for the structure and the TMD were presented in section 3.2 and can be written in matrix form as

$$\begin{bmatrix} \mathbf{A}_{11} & \mathbf{A}_{12} \\ \mathbf{A}_{21} & \mathbf{A}_{22} \end{bmatrix} \begin{bmatrix} \mathbf{D}_0 \\ \mathbf{v} \end{bmatrix} = \begin{bmatrix} \mathbf{0} \\ \mathbf{F}_{\text{ext}} + \mathbf{Z}_I \mathbf{Z}_b \mathbf{Z}_q^{-1} (\mathbf{Q}_{\text{int}} + \mathbf{Q}_{\text{HR}}) \end{bmatrix} \quad (3.31)$$

The coupled equations for the acoustic cavity and the Helmholtz resonators presented in section 3.3 are

$$\begin{bmatrix} \mathbf{B}_{11} & \mathbf{B}_{12} \\ \mathbf{B}_{21} & \mathbf{B}_{22} \end{bmatrix} \begin{bmatrix} \mathbf{x}_0 \\ \mathbf{p} \end{bmatrix} = \begin{bmatrix} \mathbf{0} \\ \mathbf{Q}_{\text{int}} + \mathbf{Z}_q \mathbf{Z}_a \mathbf{Z}_I^{-1} (\mathbf{F}_{\text{ext}} + \mathbf{F}_{\text{TMD}}) \end{bmatrix} \quad (3.32)$$

These matrices can be coupled to a larger matrix as

$$\begin{bmatrix} \begin{bmatrix} \mathbf{A}_{11} & \mathbf{A}_{12} \\ \mathbf{A}_{21} & \mathbf{A}_{22} \end{bmatrix} & \mathbf{0} & \mathbf{0} \\ \mathbf{0} & \mathbf{0} & \begin{bmatrix} \mathbf{B}_{11} & \mathbf{B}_{12} \\ \mathbf{B}_{21} & \mathbf{B}_{22} \end{bmatrix} \\ \mathbf{B}_{41} & \mathbf{B}_{42} & \begin{bmatrix} \mathbf{B}_{11} & \mathbf{B}_{12} \\ \mathbf{B}_{21} & \mathbf{B}_{22} \end{bmatrix} \end{bmatrix} \begin{bmatrix} \mathbf{D}_0 \\ \mathbf{v} \\ \mathbf{x}_0 \\ \mathbf{p} \end{bmatrix} = \begin{bmatrix} \mathbf{0} \\ \mathbf{F}_{\text{ext}} + \mathbf{Z}_I \mathbf{Z}_b \mathbf{Z}_q^{-1} \mathbf{Q}_{\text{int}} \\ \mathbf{0} \\ \mathbf{Q}_{\text{int}} + \mathbf{Z}_q \mathbf{Z}_a \mathbf{Z}_I^{-1} \mathbf{F}_{\text{ext}} \end{bmatrix} \quad (3.33)$$

where \mathbf{A}_{11} , \mathbf{A}_{12} , \mathbf{A}_{21} , \mathbf{A}_{22} and \mathbf{B}_{11} , \mathbf{B}_{12} , \mathbf{B}_{21} , \mathbf{B}_{22} were defined previously, and

$$\mathbf{A}_{23} = \mathbf{Z}_I \mathbf{Z}_b \mathbf{Z}_q^{-1} (-j\omega A_J^{\text{HR}} [\phi_J]^T) \quad (3.34)$$

$$\mathbf{A}_{24} = \mathbf{0} \quad (3.35)$$

$$\mathbf{B}_{41} = \mathbf{Z}_q \mathbf{Z}_a \mathbf{Z}_I^{-1} (-[\psi_J]^T k_J^{\text{TMD}}) \quad (3.36)$$

$$\mathbf{B}_{42} = \mathbf{Z}_q \mathbf{Z}_a \mathbf{Z}_I^{-1} [\boldsymbol{\psi}_J]^T k_J^{\text{TMD}} \quad (3.37)$$

The dimensions of the elements of the matrices in Eq.(3.33) are

$$\begin{bmatrix} \begin{bmatrix} (N_{\text{TMD}} \times N_{\text{TMD}}) & (N_{\text{TMD}} \times N_s) \\ (N_s \times N_{\text{TMD}}) & (N_s \times N_s) \end{bmatrix} & \begin{bmatrix} (N_{\text{TMD}} \times N_{\text{HR}}) & (N_{\text{TMD}} \times N_c) \\ (N_s \times N_{\text{HR}}) & (N_s \times N_c) \end{bmatrix} \\ \begin{bmatrix} (N_{\text{HR}} \times N_{\text{TMD}}) & (N_{\text{HR}} \times N_s) \\ (N_c \times N_{\text{TMD}}) & (N_c \times N_s) \end{bmatrix} & \begin{bmatrix} (N_{\text{HR}} \times N_{\text{HR}}) & (N_{\text{HR}} \times N_c) \\ (N_c \times N_{\text{HR}}) & (N_c \times N_c) \end{bmatrix} \end{bmatrix} \begin{bmatrix} (N_{\text{TMD}} \times 1) \\ (N_s \times 1) \\ (N_{\text{HR}} \times 1) \\ (N_c \times 1) \end{bmatrix} = \begin{bmatrix} (N_{\text{TMD}} \times 1) \\ (N_s \times 1) \\ (N_{\text{HR}} \times 1) \\ (N_c \times 1) \end{bmatrix} \quad (3.38)$$

where N_{TMD} , N_{HR} , N_s , N_c are the number of Tuned Mass Dampers, Helmholtz resonators, number of modes included in the structural and acoustic analysis, respectively.

The mathematical model described above was realised in Matlab, and the testing of the mathematics and software is described in Appendix D.4.

3.5 Acoustic Potential Energy

As mentioned previously, the cost function that is to be minimised is the Acoustic Potential Energy (APE) within the cavity. The APE is calculated using the modal participation factors. Appendix D.5 describes the testing of this method.

To enable comparison of APE from different systems, the APE is normalised using the following expression

$$\overline{\text{APE}} = 10 \log_{10} \left(\frac{\Delta f_1 \times \sum_{i=1}^{i_{\max}} \text{APE}(f_i)}{\Delta f_2} \right) \quad (3.39)$$

where $\text{APE}(f)$ is the Acoustic Potential Energy evaluated at frequency f , Δf_1 is the frequency spacing using for the analysis, and Δf_2 is the frequency range over which the analysis was conducted.

3.6 Boeing Cylinder

The eventual goal of this project is to develop methods to aid in the design of vibro-acoustic treatments for the payload bay of a rocket. Experimental work is being conducted at Boeing, Virginia Technology, and at the Kirtland airforce base. The experimental model is a large cylindrical structure made of composite material that was built at Boeing. Later in the project, the experimental work and theoretical models will focus on a Representative Small Launch Vehicle Fairing (RSLVF). However in this stage we are only considering the Boeing cylinder.

A model of the Boeing cylinder is shown in Figures 3.7 and 3.8, which is similar to the model used in the Stage 2 work. The only difference is that the average mesh density spacing was decreased to 0.08m, whereas in the Stage 2 work the average mesh density was 0.8m. Based on the rule-of-thumb guideline for acoustic finite element analyses, one should have an element spacing of 6 elements per wavelength [8, 9]. Using this guide, the model should be suitable for analyses up to $(344/(0.08 \times 6) =) 716\text{Hz}$.

However, experience has shown [4] that when using the modal coupling method, one should conduct the modal analyses up to 2 octaves higher than the frequency range of interest. For example, if the frequency range of interest is 300Hz, then one should include all modes up to 1200Hz. If this guideline were to be followed, the mesh spacing would need to be about 0.045m, which means that the finite element model would be about 8 times as large, and the Matlab modal coupling software would take much longer to solve the model used for this work. It is recognised that this is a limitation of the current work. In the future, work should be done to find or develop modal coupling algorithms that use smaller matrices, so that the cost function evaluation times are shorter than currently.

3.7 Cylinder Loading

Two types of cylinder loading were considered. The first loading case a fictitious loading condition where every node on the circumference of the Boeing cylinder has a 1N radial force, which equates to a sound pressure level of 139dB re $20\mu\text{Pa}$, based on the nodal area.

One of the concerns raised by the reviewers of the previous reports was that this type of loading may not excite the odd modes of the cylinder. In reality, the launch vehicle sits on a launch pad that has a concrete chute to direct the rocket motor exhaust in a line to one or two sides of the rocket. The second loading case tries to address some of these issues.

The second load case has the cylinder loaded by a plane wave of sound from one direction, as shown in Figure 3.9. Some analysis was conducted in Stage 1 to show the pressure distribution from a plane wave impinging on a sphere. The load case presented here does not attempt to mimic these results, but is rather a more simplified loading pattern used to demonstrate the use of the modelling techniques and the GA approach to determine the optimum acoustic and vibration treatments.

In a finite element sense, the surface of the cylinder can be discretised into small elements that have nodes as the vertices of the area. As the plane wave reaches the surface of the cylinder, the pressure acts on an elemental area. This pressure can be converted into a nodal force, based on the area associated with each node, which can be applied to the modal model. The pressure that acts on the surface of the cylinder is

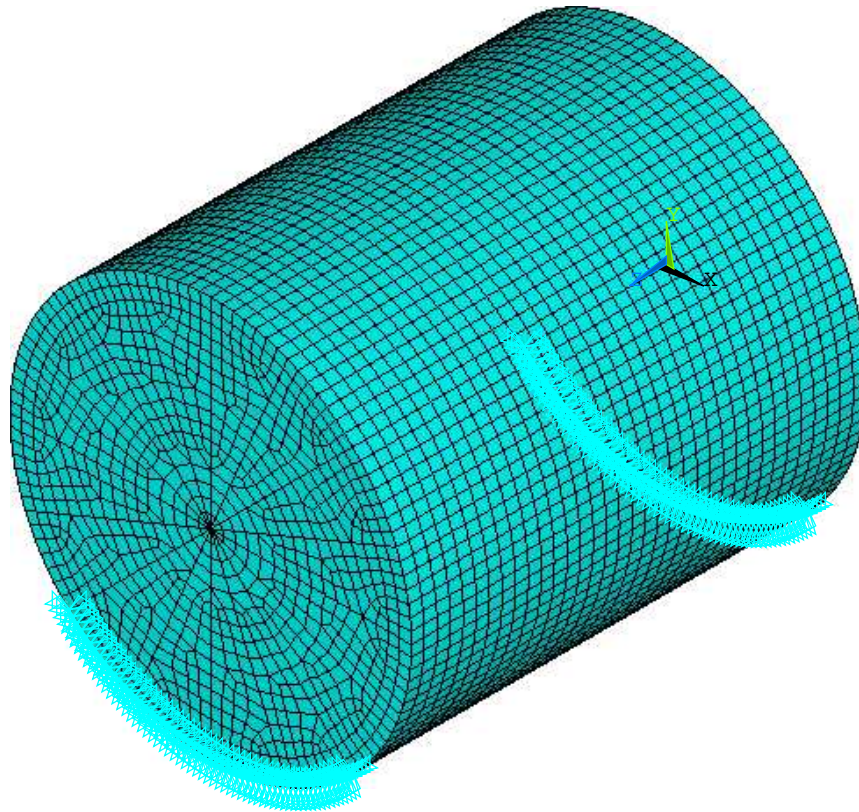


FIG. 3.7: ANSYS model of the Boeing cylinder showing the acoustic space.

a function of the area that faces the incoming plane wave. Hence the nodes that have normals facing the impinging direction have the greatest pressure excitation amplitude, and the nodes that are at 90 degrees to the impinging direction have zero excitation pressure, as the plane wave is travelling tangentially to the surface of the cylinder. We shall assume that there is no diffraction around the cylinder, and only half of the cylinder is loaded. In reality, one would expect some diffraction around the cylinder, however we shall assume this is of less importance than the waves that directly strike the cylinder and will be ignored. Another effect that is ignored is the external re-radiation of the cylinder, as this is a second order effect.

Figure 3.10 shows a diagram of the important features of the mathematical model for the pressure loading on the cylinder. The pressure is assumed to vary sinusoidally around the circumference of the cylinder, due to the area that is normal to the impinging direction. Hence the nodal pressure is given by

$$F_{\text{node}} = P(\theta)A_{\text{node}} \cos \theta \quad (3.40)$$

where F_{node} is the nodal force, $P(\theta)$ is the pressure at angle θ , and A_{node} is the nodal area.

The distance travelled by a plane wave between the surface closest to the speaker array and at a point on the circumference on the cylinder is

$$x_{\text{delay}} = R(1 - \cos \theta) \quad (3.41)$$

The wavelength of sound is $\lambda = c/f$, where c is the speed of sound, f is the frequency in Hertz. If one assumes that the sound pressure level varies sinusoidal along the wavelength,

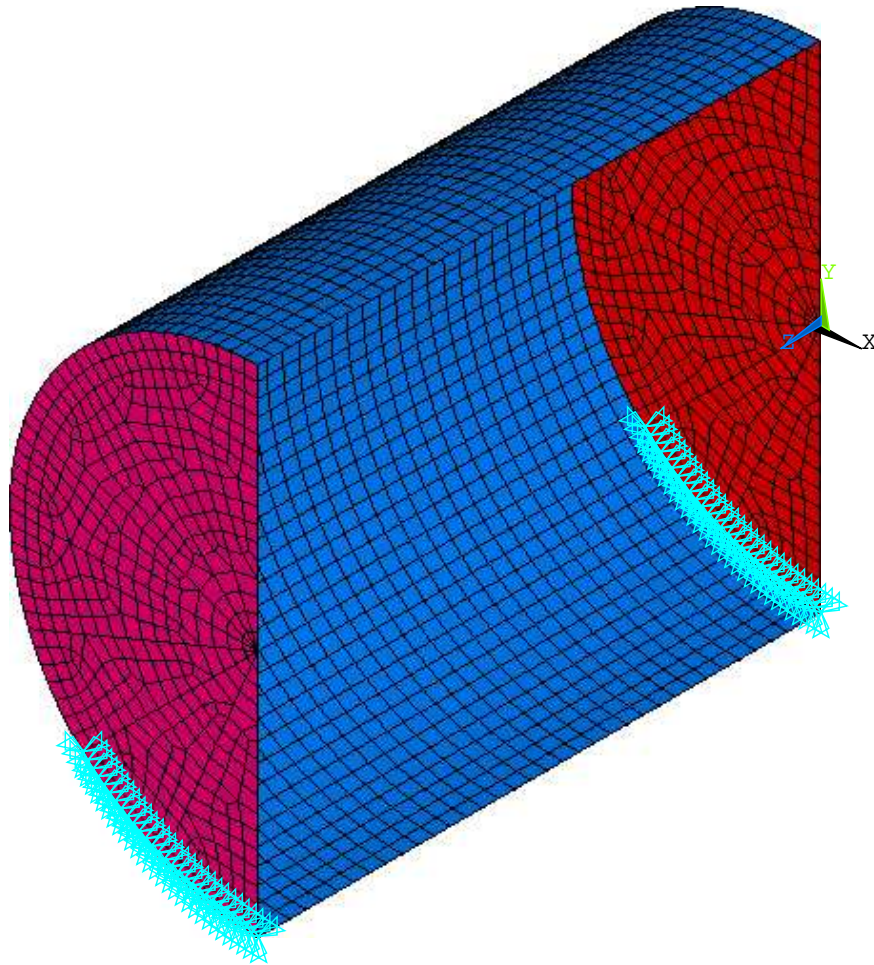


FIG. 3.8: ANSYS model of the Boeing cylinder, showing a cross section through the structure.

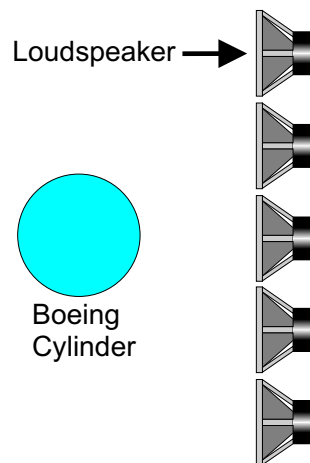


FIG. 3.9: The Boeing cylinder with a plane wave incident from one direction.

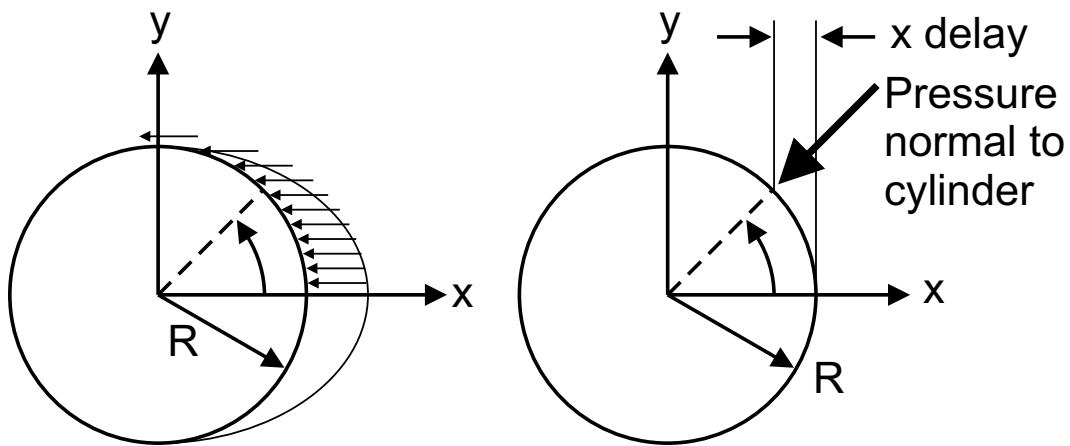


FIG. 3.10: Diagram of the plane wave striking the cylinder.

then assuming the maximum amplitude occurs when the wave strikes the edge of the cylinder closest to the speakers, then one can assume that the pressure will vary cosinusoidally as

$$P(\theta) = P_0 \left[\cos \left(\frac{2\pi x_{\text{delay}}}{\lambda} \right) + j \sin \left(\frac{2\pi x_{\text{delay}}}{\lambda} \right) \right] \quad (3.42)$$

where P_0 is the pressure on the surface of the cylinder that is closest to the speaker array. It was assumed that the sound pressure level was 140dB, which means $P_0 = 10^{(140/20)} \times (20 \times 10^{-6}) = 200\text{Pa}$. Hence the nodal force is found by combining Eqs. (3.40), (3.41), and (3.42) to give

$$F_{\text{node}} = P_0 A_{\text{node}} (\cos \theta) \left[\cos \left(\frac{2\pi R(1 - \cos \theta)}{\lambda} \right) + j \sin \left(\frac{2\pi R(1 - \cos \theta)}{\lambda} \right) \right] \quad (3.43)$$

Using Eq. (3.40) one can show the distribution of nodal loads around the circumference of the cylinder. Figure 3.11 shows the nodal forces acting on the cylinder, when looking along the axis of the cylinder, where the lengths of the arrows are proportional to the magnitude of the force, and all the forces are acting normal to the surface of the cylinder. Figure 3.12 shows the same results as shown in Figure 3.11, only viewed in three dimensions.

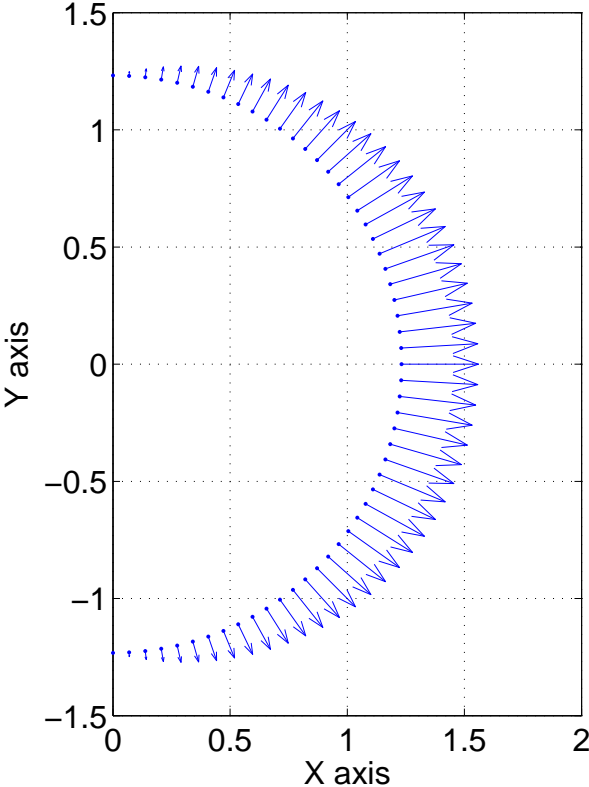


FIG. 3.11: Plot of the nodal loads on the cylinder that accounts for the nodal area and incidence angle. The length of the arrows is proportional to the magnitude of the nodal force.

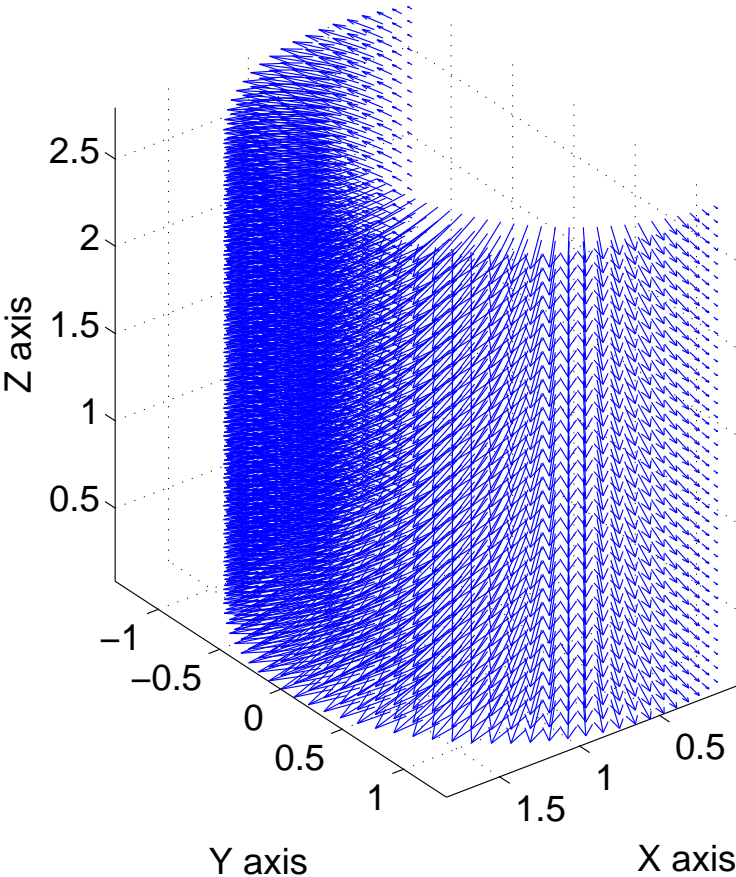


FIG. 3.12: Plot of the load on the cylinder that account for the nodal area and incidence angle.

By using Eq. (3.43), one can plot the real and imaginary parts of the nodal forces. As an example, Figure 3.13 shows the real and imaginary part of a nodal force, with one end of the curve corresponding to the force at 50Hz, and the other end of the curve corresponding to the force at 300Hz. The curve has a constant curvature, or radius from the origin, which indicates that the magnitude of the force is constant. Figure 3.14 shows

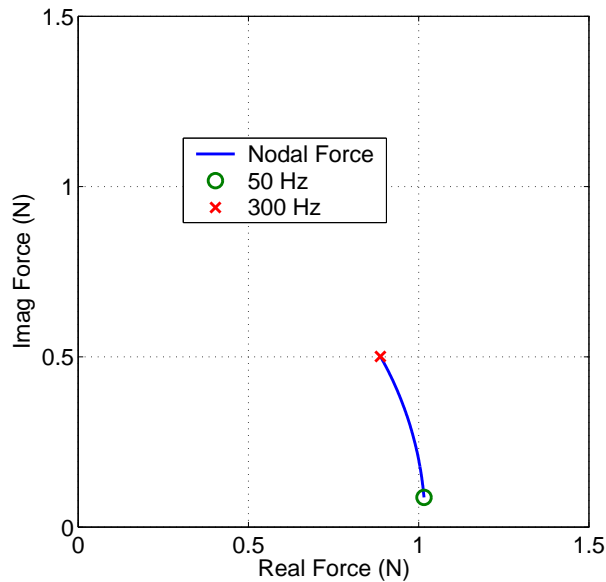


FIG. 3.13: Plot of the real and imaginary parts of the force.

a similar plot as Figure 3.13, only all the nodal forces are plotted. The results show that all the curves have constant curvature, indicating that for each node, the magnitude of the force is constant over the frequency range.

Figure 3.15 shows the acoustic potential energy inside the cylinder without PVADs, for the case where the nodes on the circumference of the cylinder have 1N radial load, and when the wall of speakers is on one side to model the acoustic loading caused by an exhaust plume on one side only.

The first peak in the spectra occurs at about 62Hz, which coincides with the first acoustic mode (after the bulk acoustic mode). The first structural resonance occurs at 39Hz, which is below the frequency range of interest. The results show that the APE within the cylinder for the case where there is an asymmetric load is much greater than when there is a axi-symmetric load. The asymmetric load is able to excite more structural and acoustic modes than the axi-symmetric load, which only effectively drives the bulk breathing mode and has acoustic cancellation effects occurring within the cavity.

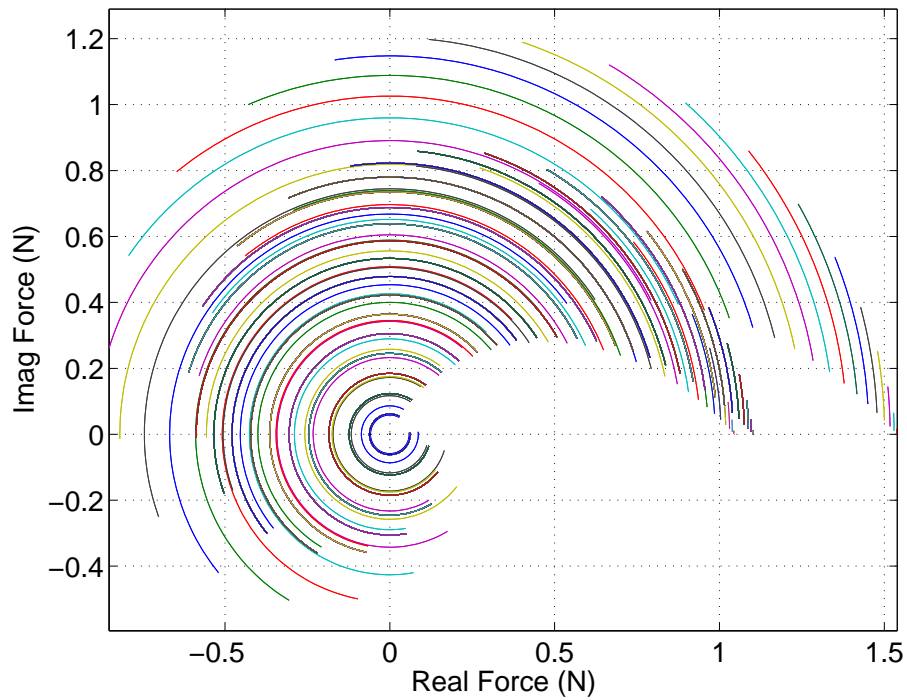


FIG. 3.14: Plot of the real and imaginary parts of the force.

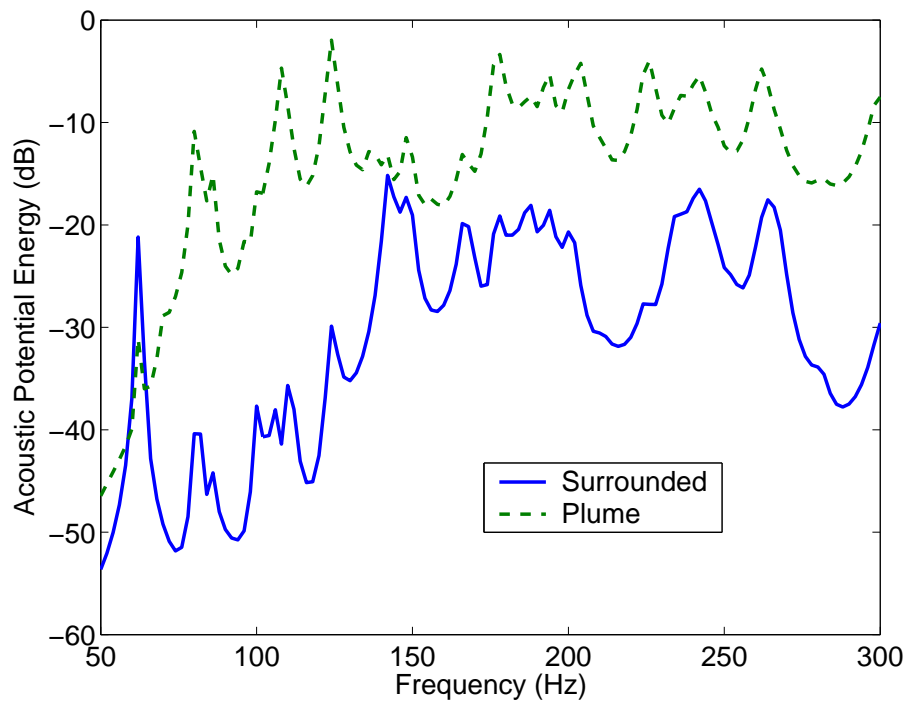


FIG. 3.15: Comparison of the acoustic potential energy inside the cylinder without PVADs, for the case where the nodes on the circumference of the cylinder have 1N load, and when the wall of speakers is on one side (plume).

Chapter 4

Genetic Algorithms

4.1 Introduction

A Genetic Algorithm (GA) was developed and used in the previous stage of work [5] to find locations and parameters for the vibro-acoustic devices that would minimise the acoustic potential energy within the cavity. Some of the conclusions from the work were:

- whilst in principle the optimisation routine is well suited to the problem, the evaluation of the cost function took considerable time and needed improvement,
- the Genetic Algorithm that was developed also needs improvement, and
- one should consider the use of distributed computing.

The GA can be easily adapted for use in a distributed computing environment, where a *master* processor distributes jobs to *slave* processors, as shown in Figure 4.1. The

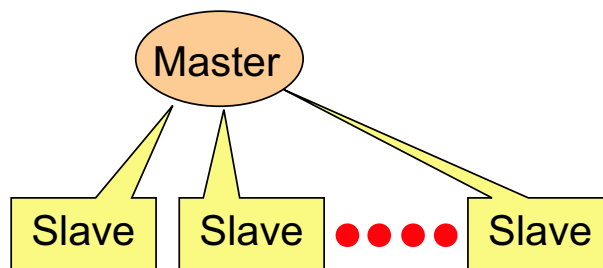


FIG. 4.1: Diagram of showing a master processor distributing tasks to a variable number of slave processors.

master processor takes care of managing the population and the synchronisation of the slave processors. The master processor handles the selection and mating. The slave processors calculate the cost function and return the results. In the simplest form, all the cost functions are evaluated at the same time, and the master processor waits until all the results are returned from the slave processors. This scheme is called a *synchronous master-slave* GA, which is relatively easy to implement but suffers from the drawback that it requires all the slave processors to complete their tasks before the master processor can update the population. If one of the slave processors fails, then the population cannot be updated. In addition the GA can only update at the speed of the slowest slave processor.

A variation of this scheme is the *semi-synchronous master-slave* [10, p208], where the master process does not depend on the completion of all the slave processors, and instead selects members ‘on the fly’.

The GA software that was developed in Stage 2 was not used as a starting point for developing a parallel GA. There is a freely available parallel genetic algorithm library available in ANSI C and Fortran [11]. However this software also requires an implementation of the Message Passing Interface (MPI), and requires that the machine is dedicated to the distributed network. The large pool of computers available at the University of Adelaide are accessed by students and are not dedicated to a distributed computing environment. Hence this software is not suitable for the task.

Instead, a software package called Genetic Algorithm Optimisation Toolbox (GAOT) [12] was used as a starting point, and was modified by the authors to make it suitable for a distributed computing environment. The algorithm determines several chromosomes that require cost function evaluations, and then sends the jobs to the master processor which handles the distribution of the tasks to the slave computers. A software package called Condor was used as the framework for the distributed computing environment and is discussed in the next section.

The previous work in Stage 2 involved the use of integer representation of the chromosomes, however the authors of that report felt that it would be better to implement a binary representation, which was done in this stage of the work.

4.2 Condor Software

The Condor software package is freely available and can be used for distributed computing [13]. It is best suited to ‘embarrassingly parallel’ problems, where there is no inter-processor communication. This type of framework is suitable for parallel GAs where a master processor is responsible for ‘managing’ the population, conducting the breeding and mutation and distributing the cost function evaluations to ‘slave’ processors. The slave processors receive the jobs from the master processor, and evaluate the cost function, and return the value of the cost function, in this case the acoustic potential energy within the cavity.

The Condor system was installed on the faculty’s 120 Pentium computers and one computer was assigned as the master processor and distributed the jobs to the slave computers.

An attractive feature of the Condor system is that the master processor responsible for the distribution of tasks can look at the usage of the computer and tell if someone is using the machine. If the machine is being used by a student, then that computer is marked as unavailable. The system was set up so that computers that have been left idle for 15 minutes are marked as available to the Condor pool. One limitation of the present system, for computers running Microsoft Windows XP, is that if the computer is used by a student whilst it is processing a job, the computer will halt the task and find another computer to run the task, but it will re-start the job from the beginning instead of continuing from where the interruption occurred. This is not a significant problem because the students do not use the computers overnight, when they are used for the GA calculation.

The Matlab compiler [14] was used to create a binary executable file for the cost function evaluation. The executable file reads in Matlab .mat files and extracts the

parameters for the PVADs and then uses those parameters to calculate the acoustic potential energy, which is then written to an output Matlab .mat file. The genetic algorithm reads the results from the cost function evaluation and determines if there was any improvement in the results.

4.3 Synchronous Genetic Algorithm

The initial development of the GA code was with the Genetic Algorithm Optimisation Toolbox (GAOT) [12] for Matlab. The Matlab code was modified so that it would work with the Condor system in a synchronous manner - the GA sends a number of jobs to the Condor pool, and the GA waits until it has received all the answers from the submission. There are several problem with this system:

- All the jobs must complete successfully before the next set of chromosomes can be calculated. Some processors can take longer than others, because the slave computers do not have the same configuration, and hence the synchronous method is dependent on the slowest processor.
- If one of the jobs fails, then the whole optimisation process will cease.

Hence these limitations were the impetus for developing an asynchronous parallel Genetic Algorithm.

4.4 Asynchronous Genetic Algorithm

Another software package called the Genetic Algorithm Toolbox [15] was used as a basis for developing an asynchronous parallel GA. As a starting point, the Genetic Algorithm Toolbox was used in the intended manner, where the cost functions were evaluated on the local machine, then the asynchronous parallel GA code was developed, where the cost function evaluations were submitted to remote machines through the Condor system. The results from both optimisations were compared to ensure that they obtained the same results.

Five parameters were chosen to be optimised for each PVAD:

1. the location of the PVAD,
2. the stiffness of the Helmholtz resonator,
3. the damping of the Helmholtz resonator,
4. the stiffness of the TMD, and
5. the damping of the TMD.

Each of these parameters was assigned a finite number of choices, each corresponding to a physical value. For example, say that we permit 11 possibilities for damping in the linear range from 5% to 25%. If the GA selects a value of 4, then the damping value is converted to 11%.

The results from the Stage 2 report showed that the best results occur when the mass of the TMD is maximised, so as to maximise absorption, and when the mass of the HR is

minimised, to get the best coupling between the HR and the cavity. Note that the mass of the HR is the effective mass of the air in the neck. For the optimisation of the large box, it was assumed that the mass of the TMD was 0.45kg and the mass of the HR was 0.01kg. By fixing the mass, and allowing the resonance frequency of the device to vary within a range, one can calculate the equivalent stiffness.

The operation of the asynchronous GA was developed with guidance from Ref [16], as follows:

1. The GA generates a random initial population
2. The cost functions are evaluated for the initial population either on the local machine, if the problem is small, or using the Condor pool if the problem is large, and the results are saved, in case the optimisation needs to be re-started.
3. The GA checks how many jobs are already being calculated by the slave processes and if it has not exceeded a chosen value (it is possible to have more jobs in the Condor queue than the number of computers in the pool), then
 - (a) The results from the cost function evaluations are sorted in rank order based on their fitness (in this case Acoustic Potential Energy).
 - (b) A new set of individuals is created by performing the selection, mutation and recombination operations. If the new set of individuals has been previously calculated, the process is repeated. Note this is only possible when the size of the chromosomes is small, otherwise the matrix of previously calculated chromosomes becomes excessively large and causes an overflow in the computer's memory.
 - (c) A file is generated for submission to the Condor pool. The file contains the parameters for the PVADs (chromosomes). The files are placed in a unique directory, where all the files relevant to that particular cost function evaluation reside. The job is submitted to the Condor pool.
4. The directory structure is checked for the existence of a file called success.sub, which indicates that the cost function evaluation completed successfully. The jobs that are ready to have their results read back into the GA are formed into a queue, with the oldest jobs at the front of the queue.
5. The results from the cost function evaluation from the oldest job in the queue are retrieved.
6. The new population is inserted into the old population by replacing the chromosomes in the old population that had the worst fitness, in this case the highest acoustic potential energy.
7. The process repeats from step 3.

The selection method used is stochastic universal sampling [17]. Stochastic Universal Sampling (SUS) is a single-phase sampling algorithm with minimum spread and zero bias. Spread is the range in the possible number of trials that an individual may achieve. If

$f(i)$ is the actual number of trials that individual i receives, then the ‘minimum spread’ is the smallest spread that theoretically permits zero bias, i.e.

$$f(i) \in \{\lfloor et(i) \rfloor, \lceil et(i) \rceil\} \quad (4.1)$$

where $et(i)$ is the expected number of trials of individual i , $\lfloor et(i) \rfloor$ is the floor of $et(i)$ and $\lceil et(i) \rceil$ is the ceil. Thus, while bias is an indication of accuracy, the spread of a selection method measures its consistency. Instead of the single selection pointer employed in roulette wheel methods, SUS uses N equally spaced pointers, where N is the number of selections required. The population is shuffled randomly and a single random number in the range $[0, \text{Sum}/N]$ is generated, ptr . The N individuals are then chosen by generating the N pointers spaced by 1, $[ptr, ptr + 1, \dots, ptr + N - 1]$, and selecting the individuals whose fitnesses span the positions of the pointers. An individual is thus guaranteed to be selected a minimum of $\lfloor et(i) \rfloor$ times and no more than $\lceil et(i) \rceil$, thus achieving minimum spread. In addition, as individuals are selected entirely on their position in the population, SUS has zero bias.

A single-point crossover function is used in the GA [17] that performs the following function:

“Consider the two parent binary strings:

$$P1 = [1 \ 0 \ 0 \ 1 \ 0 \ 1 \ 1 \ 0]$$

$$P2 = [1 \ 0 \ 1 \ 1 \ 1 \ 0 \ 0 \ 0]$$

If an integer position, i , is selected uniformly at random between 1 and the string length, L , minus one $[1, L - 1]$, and the genetic information exchanged between the individuals about this point, then two new offspring strings are produced. The two offspring below are produced when the crossover point $i = 5$ is selected,

$$O1 = [1 \ 0 \ 0 \ 1 \ 0 \ 0 \ 0 \ 0]$$

$$O2 = [1 \ 0 \ 1 \ 1 \ 1 \ 1 \ 1 \ 0]$$

This crossover operation is not necessarily performed on all strings in the population. Instead, it is applied with a probability Px when the pairs are chosen for breeding.”

The reinsertion of the chromosomes into the population is done using an ‘elitist’ strategy, where the least fit chromosomes are replaced by the most recently evaluated chromosomes.

Chapter 5

Results

5.1 Testing of the GA Optimisation

After the development of the GAs that calculated the cost function locally, and using the asynchronous parallel GAs, several test cases were evaluated to test that the algorithms were able to select parameters that would minimise the APE within a cavity. The first optimisation was conducted using a rectangular box, and the second case was with 5 PVADs attached to the Boeing cylinder.

5.1.1 Two PVADs Attached to a Large Box

A picture of a model of a large box with 5 rigid walls and one flexible wall is shown in Figure 5.1. The details of the model are described in Appendix D.4. This model was

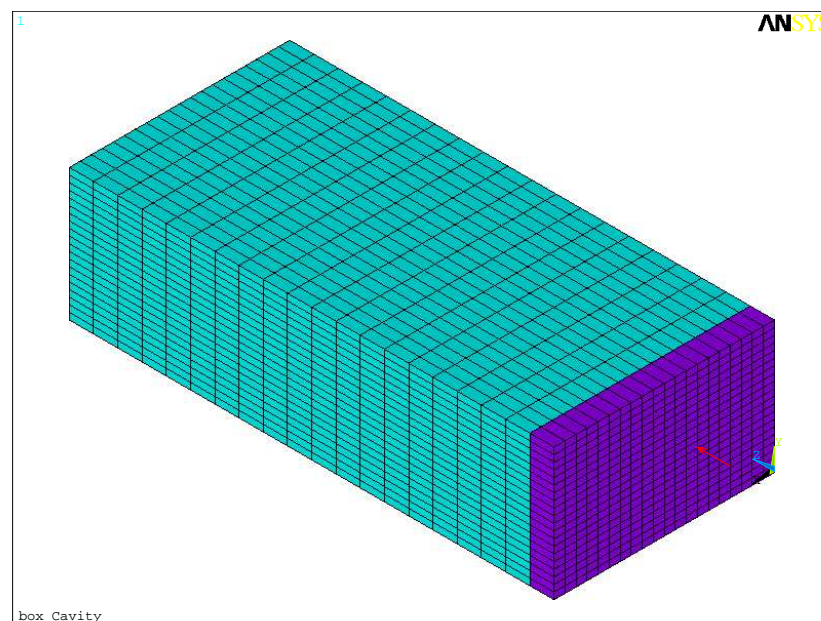


FIG. 5.1: Picture of the large box ANSYS model used for the comparison of the finite element and the Matlab modal coupling software.

used to test that the GA software was capable of finding configurations for 2 PVADs that would minimise the APE within the cavity. The parameters that were varied are listed in Table 5.1. The mass of the TMDs were 0.45kg and the mass of the HRs were 0.01kg.

PVAD parameter	Min	Max	No Values	Comment
PVAD position	1	273	273	All structural elements
Mass-spring frequency	20	400	500	[Hz]
Mass-spring damping (η)	0.01	0.25	10	
Acoustic resonator frequency	20	400	500	[Hz]
Acoustic resonator damping (η)	0.01	0.25	10	

Table 5.1: PVAD parameter range for the optimisation of the large box.

Figure 5.2 shows the reduction in the cost function with the evolution of the GA. The asynchronous GA code submits two cost function evaluations to the Condor pool at a time, hence the number of cost functions evaluated is twice the generation value shown in Figure 5.2. Hence, there were 600 cost function evaluated using the asynchronous parallel GA.

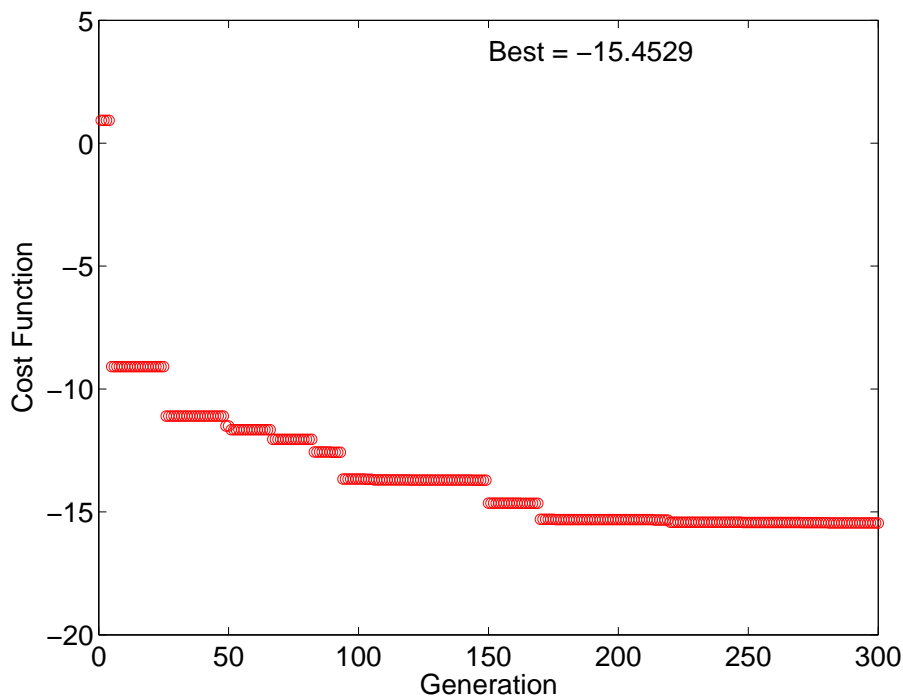


FIG. 5.2: Plot of the reduction in the cost function versus the generation. This result is for the optimisation using the Condor system.

The problem was also solved for 700 cost functions evaluated on a local machine, without sending them to the Condor pool. Table 5.2 lists the reduction in the APE for the methods used. Figure 5.3 shows the APE within the cavity for the baseline case without PVADs, optimisation using the GA when the cost function evaluation was conducted locally, and when the asynchronous parallel GA was used. The results shows that the same attenuation is obtained when the GA calculates the cost function locally, and when the cost functions were evaluated remotely using the asynchronous parallel GA.

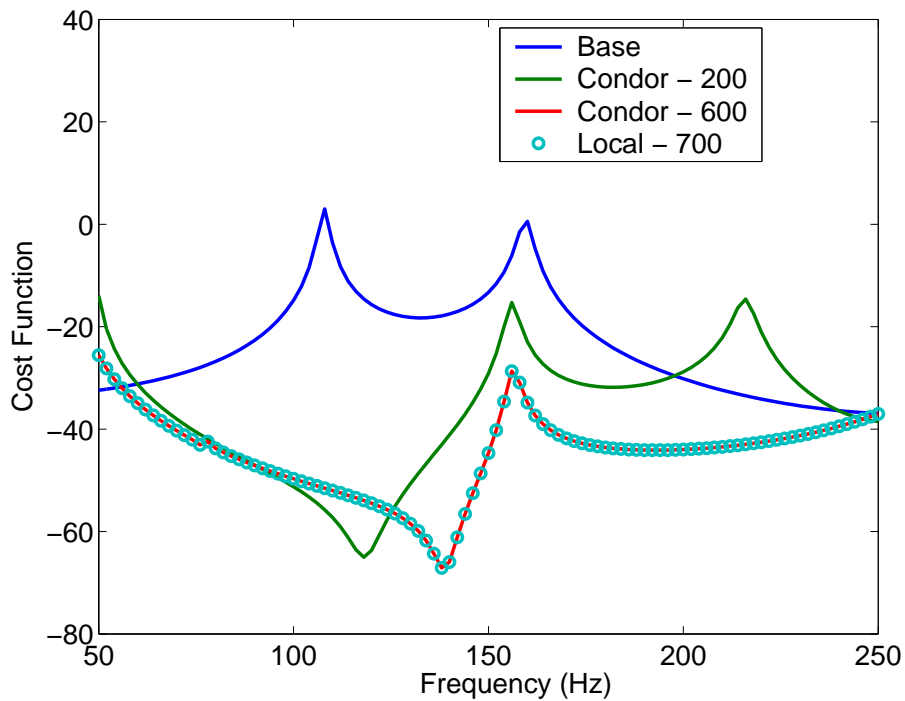


FIG. 5.3: The acoustic potential energy within the box for the baseline and the best result from the Condor GA optimisation, and the GA local optimisation. The number of actual cost function evaluations is shown in the legend.

No. Cost Function Evaluations	Local or Condor	Attenuation (dB)
200	Condor	14
600	Condor	25
700	Local	25

Table 5.2: Reduction in the APE for the optimisation of PVADs attached to the large box.

The values of the parameters that were found for the optimisation after 600 cost function evaluations using the Condor system are listed in Table 5.3.

PVAD No.	Node	TMD		HR	
		Stiffness ($\times 10^6$ N/m)	Damping (%)	Stiffness ($\times 10^4$ N/m)	Damping (%)
1	442	8.87	10.6	8.91	22.6
2	521	1.73	22.6	8.63	17.8

Table 5.3: Value of parameters for the PVADs applied to the large box model, after 600 cost function evaluations

5.1.2 Five PVADs Attached to the Boeing Cylinder

An optimisation was conducted to find the location and parameters of 5 PVADs that would minimise the acoustic potential energy within the entire cavity over the frequency range 50-300Hz, in frequency increments of 2Hz. The loading condition on the model of the Boeing cylinder was a 1N force applied to all the nodes on the circumference of the cylinder. The range of parameters for each PVAD is described in Table 5.4. The location of the PVADs was limited to any node on the circumference of the cylinder. The mass of the TMDs was 1.0kg and the mass of the HRs was 0.01kg.

The optimisation was conducted using the Genetic Algorithm toolbox [15] where the cost function evaluations were conducted locally on the host machine (a 3.0 GHz Intel Pentium 4, Hyperthreading, 800 MHz FSB, 1Gb RAM PC3200), and also using the asynchronous parallel GA and the Condor pool (the computers were mostly 2.4GHz Pentium 4, 512MB RAM).

As described previously, there is a significant length of time between the submission of the job and when the job starts to run on the slave computer, which can be on the order of a minute. One has to determine if the use of Condor system will be more time effective than if the cost functions are evaluated on the local host machine.

It was found for the optimisation described in this section, it took 6 minutes to calculate one cost function when evaluated on the 3.0GHz PC. The time taken for the same job submitted to the Condor pool took about 8 mins to evaluate. However, because the Condor jobs can be submitted in parallel, the result of the cost function evaluations return substantially quicker. It was found that the results from 10 jobs, or 20 cost function evaluations, took 4 min 30 seconds, when 80 PCs were used. Hence on average, a cost function evaluation completes every 13.5 seconds, which means the GA can update the population every 13.5 seconds. The time could be further reduced by using more PC's. During this optimisation, about 50 PCs in the Condor pool were unused, which could have increased the performance had they been used.

On average, there is about a 25 times speed increase using 100 computers, compared to evaluating the cost function on a local machine with a 3.0GHz processor.

The asynchronous GA was used to optimise the parameters of 5 PVADs, when the loading condition was a 1N force on all the circumference nodes on the structure. This simulates a plane wave hitting the cylinder from all directions. After 12000 cost function evaluations the PVADs were able to reduce the APE within the cylinder by 2.1dB overall in the frequency range 50-300Hz. The APE is shown in Figure 5.4.

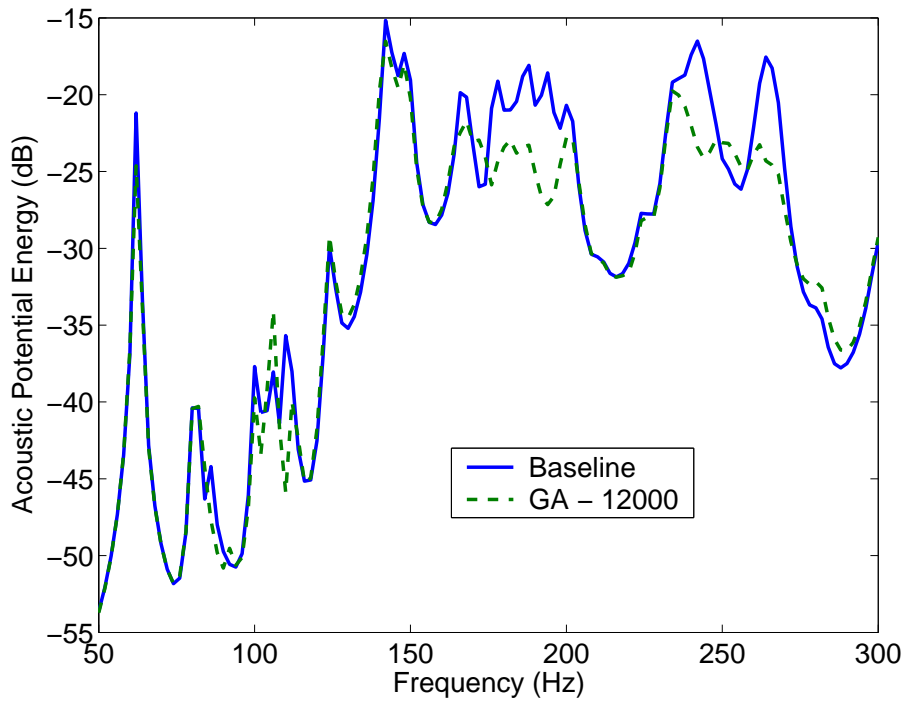


FIG. 5.4: Acoustic potential energy within the cavity after using the GA for 12000 cost function evaluations.

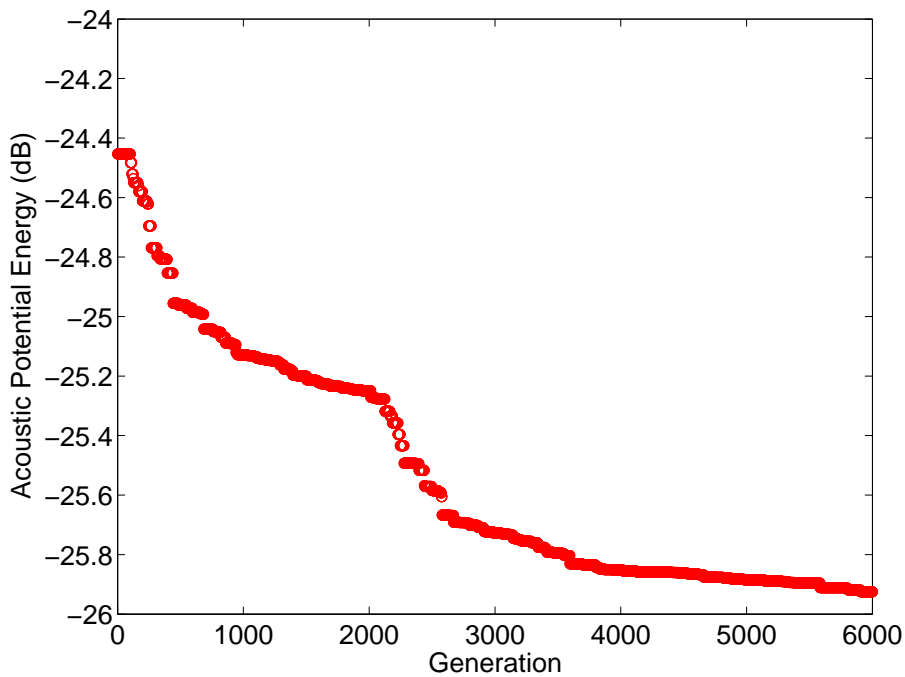


FIG. 5.5: Acoustic potential energy within the cavity after using the GA for 12000 cost function evaluations.

5.2 Performance vs Number of PVADs

Several optimisations were conducted to determine the variation of the acoustic potential energy within the cavity when varying the number of PVADs. Optimisations were conducted over 18,000 cost function evaluations, using 10, 20 and 30 PVADs, where they could be located anywhere on the circumference of the cylinder, and the parameters were allowed to vary as listed in Table 5.4.

PVAD parameter	Min	Max	No. Values	Comment
PVAD position	1	4032	4032	Circumferential nodes
Mass-spring frequency	11	510	500	[Hz]
Mass-spring damping (η)	0.01	0.25	10	
Acoustic resonator frequency	11	510	500	[Hz]
Acoustic resonator damping (η)	0.01	0.25	10	

Table 5.4: PVAD parameter range for the optimisation of the Boeing cylinder.

Table 5.5 lists the population size for each of the optimisations.

No. PVADs	Population Size
5	20
10	20
20	60
30	60

Table 5.5: The population size for each of the optimisations

Figure 5.6 shows the variation in acoustic potential energy versus frequency for 10, 20 and 30 PVADs. Figure 5.7 shows the average acoustic potential energy within the cavity, over 50 - 300Hz.

Figure 5.8 shows the location of 10 PVADs after 18,000 cost function evaluations (two cost function evaluations per generation) plotted in three dimensions, and Figure 5.9 shows the locations of the PVADs on an angular plot, where the 0° is along the X -axis, pointing towards the sound source.

Table 5.7 lists the approximate resonance frequencies of the 10 PVADs, based on the stiffness values in Table 5.6, and that the mass of the TMD and HR are 0.45kg and 0.01kg, respectively.

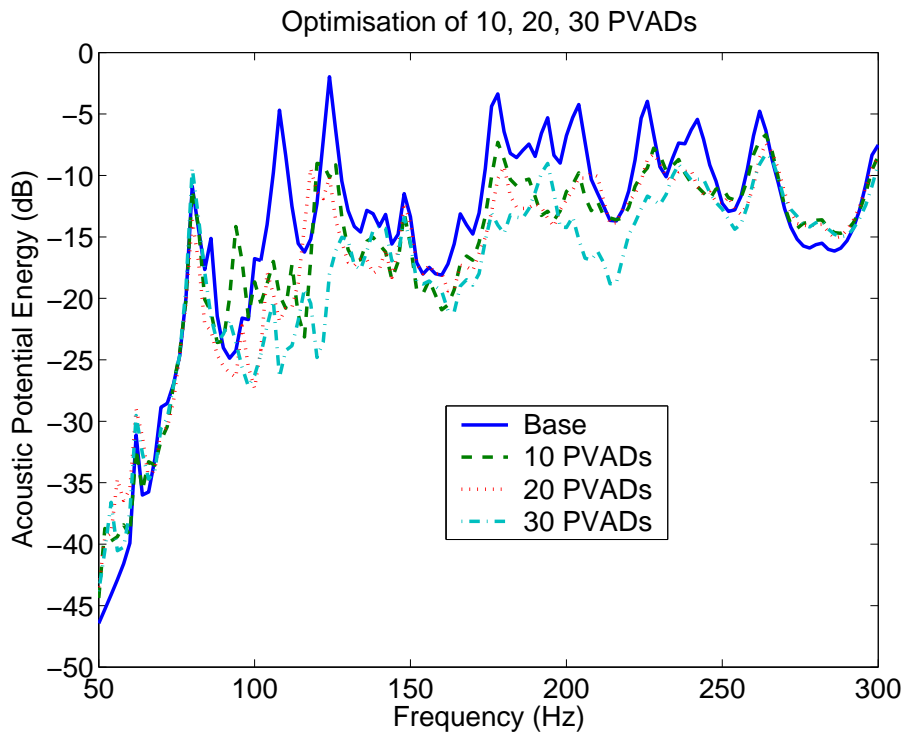


FIG. 5.6: Variation in acoustic potential energy for no PVADs (Base), 10, 20 and 30 PVADs.

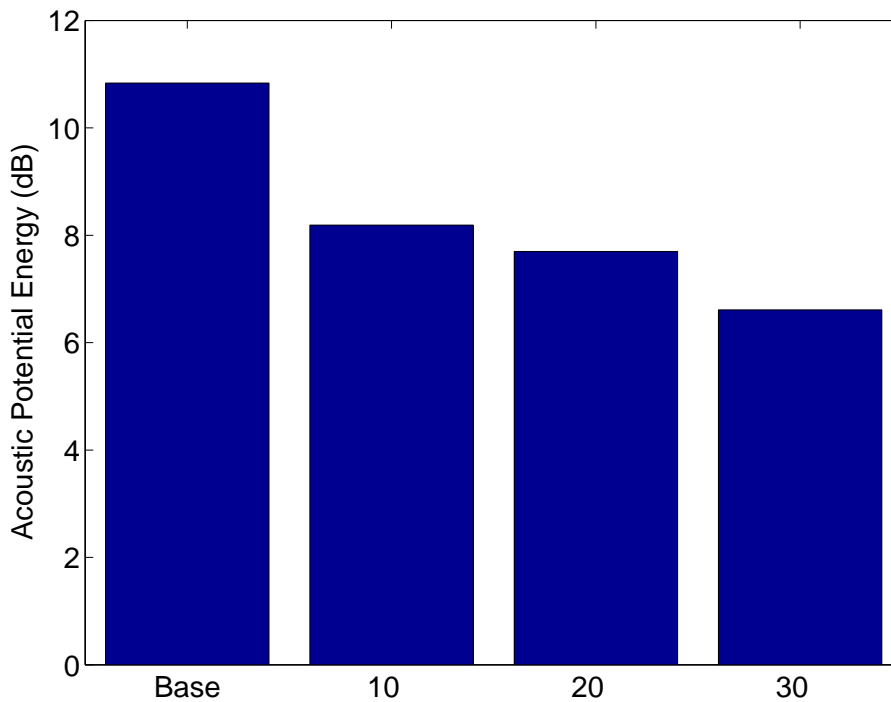


FIG. 5.7: Average acoustic potential energy for no PVADs (Base), 10, 20 and 30 PVADs.

PVAD No.	Location			TMD		HR	
	Node	θ (degrees)	Z (m)	Stiffness ($\times 10^6$ N/m)	Damping (%)	Stiffness ($\times 10^4$ N/m)	Damping (%)
1	27227	-70.7	0.56	1.91	25	3.43	3
2	9916	73.9	1.76	1.08	25	3.45	3
3	25204	-61.1	1.44	1.42	23	2.26	11
4	27169	-90.0	1.36	1.32	23	2.73	3
5	29414	-176.8	1.92	4.59	13	3.08	6
6	20866	-16.1	1.60	2.25	13	2.02	3
7	25126	-54.6	0.64	2.82	18	2.32	6
8	7634	67.5	0.96	3.46	20	0.27	3
9	12502	180.0	1.12	0.30	25	3.27	11
10	27239	-70.7	1.52	4.47	20	3.21	20

Table 5.6: Value of parameters for the 10 PVADs after 18,000 cost function evaluations

PVAD No.	TMD Freq (Hz)	HR Freq (Hz)
1	220	295
2	166	296
3	190	239
4	183	263
5	341	279
6	239	226
7	267	243
8	296	83
9	87	288
10	337	285

Table 5.7: Approximate resonance frequencies of the 10 PVADs after 18,000 cost function evaluations

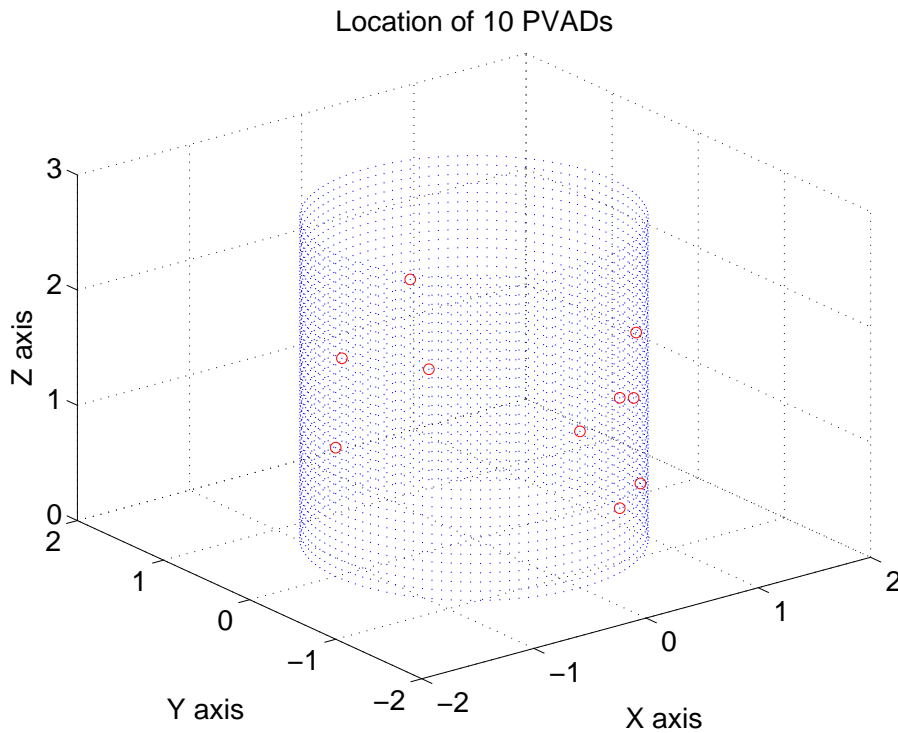


FIG. 5.8: Location of the 10 PVADs after optimisation for 18,000 cost function evaluations, viewed in three dimensions.

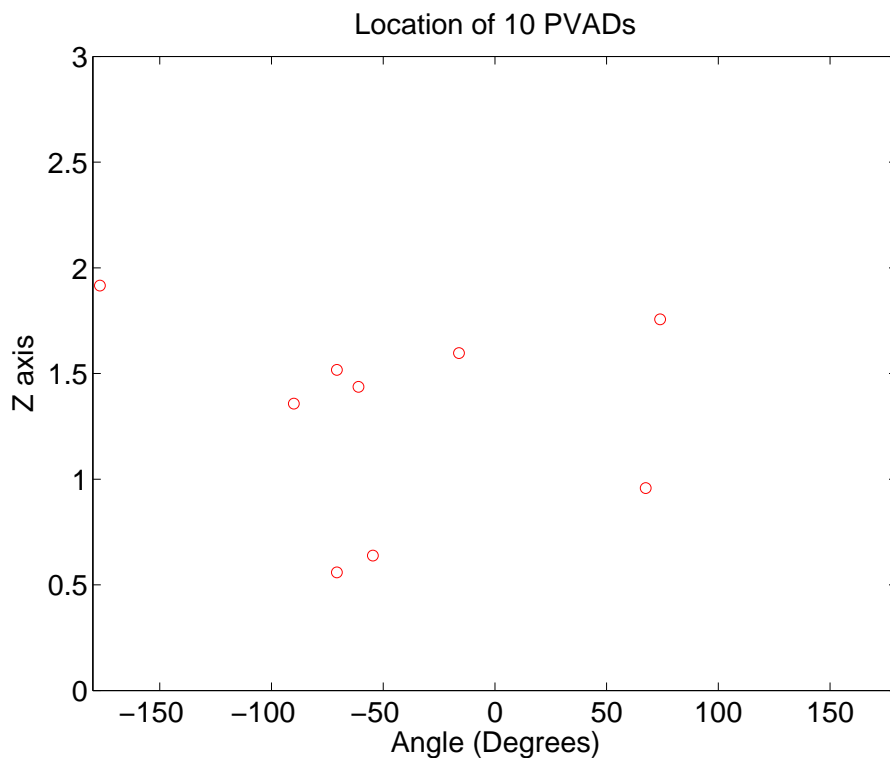


FIG. 5.9: Location of the 10 PVADs after optimisation for 18,000 cost function evaluations, as if the surface of the cylinder had been unwrapped.

Figure 5.10 shows the location of 20 PVADs after 18,000 cost function evaluations plotted in three dimensions, and Figure 5.11 shows the locations of the PVADs on an angular plot, where the 0° is along the X -axis, pointing towards the sound source.

Table 5.9 lists the approximate resonance frequencies of the 20 PVADs, based on the stiffness values in Table 5.8, and that the mass of the TMD and HR are 0.45kg and 0.01kg, respectively.

PVAD No.	Location			TMD		HR	
	Node	θ (degrees)	Z (m)	Stiffness ($\times 10^6$ N/m)	Damping (%)	Stiffness ($\times 10^4$ N/m)	Damping (%)
1	33741	-131.8	0.88	1.06	15	1.02	20
2	27242	-70.7	1.76	2.59	25	0.57	18
3	25105	-51.4	1.68	3.35	25	0.61	23
4	27273	-73.9	1.52	2.05	20	0.37	8
5	29472	-170.4	1.12	1.70	13	0.42	13
6	22925	-28.9	0.88	0.62	25	0.13	23
7	18600	106.1	2.08	1.35	20	0.60	20
8	7776	54.6	1.44	4.33	11	1.01	3
9	14925	141.4	2.32	0.76	13	0.39	13
10	27170	-90.0	1.44	2.47	13	0.52	11
11	7646	67.5	1.92	1.95	20	0.11	25
12	5584	28.9	2.39	1.16	23	0.82	6
13	31758	-138.2	2.24	4.27	23	0.19	6
14	20755	-6.4	0.88	1.75	25	0.51	8
15	20731	-3.2	1.68	3.55	13	0.20	25
16	7636	67.5	1.12	2.61	20	0.16	18
17	12691	167.1	2.63	4.09	18	0.34	13
18	35485	-96.4	0.72	2.36	15	0.06	3
19	27167	-90.0	1.20	0.65	11	0.07	15
20	12713	163.9	1.68	2.39	20	0.07	11

Table 5.8: Value of parameters for the 20 PVADs after 18,000 cost function evaluations

PVAD No.	TMD Freq (Hz)	HR Freq (Hz)
1	164	161
2	256	120
3	291	125
4	228	96
5	208	103
6	125	56
7	185	124
8	331	160
9	139	100
10	250	115
11	222	52
12	171	144
13	329	69
14	210	114
15	300	71
16	257	64
17	322	93
18	244	40
19	128	43
20	246	41

Table 5.9: Approximate resonance frequencies of the 20 PVADs after 18,000 cost function evaluations

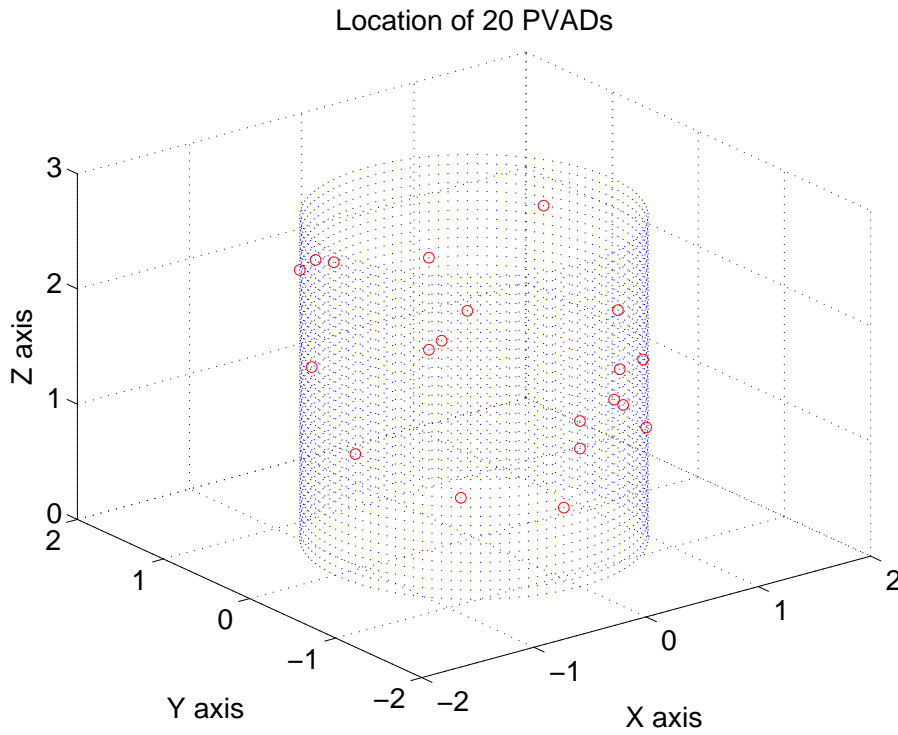


FIG. 5.10: Location of the 20 PVADs after optimisation for 18,000 cost function evaluations, viewed in three dimensions.

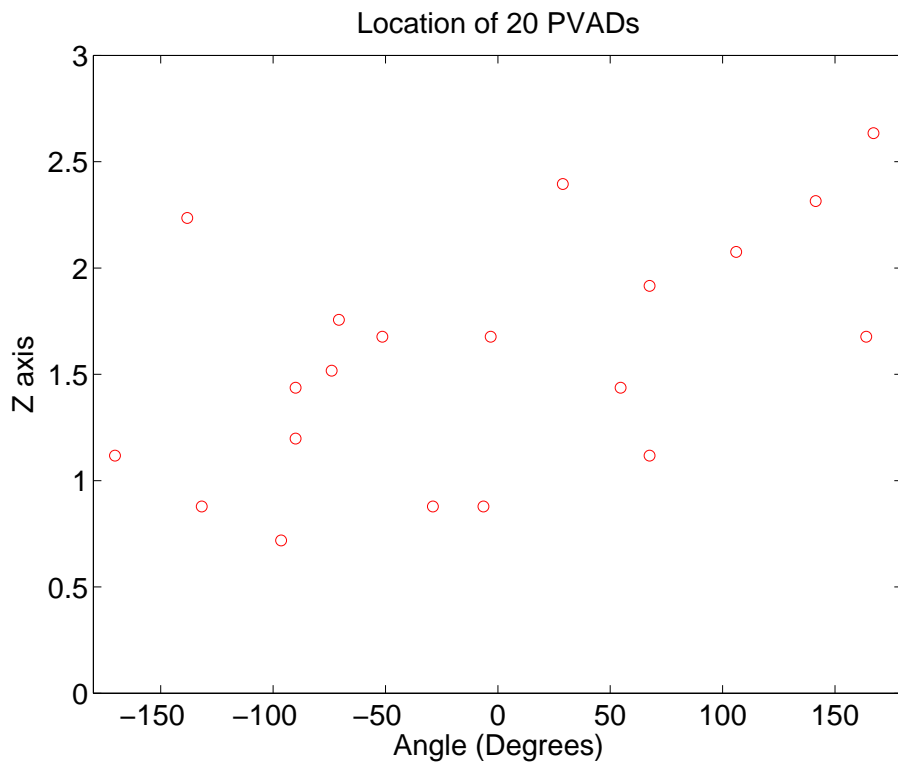


FIG. 5.11: Location of the 20 PVADs after optimisation for 18,000 cost function evaluations, as if the surface of the cylinder had been unwrapped.

Figure 5.12 shows the location of 30 PVADs after 18,000 cost function evaluations plotted in three dimensions, and Figure 5.13 shows the locations of the PVADs on an angular plot, where the 0° is along the X -axis, pointing towards the sound source.

Table 5.11 lists the approximate resonance frequencies of the 30 PVADs, based on the stiffness values in Table 5.10, and that the mass of the TMD and HR are 0.45kg and 0.01kg, respectively.

PVAD No.	Location			TMD		HR	
	Node	θ (degrees)	Z (m)	Stiffness ($\times 10^6$ N/m)	Damping (%)	Stiffness ($\times 10^4$ N/m)	Damping (%)
1	33688	-112.5	2.08	3.96	15	6.72	25
2	9984	80.4	1.76	2.22	11	2.18	3
3	10051	86.8	1.68	2.83	13	2.80	3
4	7836	61.1	0.80	3.72	20	5.79	15
5	20743	-3.2	2.63	2.38	25	2.55	6
6	33918	-115.7	1.44	0.43	25	6.29	3
7	7636	67.5	1.12	3.69	13	7.85	15
8	25209	-61.1	1.84	2.29	25	6.10	11
9	3469	12.9	1.36	0.93	13	2.16	20
10	35403	-106.1	2.32	1.71	6	9.94	18
11	25180	-57.9	2.24	3.72	18	3.82	20
12	18625	102.9	1.36	2.70	25	2.78	20
13	31519	-135.0	2.16	3.11	13	0.50	13
14	5601	32.1	1.04	1.49	25	5.38	8
15	22902	-25.7	1.76	4.24	25	0.89	20
16	16881	112.5	1.52	3.10	25	8.95	6
17	16883	112.5	1.68	2.87	20	0.03	13
18	12647	170.4	1.84	1.43	18	1.95	3
19	10003	83.6	0.56	0.31	11	6.06	18
20	14948	138.2	1.44	0.99	18	3.45	8
21	33782	-128.6	1.44	1.27	20	2.88	8
22	7647	67.5	2.00	2.36	25	2.47	20
23	35523	-93.2	1.04	0.47	25	2.76	23
24	27228	-70.7	0.64	2.21	25	2.88	20
25	3218	0.0	0.32	3.67	20	7.46	6
26	12511	180.0	1.84	0.50	25	3.12	6
27	18616	102.9	0.64	2.49	23	0.58	11
28	27273	-73.9	1.52	4.17	18	6.12	18
29	14799	151.1	0.40	3.20	13	1.93	3
30	25008	-67.5	2.08	4.42	25	9.55	3

Table 5.10: Value of parameters for the 30 PVADs after 18,000 cost function evaluations

PVAD No.	TMD Freq (Hz)	HR Freq (Hz)
1	317	412
2	237	235
3	268	266
4	307	383
5	245	254
6	104	399
7	306	446
8	241	393
9	153	234
10	208	502
11	307	311
12	261	265
13	280	112
14	194	369
15	328	150
16	280	476
17	270	25
18	191	223
19	88	392
20	158	296
21	179	270
22	244	250
23	109	264
24	237	270
25	305	435
26	113	281
27	251	121
28	325	394
29	285	221
30	335	492

Table 5.11: Approximate resonance frequencies of the 30 PVADs after 18,000 cost function evaluations

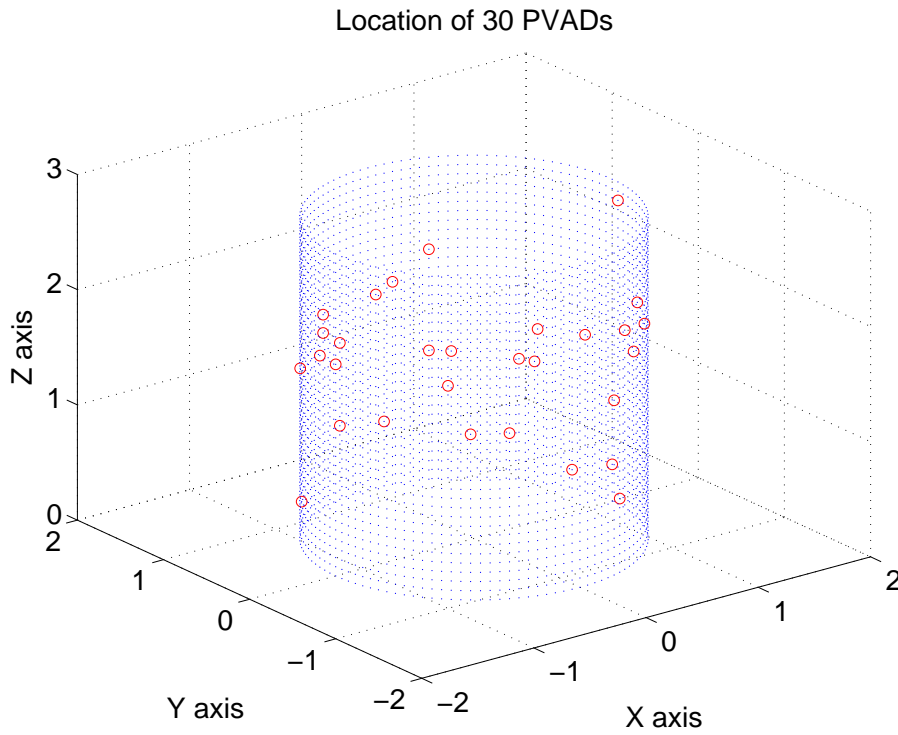


FIG. 5.12: Location of the 30 PVADs after 18,000 cost function evaluations, displayed in three dimensions.

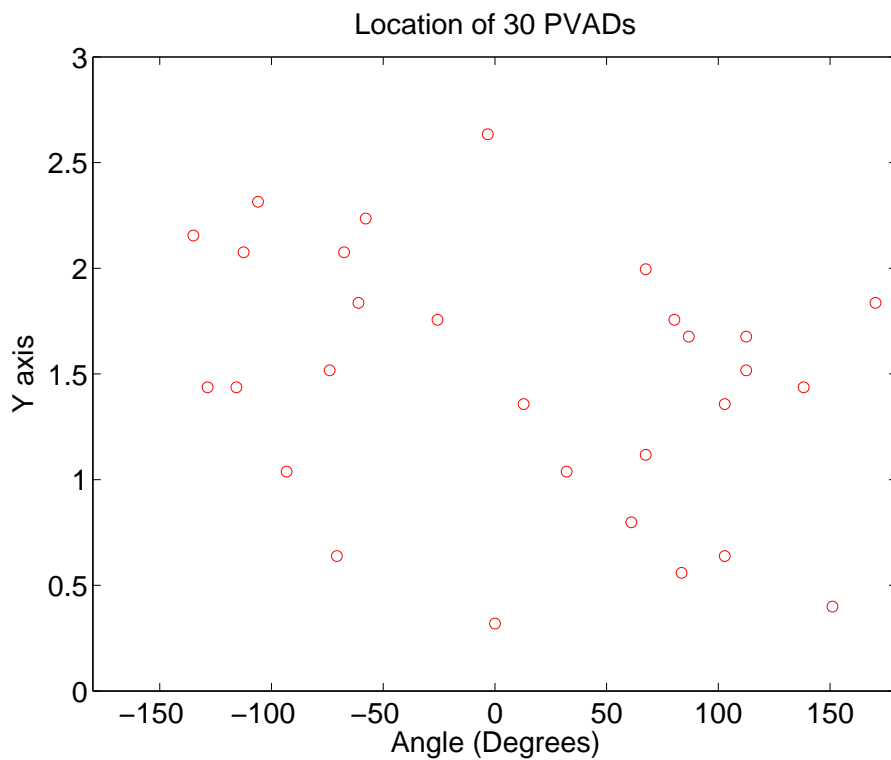


FIG. 5.13: Location of the 30 PVADs after 18,000 cost function evaluations, displayed as if the surface of the cylinder was unwrapped.

The results in Figure 5.7 show that the greatest benefit in the noise reduction was achieved using 30 PVADs, which unfortunately means that the more mass that is added to the structure, the lower the APE. The results in Figure 5.6 show a consistent trend for all three optimisations that the parameters of the PVADs were selected to reduce the noise in the 100-130Hz frequency band.

5.3 Fixed Location and Free Parameters of 20 PVADs

Figure 5.14 shows the location of 20 PVADs arranged into 5 equi-spaced rings along the length of the Boeing cylinder, with 4 PVADs per ring, placed at angles 0° , 90° , 180° , 270° .

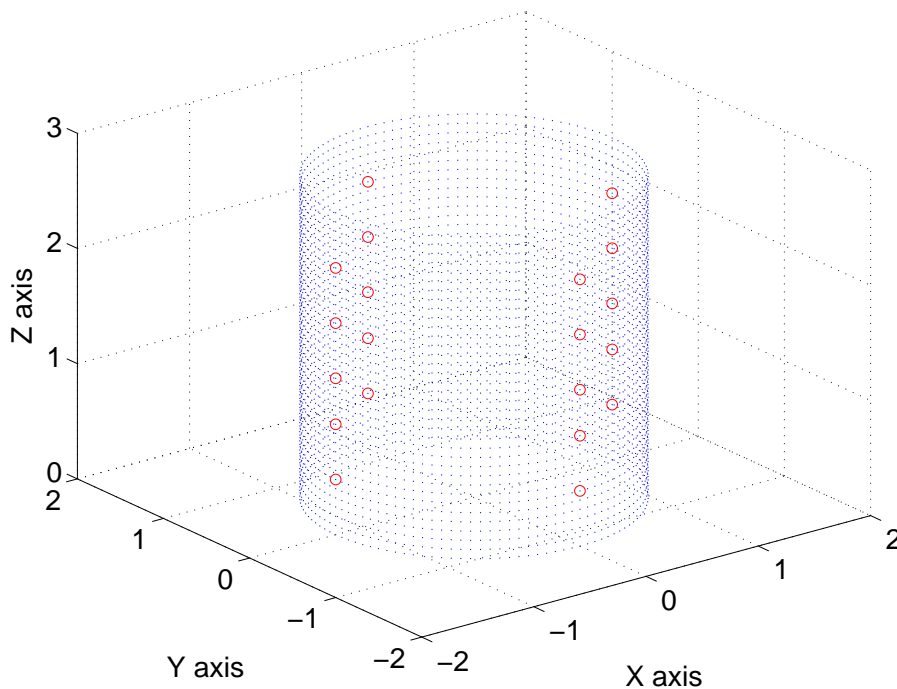


FIG. 5.14: Figure of the circumferential nodes on the Boeing cylinder and the location of the 20 PVADs formed into 5 rings with 4 PVADs on each ring.

Table 5.12 lists the parameters for the 20 PVADs that were arranged into 5 rings of 4 PVADs per ring, after 18,000 cost function evaluations. Table 5.13 lists the approximate resonance frequencies for the PVADs.

Figure 5.15 shows the APE within the cylinder without any PVADs attached to the cylinder (Base) and for 20 PVADs arranged into 5 rings of 4 PVADs per ring (GA). Figure 5.16 shows the reduction in the cost function for each generation.

Figure 5.15 shows that when the 20 PVADs were constrained in location to 5 rings with 4 PVADs per ring, less noise reduction was obtained than when the location and the parameters of the 20 PVADs were allowed to vary, as shown in Figure 5.6.

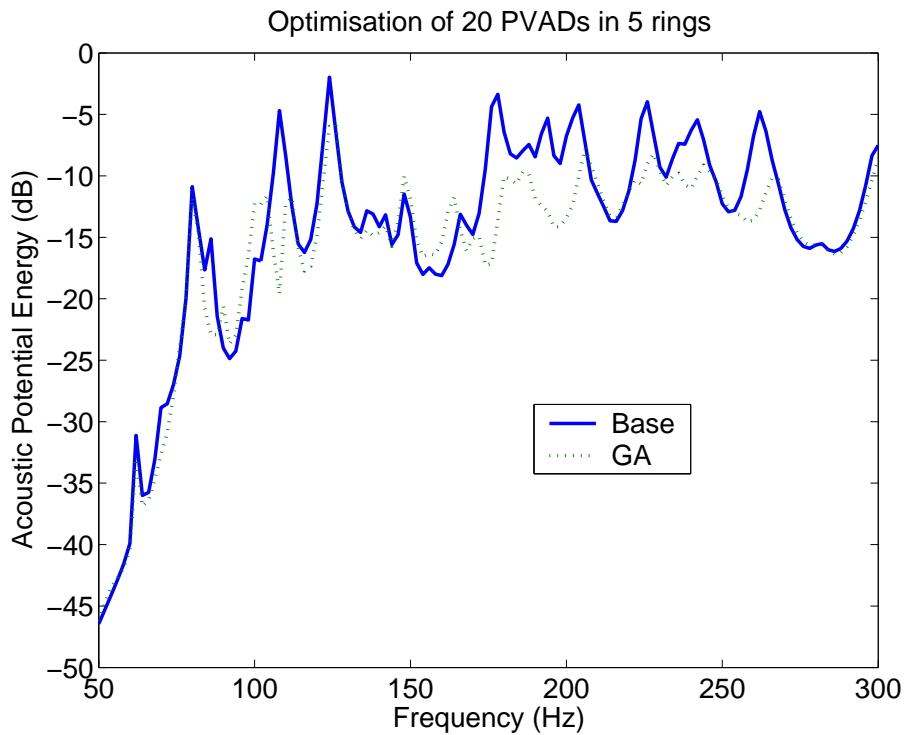


FIG. 5.15: APE within the cylinder without PVADs (Base) and for 20 PVADs arranged into 5 rings of 4 PVADs per ring (GA).

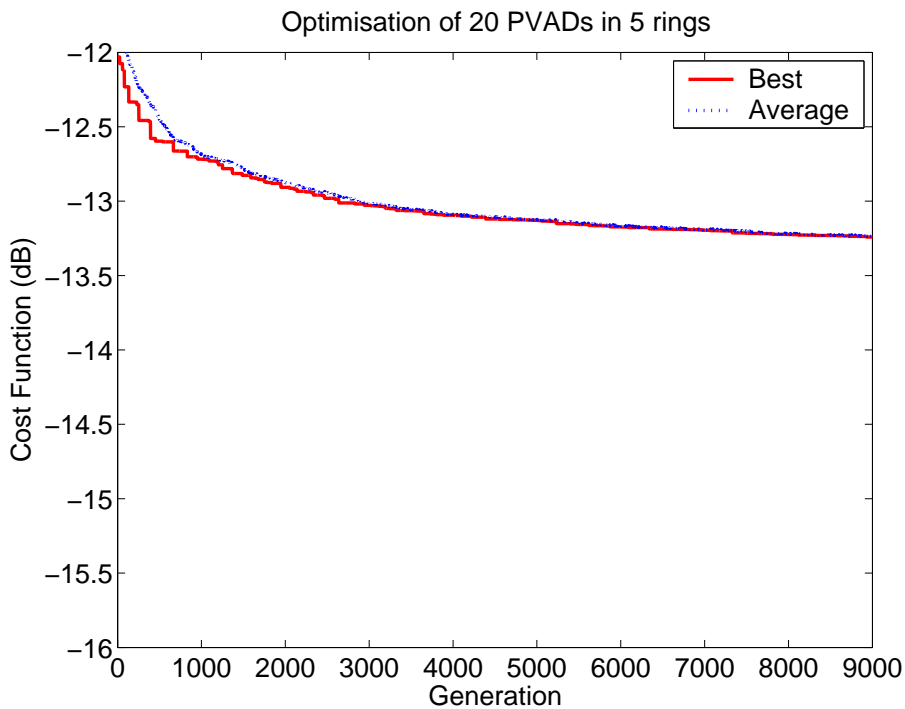


FIG. 5.16: Cost function for each generation within the cylinder for 20 PVADs arranged into 5 rings of 4 PVADs per ring.

PVAD No.	Location			TMD		HR	
	Node	θ (degrees)	Z (m)	Stiffness ($\times 10^6$ N/m)	Damping (%)	Stiffness ($\times 10^4$ N/m)	Damping (%)
1	9798	90.0	0.48	0.29	25	7.70	13
2	9804	90.0	0.96	2.95	20	0.83	13
3	9809	90.0	1.36	0.19	11	1.11	15
4	9815	90.0	1.84	0.11	3	2.28	3
5	9821	90.0	2.32	0.70	6	0.83	3
6	27158	-90.0	0.48	0.20	23	7.23	15
7	27164	-90.0	0.96	0.58	23	3.72	23
8	27169	-90.0	1.36	0.43	15	2.18	8
9	27175	-90.0	1.84	0.24	6	2.45	6
10	27181	-90.0	2.32	0.16	13	1.17	3
11	3220	0.0	0.48	0.45	18	0.23	13
12	3226	0.0	0.96	1.76	25	1.75	20
13	3231	0.0	1.36	0.05	23	1.95	3
14	3237	0.0	1.84	0.94	13	6.25	23
15	3243	0.0	2.32	0.86	3	1.95	6
16	12494	180.0	0.48	3.91	8	2.08	20
17	12500	180.0	0.96	2.08	23	5.75	15
18	12505	180.0	1.36	0.23	25	2.18	6
19	12511	180.0	1.84	0.03	15	5.47	20
20	12517	180.0	2.32	0.60	20	1.59	3

Table 5.12: Values of the parameters for the 20 PVADs after 18,000 cost function evaluations, with the PVADs were arranged into 5 rings of 4 PVADs per ring.

PVAD No.	TMD Freq (Hz)	HR Freq (Hz)
1	85	442
2	273	145
3	69	168
4	54	240
5	134	145
6	70	428
7	122	307
8	104	235
9	78	249
10	64	173
11	107	76
12	211	211
13	35	223
14	154	398
15	148	223
16	315	229
17	230	382
18	77	235
19	28	372
20	124	200

Table 5.13: Approximate resonance frequencies of the 20 PVADs arranged into 5 rings of 4 PVAD per ring, after 18,000 cost function evaluations.

5.4 Performance vs Volume of Helmholtz Resonators

The results from section 5.2 showed how the APE inside the cylinder varied with the number of PVADs. Figure 5.17 shows the APE within the cylinder versus the total volume occupied by the PVADs, calculated by using Eq. (3.17). The results show that the greater the number of PVADs and hence the greater the volume, the lower the APE within the cylinder. Note that one of the 30 PVADs has a volume of 17 litres, which is the cause for 30 PVADs result to appear as an outlier. Figure 5.18 shows the APE versus the total PVAD volume, with the outlier result removed. The results show the trend that the greater number of PVADs, the lower the noise level inside the cylinder.

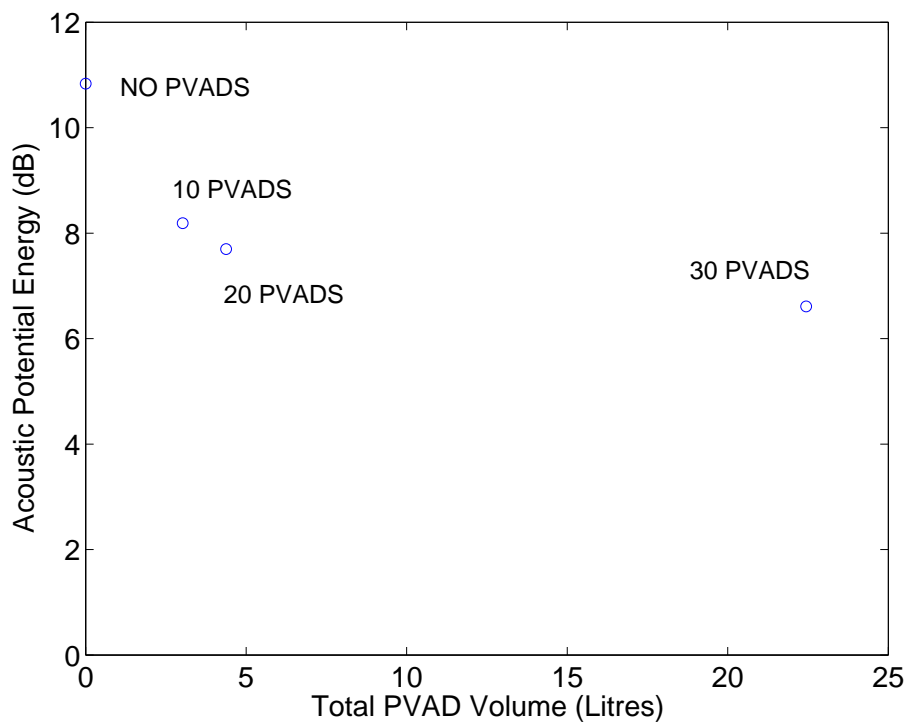


FIG. 5.17: Variation in acoustic potential energy with volume.

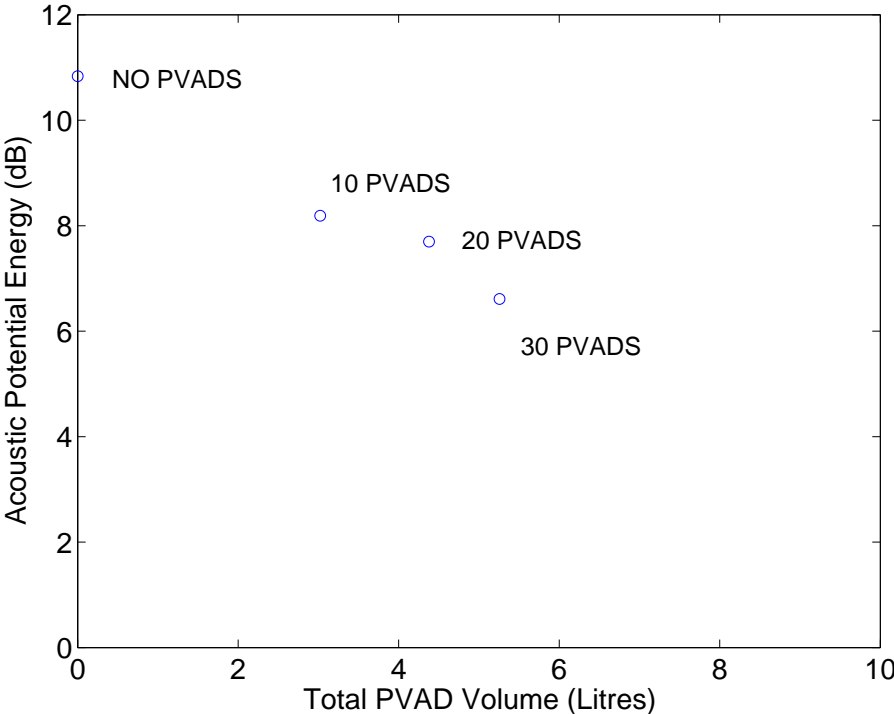


FIG. 5.18: Variation in acoustic potential energy with volume, after removing the outlier result.

5.5 Separating the Helmholtz Resonators and Tuned Mass Dampers

Up to now, it has been assumed that the location of the HR and the TMD reside at the same node. However, it is possible that better results could be achieved by separating the locations. Using the parameters for the mass, stiffness and damping for the HRs and TMDs another optimisation was conducted where the position of the HRs and TMDs were not constrained to be at the same location. The parameters of the PVADs are listed in Table 5.12.

Figure 5.19 shows the change in the cost function with evolution over 18,000 cost function evaluations.

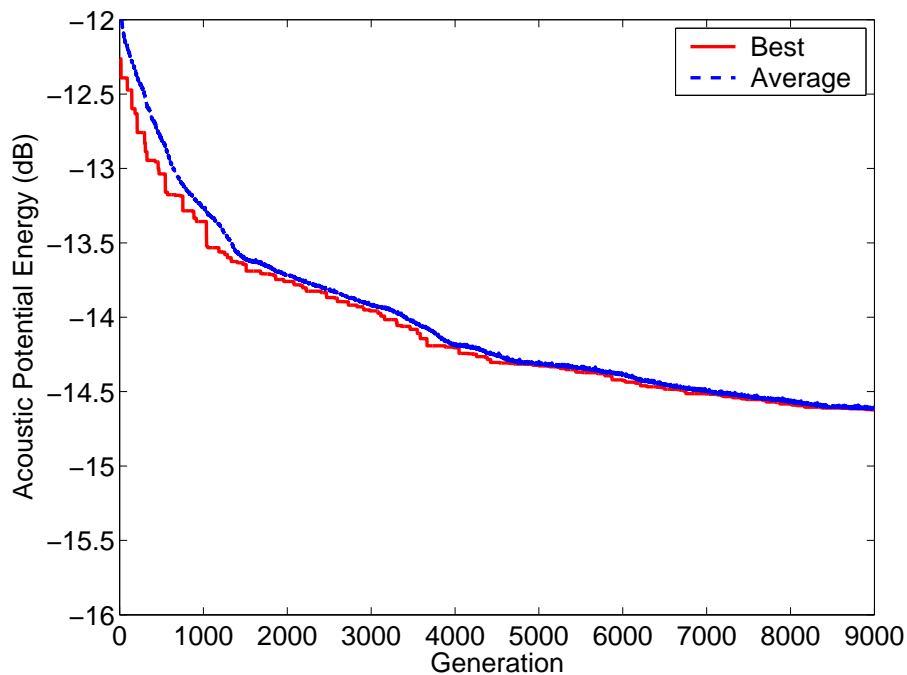


FIG. 5.19: Change in the cost function with each generation.

Figure 5.20 shows the acoustic potential energy versus frequency within the cavity at the end of the optimisation, after 18,000 cost function evaluations. Figure 5.21 shows the average acoustic potential energy. The results show that there is further noise reduction by separating the locations of the HRs and TMDs, compared to constraining the locations to 5 rings with 4 PVADs per ring.

The locations of the HRs and TMDs are shown in Figures 5.22 and 5.23, where the ‘o’ signs are the locations of the HRs and the ‘+’ signs are the locations of the TMDs.

Table 5.15 lists the approximate resonance frequencies of the 20 PVADs, based on the stiffness values in Table 5.14, and that the mass of the TMD and HR are 0.45kg and 0.01kg, respectively.

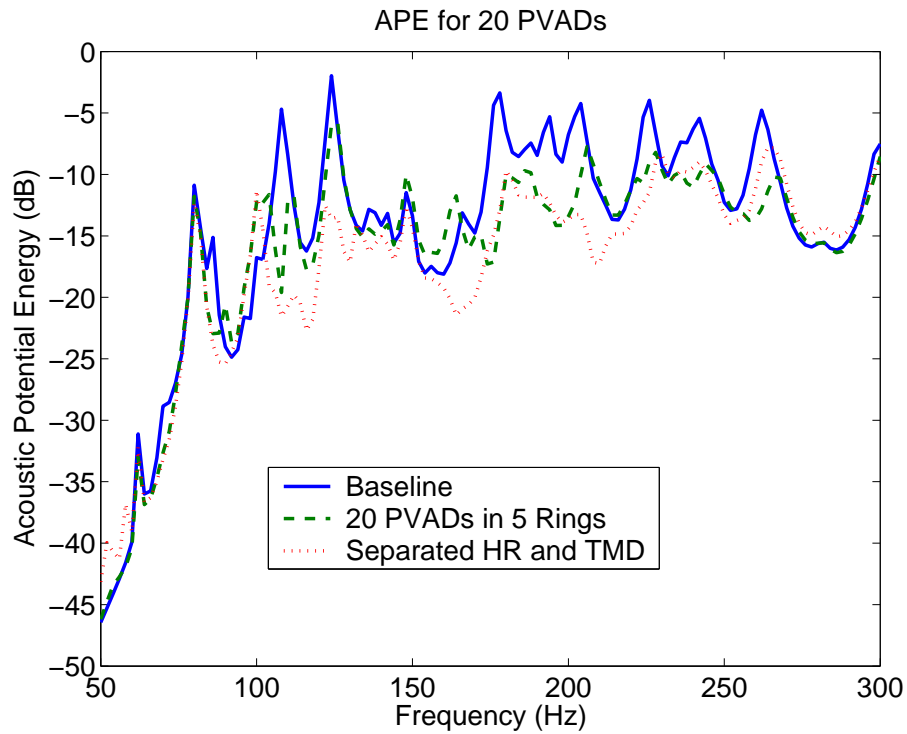


FIG. 5.20: Acoustic potential energy within the cavity without PVADs (Base), with 20 PVADs arranged into 5 rings with 4 PVADs per ring, and when location of the HR and TMD were permitted to vary independently.

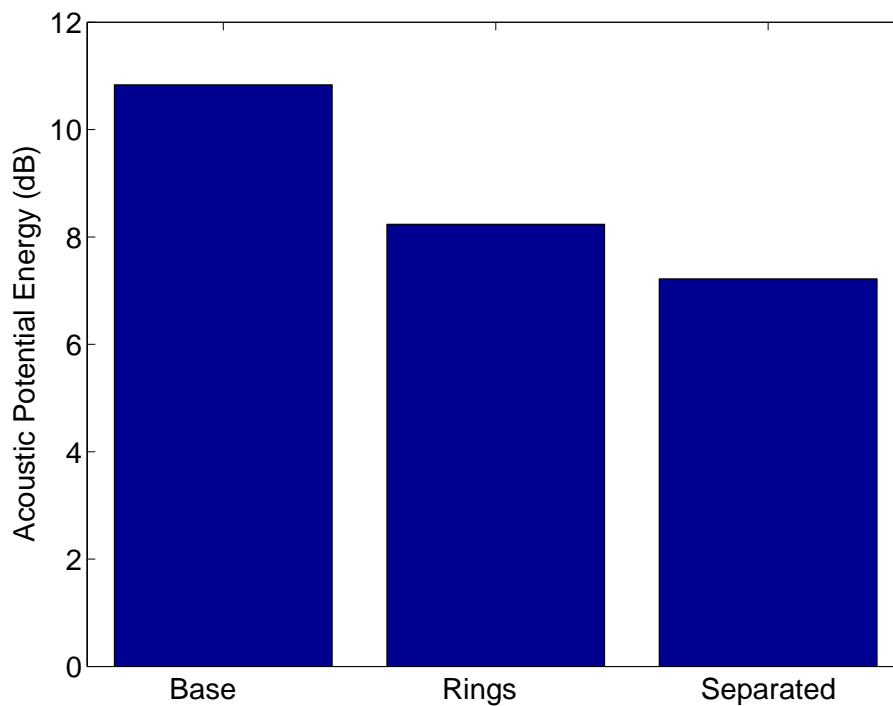


FIG. 5.21: Average acoustic potential energy within the cavity without PVADs (Base), with 20 PVADs arranged into 5 rings with 4 PVADs per ring, and when location of the HR and TMD were permitted to vary independently.

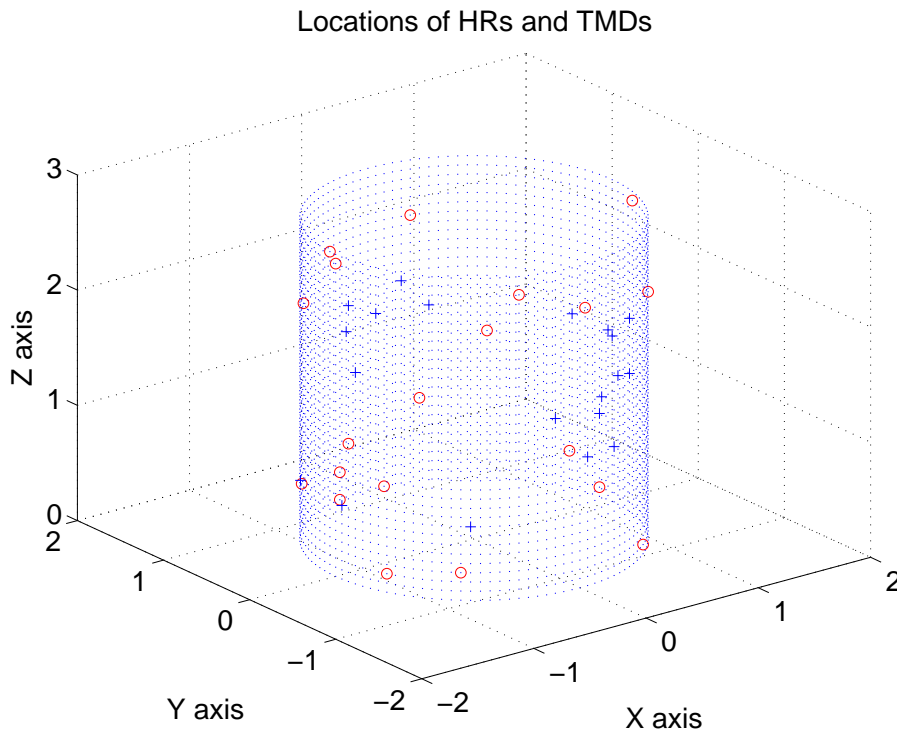


FIG. 5.22: Location of the 20 HRs (o) and 20 TMDs (+) after 18,000 cost function evaluations, displayed in three dimensions.

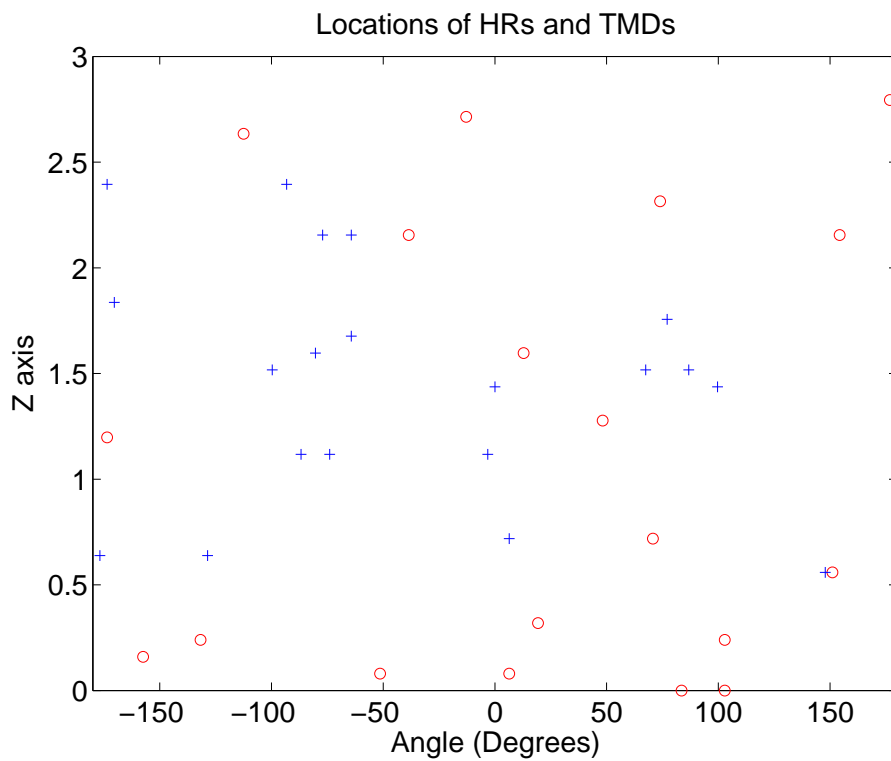


FIG. 5.23: Location of the 20 HRs (o) and 20 TMDs (+) after 18,000 cost function evaluations, displayed as if the surface of the cylinder was unwrapped.

PVAD No.	TMD					HR				
	Node	θ (degrees)	Z (m)	Stiffness ($\times 10^6$ N/m)	Damping (%)	Node	θ (degrees)	Z (m)	Stiffness ($\times 10^4$ N/m)	Damping (%)
1	27404	-86.8	1.12	0.29	25	33695	-112.5	2.63	7.70	13
2	7641	67.5	1.52	2.95	20	3385	6.4	0.08	0.83	13
3	3232	0.0	1.44	0.19	11	14801	151.1	0.56	1.11	15
4	18660	99.6	1.44	0.11	3	23043	-38.6	2.16	2.28	3
5	9950	77.1	1.76	0.70	6	33733	-131.8	0.24	0.83	3
6	20724	-3.2	1.12	0.20	23	3524	19.3	0.32	7.23	15
7	29398	-176.8	0.64	0.58	23	20846	-12.9	2.71	3.72	23
8	27342	-80.4	1.60	0.43	15	12442	176.8	2.79	2.18	8
9	29481	-170.4	1.84	0.24	6	25085	-51.4	0.08	2.45	6
10	27315	-77.1	2.16	0.16	13	14787	154.3	2.16	1.17	3
11	10049	86.8	1.52	0.45	18	3472	12.9	1.60	0.23	13
12	27268	-73.9	1.12	1.76	25	80	83.6	0.00	1.75	20
13	33772	-128.6	0.64	0.05	23	504	102.9	0.00	1.95	3
14	25241	-64.3	1.68	0.94	13	9869	70.7	0.72	6.25	23
15	14835	147.9	0.56	0.86	3	7706	48.2	1.28	1.95	6
16	3393	6.4	0.72	3.91	8	12522	180.0	2.71	2.08	20
17	29454	-173.6	2.39	2.08	23	18611	102.9	0.24	5.75	15
18	35461	-99.6	1.52	0.23	25	29439	-173.6	1.20	2.18	6
19	35540	-93.2	2.39	0.03	15	29324	-157.5	0.16	5.47	20
20	25247	-64.3	2.16	0.60	20	9923	73.9	2.32	1.59	3

Table 5.14: Values of the parameters for the 20 PVADs after 18,000 cost function evaluations, with the HRs and TMDs at separate locations.

PVAD No.	TMD Freq (Hz)	HR Freq (Hz)
1	85	442
2	273	145
3	69	168
4	54	240
5	134	145
6	70	428
7	122	307
8	104	235
9	78	249
10	64	173
11	107	76
12	211	211
13	35	223
14	154	398
15	148	223
16	315	229
17	230	382
18	77	235
19	28	372
20	124	200

Table 5.15: Approximate resonance frequencies for the 20 PVADs after 18,000 cost function evaluations, with the HRs and TMDs at separate locations.

The results in Figures 5.20 and 5.21 confirm the findings previously, greater benefit is obtained by allowing the location of the absorbers to vary, than constraining the location to 5 rings with 4 PVADs per ring. Comparison of Figures 5.7 and 5.21 shows that there is about 0.5dB reduction in the APE by allowing the HRs and TMDs to be at different locations.

5.6 Robust Design

One of the concerns is that the performance of the PVADs will be compromised by manufacturing tolerances and the air temperature at the launch site. PVADs that have low damping are likely to provide large attenuations if they are finely tuned to coincide with resonance frequencies, but might offer little benefit if the conditions are not exactly as intended. It is desirable to have a design that might not provide the best performance, but one that is likely to provide reasonable noise level reductions for a range of expected conditions. Hence the several analyses were conducted to examine the variation in APE with changes in

- the air temperature,
- the thickness of the cylindrical shell,
- the acoustic damping within the cylinder, and

An additional optimisation was conducted that had PVADs with high damping values for the TMDs and HRs.

5.6.1 Performance vs Temperature

It is of interest to examine how the APE within the cylinder varies with changes in the air temperature. For this analysis, three tests were done with the parameters listed in Table 5.12 with the air temperature at 0°C, 20°C, and 40°C. The density of air is given by the equation for the ideal gas law [18]

$$p = \rho RT \quad (5.1)$$

where p is the pressure, ρ is the density of the gas, R is the specific gas constant, and T is the absolute temperature. Using the standard values [18] for air of $\rho = 1.21 \text{ kg/m}^3$, $T = 20^\circ\text{C} = 293\text{K}$, $R = 287 \text{ Nm / (kg K)}$ then the pressure can be calculated as $p = 101.75 \times 10^3 \text{ Pa}$. The speed of sound in a gas varies as [7]

$$c = \sqrt{\frac{1.4p}{\rho}} \quad (5.2)$$

where c is the speed of sound in the gas. Hence using Eqs. (5.1) and (5.2), one can calculate the speed of sound and density of air for various temperatures, as listed in Table 5.16.

Temperature T	(°C)	0	20	40
Speed of Sound c	(m/s)	331	343	355
Density ρ	(kg/m ³)	1.30	1.21	1.13

Table 5.16: Speed of sound and density of air for various temperatures.

Modal analyses of the cavity were calculated for three temperatures listed in Table 5.16. Figure 5.24 shows the resonance frequencies of the cavity for the three temperatures.

Figure 5.25 shows the variation in the acoustic potential energy versus frequency for three temperatures 0°C, 20°C, and 40°C. Figure 5.26 shows the total acoustic potential

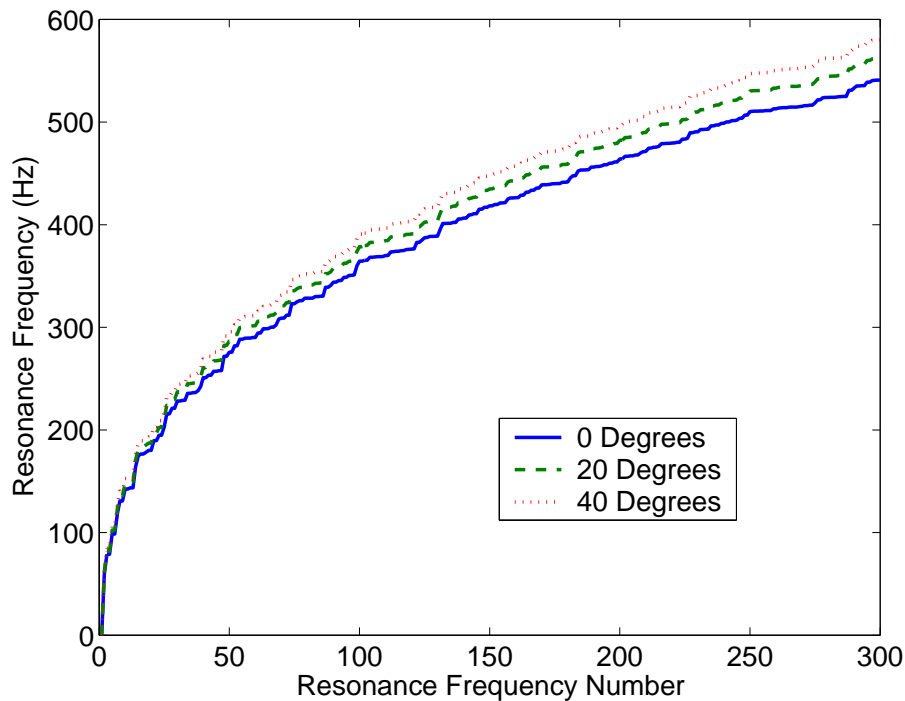


FIG. 5.24: Resonance frequencies of the cavity when the air temperature is 0°C, 20°C, and 40°C.

energy for three temperatures 0°C, 20°C, and 40°C. The results show that the change in air temperature causes a shift in the acoustic resonance frequencies of the cavity, and hence some of the PVADs are not tuned correctly. Figure 5.26 shows that at 40°C the APE within the cylinder is less than at 20°C, which is misleading. Inspection of Figure 5.25 shows that the peak in the APE curve around 300Hz at 20°C has shifted to a higher frequency at 40°C, and hence was not included in the cost function evaluation. If the analysis frequency range were extend to slightly above 300Hz, to include this peak, one would expect that the results would be the about the same overall as the 20°C result.

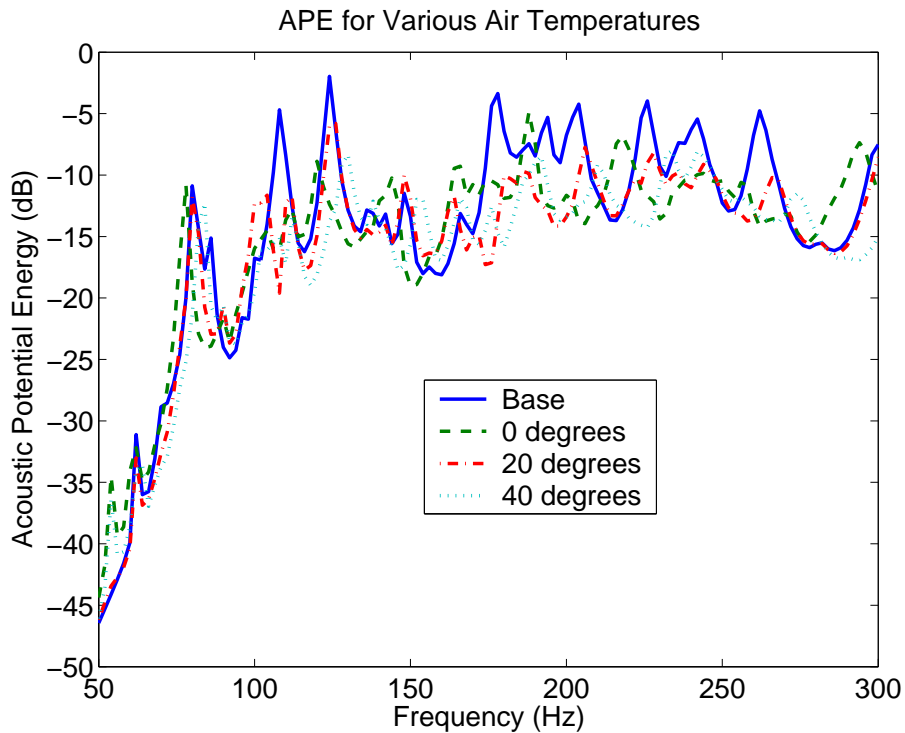


FIG. 5.25: Acoustic potential energy versus frequency, without PVADs (base), and with 20 PVADs arranged into 5 rings of 4 PVADs per ring when the air temperature is 0°C, 20°C, and 40°C.

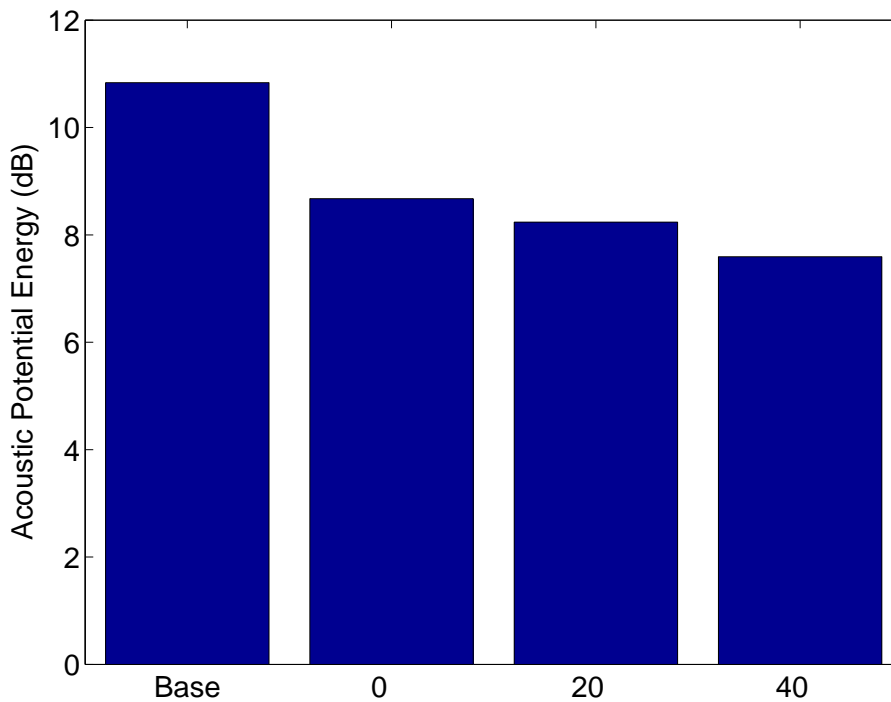


FIG. 5.26: Total acoustic potential without PVADs (base), and with 20 PVADs arranged into 5 rings of 4 PVADs per ring when the air temperature is 0°C, 20°C, and 40°C.

5.6.2 Performance vs Thickness of Shell

One could expect some variation in the thickness of the shell due to manufacturing and assembly tolerances. The parameters for the PVADs should be such that the APE within the cavity is relatively insensitive to the manufacturing and assembly tolerances. For this example, the parameters from Section 5.3 were used and the APE within the cylinder was recalculated for the nominal shell thickness, $\pm 1\text{mm}$ of the nominal shell thickness. The thickness of the core material was changed in the ANSYS model and modal analyses of the structure were recalculated for each shell thickness. The structural resonance frequencies for the three shell thicknesses are shown in Figure 5.27. Figure 5.28 shows the APE within the cylinder versus frequency for the three shell thicknesses, and Figure 5.29 shows the average APE within the cylinder versus the shell thickness. Examination of Figure 5.28 shows that changing the thickness causes some of the PVADs to be less effective in attenuating the APE within the cylinder. However the results in Figure 5.29 show that the average APE remains about the same for the various shell thicknesses examined.

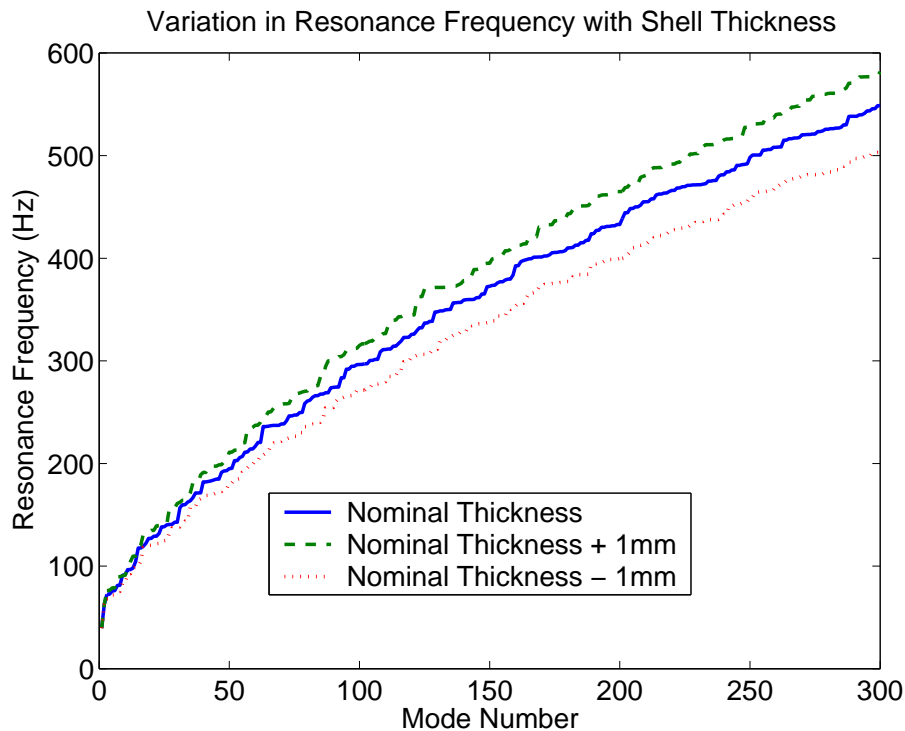


FIG. 5.27: Variation in the structural resonance frequencies for the nominal thickness, and and ± 1 mm of the nominal thickness.

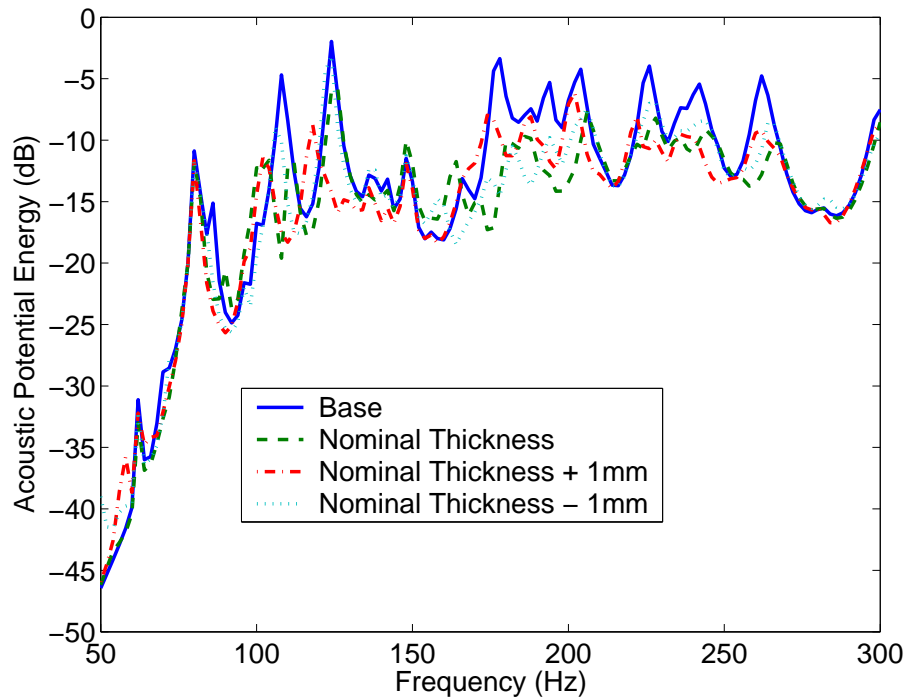


FIG. 5.28: APE versus frequency without PVADs (base), with 20 PVADs arranged into 5 rings with 4 PVADs per ring for the nominal shell thickness, and ± 1 mm of the nominal thickness.

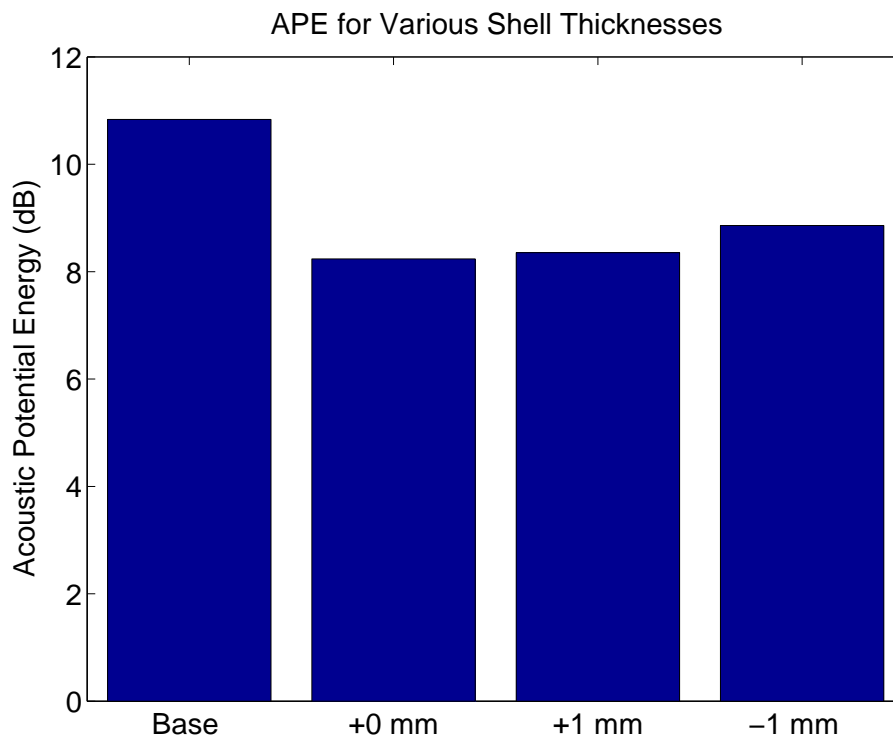


FIG. 5.29: Average APE within the cylinder for several shell thicknesses.

5.6.3 Performance vs Acoustic Damping

For this example, the parameters from Section 5.3 were used and the APE within the cylinder was recalculated when the acoustic damping within the cylinder was calculated for 2%, 5%, and 10%, and the results are shown in Figures 5.30 and 5.31. It is not surprising that changing the acoustic damping inside the cylinder provides the greatest reduction in APE within the cavity, compared to any of the methods examined thus far.

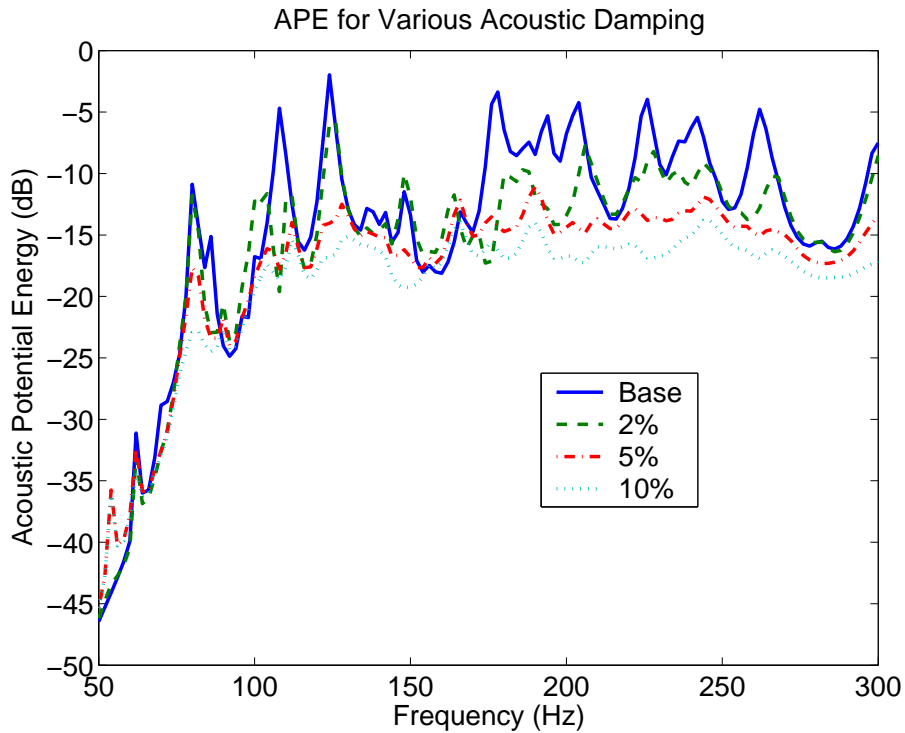


FIG. 5.30: APE versus frequency without PVADs (base), with 20 PVADs arranged into 5 rings with 4 PVADs per ring for various acoustic damping values inside the cylinder.

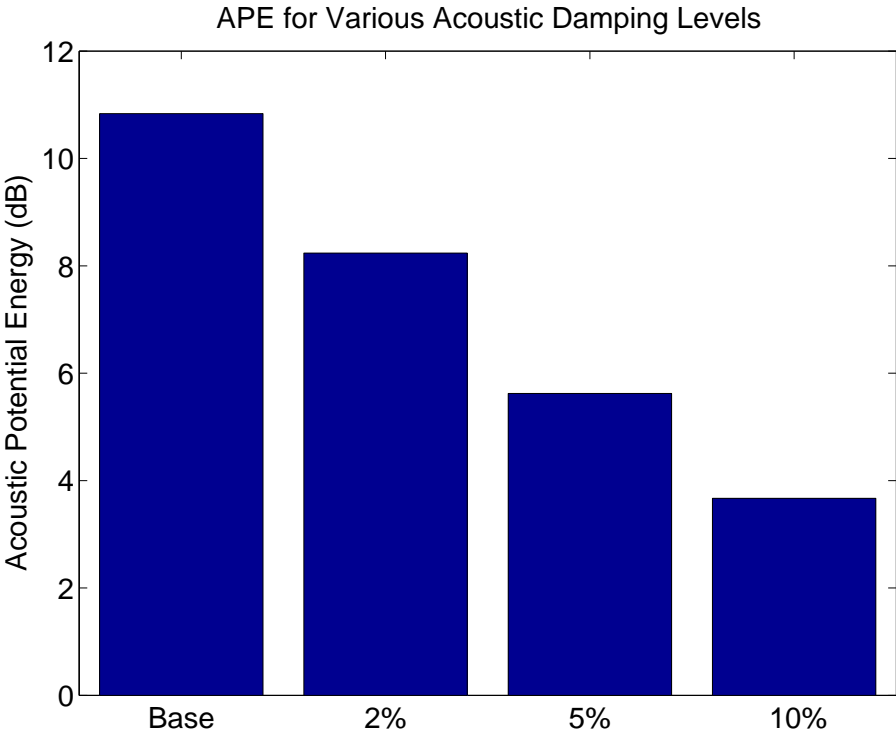


FIG. 5.31: Average APE within the cylinder for various acoustic damping values inside the cylinder.

5.6.4 Performance with Highly Damped PVADs

The researchers at Kirtland Airforce base are concerned with the ‘robustness’ of the designs. That is the parameters of the PVADs should provide acceptable noise reduction over the range of expected operating conditions, and manufacturing tolerances. One method is to use HRs and TMDs that have high damping, that do not provide as much attenuation as devices with light damping and precisely tuned to the resonance frequencies of the cavity and structure, however it will provide a reasonable attenuation over a broad frequency range.

An optimisation was done over 18,000 cost function evaluations with the damping parameters for the HRs and TMDs fixed at 25%, the location of the 20 PVADs was fixed into 5 rings with 4 PVADs per ring, the mass was fixed and the stiffness was optimised. A summary of the parameters that were fixed and variable is listed in Table 5.17.

PVAD parameter	Min	Max	No Values	Comment
PVAD position	-	-	0	Fixed
Mass-spring frequency	11	510	500	[Hz]
Mass-spring damping (η)	0.25	0.25	0	Fixed
Acoustic resonator frequency	11	510	500	[Hz]
Acoustic resonator damping (η)	0.25	0.25	0	Fixed

Table 5.17: PVAD parameter range for the optimisation of the Boeing cylinder, for 20 PVADs arranged into 5 rings with 4PVADs per ring, with the HRs and TMDs set with high damping.

Figure 5.32 shows the change in the cost function versus the generation. Figure 5.33 shows the APE within the cavity without the PVADs, and when there are 20 PVADs arranged into 5 rings of 4 PVADs per ring, with high damping for the HRs and TMDs. Figure 5.34 shows the average APE within the cylinder when there were no PVADs (Base), when the PVADs were arranged into 5 rings of 4 PVADs per ring and optimised damping, and when the damping was fixed at 25%. The results show that there was no change in the noise reduction, which indicates that this is a robust solution.

5.6.5 Summary of Robust Designs

The results presented in section 5.6 show that the APE within the cylinder varies less than 1dB for temperature changes of $\pm 20^\circ\text{C}$ about an ambient air temperature of 20°C , less than 1dB for changes in the thickness of the cylinder by $\pm 1\text{mm}$, and less than 0.1dB by fixing the damping of the HRs and TMDs to 25%. The greatest noise reduction was achieved by increasing the acoustic damping level inside the cylinder from 2% to 10%, which reduced the APE by 4dB.

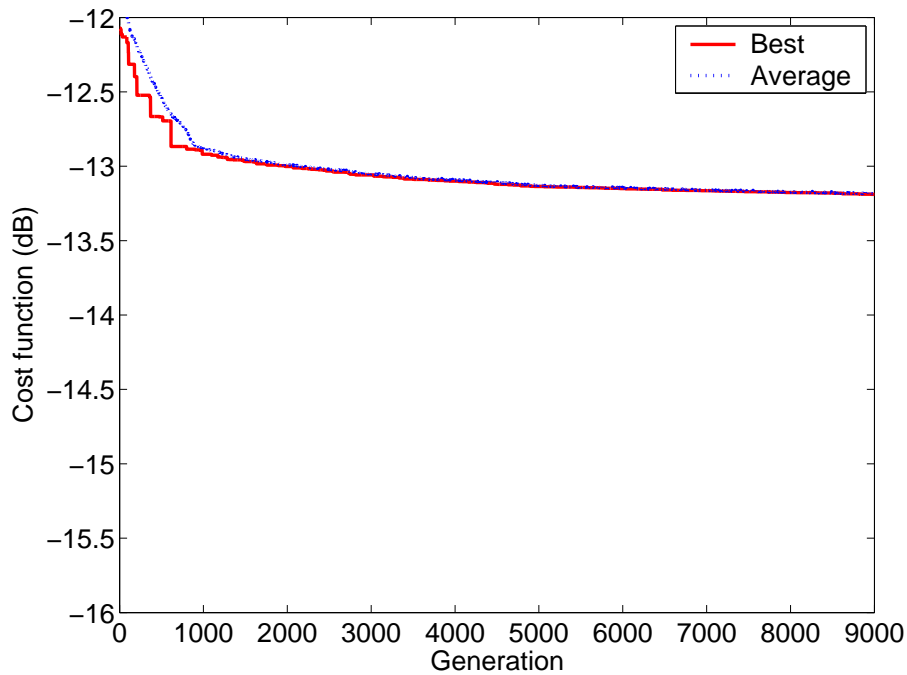


FIG. 5.32: Change in the cost function with each generation.

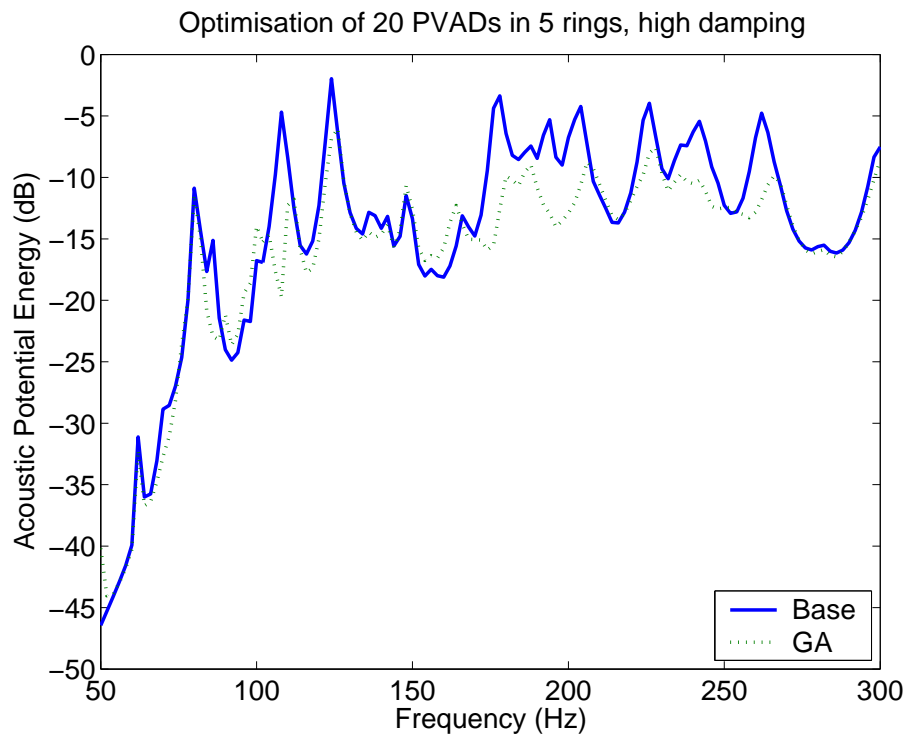


FIG. 5.33: Acoustic potential energy within the cavity without the PVADs, and when there are 20 PVADs arranged into 5 rings of 4 PVADs per ring, with high damping for the HRs and TMDs.

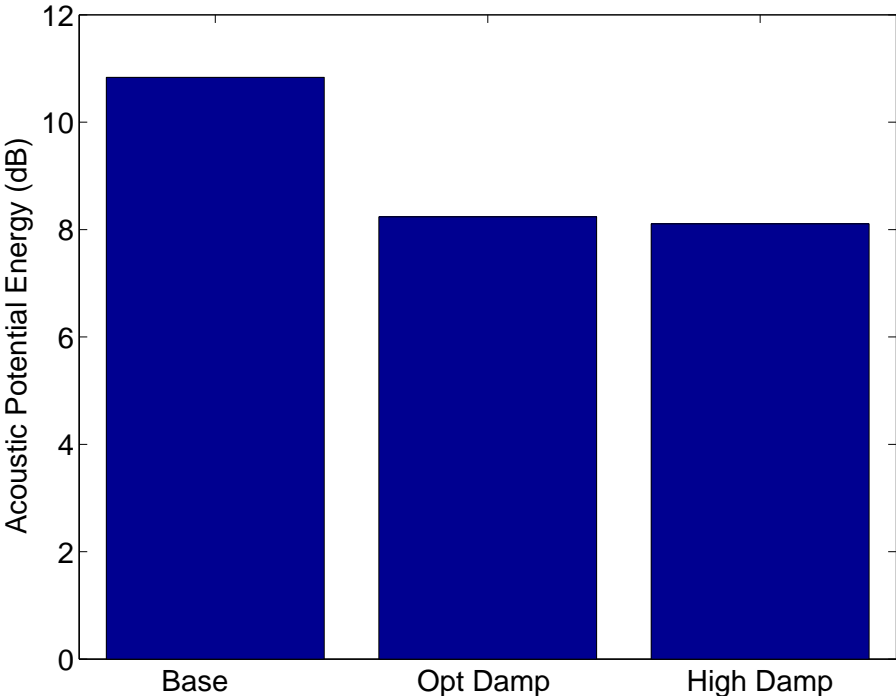


FIG. 5.34: Average APE within the cylinder for 20 PVADs arranged into 5 rings with 4 PVADs per ring when the damping was optimised, and when the damping was fixed at 25%.

Chapter 6

Conclusions

6.1 Summary

In summary, the work that completed in Stage 3A was

- The coupling of the TMDs and HRs was re-formulated. The new mathematical framework can handle multiple degree of freedom TMDs and HRs.
- A distributed computing network was developed using the Condor software suite, which enabled the optimisations to be completed 25 times faster than using a single computer. Optimisation that would have taken 75 days to complete on a single computer were completed in 3 days using the distributed computing network.
- Several GA implementations were modified from publicly available Matlab toolboxes. The scripts were modified to implement synchronous and asynchronous parallel GAs.
- Many comparisons were made between the Matlab modal coupling software and fluid-structure interaction finite element models, to demonstrate that the Matlab software can correctly predict the sound pressure level of the acoustic space and vibration level of the structure.
- The ANSYS-to-Matlab interface code was re-written for use with ANSYS V7.0.
- The entire Matlab modal coupling software was re-written to make use of structures - a Matlab term that describes the collation of information into a single object. This makes the Matlab scripts easier to understand for a person reading the code.

6.2 Future Work

Through the work that has been completed in this stage of the project, several issues have been raised which should be addressed in the stage 3B.

6.2.1 Pseudo-static correction term

During the testing of the modal coupling software it was shown that the analysis must include modes with resonance frequencies much higher than the frequency range of interest to obtain accurate results. Previous researchers [4] have suggested that the modal analysis

should be conducted up to two octaves higher than the frequency range of interest. This is a problem common to all modal methods where only a truncated set of modes is used. The problems with modal truncation have been recognised since the early 1970's from modal analysis. Methods have been developed to include the effects of modes outside the frequency range of interest, and often involve applying a residue or pseudo-static correction term to the modal sum [19, 20]. A few authors have examined the problems that occur with coupled vibro-acoustic systems. The authors conclude that without a correction factor, almost all the available modes from a finite element analysis must be included in a modal summation method [21].

The next stage of the project should implement a pseudo-static correction factor to the modal summation. This will reduce the number of modes that need to be considered in an analysis and hence the calculation times will be shorter than if a large number of modes are used in the analysis.

Other researchers [22] have considered modifying the original matrix formulation of unsymmetric matrices into a symmetric matrix formulation, which means that the symmetric matrix solvers can be used that are significantly faster than unsymmetric matrix solvers. However, this modification still does not improve the effect caused by modal truncation, and a large number of modes must still be included in the analysis.

6.2.2 Modal Analysis

The current method of calculating the cost function involved modifying the matrices to form matrices that couple the Helmholtz resonator to the acoustic space and the Tuned Mass Damper to the structure. At each solution frequency, a matrix inversion occurs to calculate the modal participation factors. The modal participation factor is then used to calculate the acoustic potential energy within the cavity.

It might be possible to only perform a single matrix inversion for all frequencies to determine the resonance frequencies, and then determine a curve fitted solution to calculate the acoustic potential energy over the entire analysis frequency range. This technique is similar to those used in modal analysis.

6.2.3 Revised Coding of the Genetic Algorithm

The parallel genetic algorithm that was used in this work was developed by modifying a publicly available Matlab toolbox so that the cost function evaluations could be distributed to slave processors. The physical parameters, such as stiffness, damping etc, were 'coded' into a range from 1 to an integer value, and then converted into a binary string. The current method of coding the numerous parameters for the HR and TMD is somewhat cumbersome, similar to the state of the Matlab modal coupling code in Stage 2. The manner in which the parameters are described should be formed into a 'structure' - a computer programming term for grouping similar things together, so that the code is more easily understood.

6.2.4 Validity of Modal Coupling with High Modal Density

Several test cases have been conducted to compare the predicted pressure inside a cavity with flexible walls, using the Matlab modal coupling theory and fully coupled ANSYS finite element models. The results have shown that when the dimensions of a rectangular

box are dissimilar, hence there is a wide separation in resonance frequencies and low modal density, that there is good agreement between the two methods. However, when the dimensions of the box are almost square, and hence there is high modal density, there is poor agreement between the two methods. There has been little research to investigate this phenomena, and it warrants further investigation to ensure that the predictions are accurate.

6.3 Plans

This section contains a proposal for the tasks to be completed in Stages 3B and 4 of the project. The tasks for Stage 4 should be re-examined after the completion of Stage 3B.

6.3.1 Stage 3B

1. Address any unexpected issues raised in the Stage 3A work

In the proposal for task 3A it was stated that if necessary and if time permitted, a re-evaluation of the modal coupling technique would be undertaken. It has since become clear that this work is necessary and that all of the time allocated to Stage 3A will be taken up with the other tasks outlined in that work statement and the re-evaluation of the modal coupling technique will need to be part of stage 3B. A possible approach to this task may be to rewrite the modal coupling code to perform a coupled eigenvalue analysis, giving the coupled natural frequencies.

The tasks that will be undertaken are:

- investigate the implementation of a symmetric matrix formulation for the modal coupling method. Symmetric matrices are faster to invert than non-symmetric matrices, and hence the response of the vibro-acoustic system will be evaluated faster than currently.
- investigate the implementation of pseudo-static correction factors to account for modes outside the analysis frequency range.
- compare the integer and binary representations of the chromosomes and determine which method converges to the optimum solution the fastest.

(Estimated duration: 1 month).

2. Feasibility of Stage 4 Tasks

Preliminary work will be undertaken on Stage 4 tasks 2, 3 and 4 with a view to confirming the feasibility of the proposed approach and investigating the possibility of using alternative approaches to the absorber design and evaluation tasks, which may be preferable to the approach proposed initially.

(estimated duration: 1.5 months)

3. Report for Stage 3B

(estimated duration: 0.5 month)

Total time for stage 3B: 3 months

6.3.2 Stage 4

1. RSLVF Optimal and Sub-optimal Performance Evaluation

The design tools developed in stage 3 will be applied the RSLVF fairing model. The reduction of interior noise levels shall be investigated for different design approaches for the RSLVF. Performance of the tools shall be assessed. The investigation shall include the performance of VADs, which represent vibration and acoustic absorbers at the same location, the possible benefit of separating them shall be investigated.

(estimated duration: 9 months)

2. Optimal design of multi-degree-of-freedom vibro-acoustic absorbers

The design of a multi-degree-of-freedom vibro-acoustic absorber with rocking modes and a twisting mode in addition to the normal translational modes will be investigated. Key design issues shall be identified and design techniques developed.

(estimated duration: 9 months)

3. Incorporation of Practical Phenomenon into the Modeling and Design Process

Having developed efficient computation methods in task 4.1, and having developed improved PVAD devices in task 4.2, the effects of the following practical phenomena will be investigated:

- structural anomalies including a vent, a separation seam, and/or a variation in the boundary conditions, and
- Acoustic fill including the determination of the effect of having a rigid payload and a resonant payload in the interior volume.

(estimated duration: 6 months)

4. Incorporation of Measured Data into Modeling and Design Tools

The FE modal data will be replaced with actual measured modal data for the structure, cavity and VADS to provide a more accurate prediction of the performance and determine the optimal configuration of VADS for best performance.

(estimated duration: 7 months)

5. Final Report

A final report documenting Stage 4 results and providing a summary of relevant earlier stage work will be prepared.

(estimated duration: 1 month).

(Stage 4 total estimated duration: 32 months)

Appendix A

Dirac Delta Function Properties

The model of the Tuned Mass Dampers used in this report assumes that they vibrate only along one translational axis. It is possible to extend the mathematical framework to include multiple degrees of freedom, including torsional vibration. To include torsional vibration, one can convert point moments into force couples using Dirac delta functions as described below. The force couples are then applied to the model the same way as the translational forces are applied to the model as described in this report. References [2, 6] provide further details.

1. Figure A.1 shows a point force F_z acting in the Z direction on point $\sigma_J(x_J, y_J)$ on a support structure which is equivalent to a distributed load $F_z \delta(x - x_J, y - y_J)$.

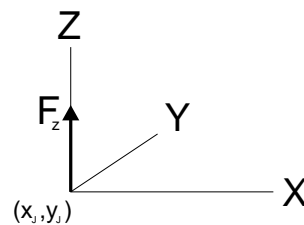
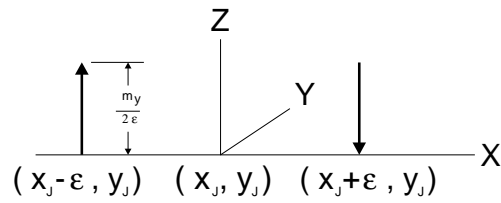


FIG. A.1: Point force F_z

2. Figure A.2 shows a point moment M_y , around the Y axis, which is equivalent to a pair of point forces in the Z direction of $\frac{M_y}{2\epsilon} \delta(x - x_J + \epsilon, y - y_J)$ and $-\frac{M_y}{2\epsilon} \delta(x - x_J - \epsilon, y - y_J)$ when $\epsilon \xrightarrow{\text{lim}} 0$, they correspond to a distributed load

$$\begin{aligned} & \lim_{\epsilon \rightarrow 0} \frac{M_y}{2\epsilon} \delta(x - x_J + \epsilon, y - y_J) - \frac{M_y}{2\epsilon} \delta(x - x_J - \epsilon, y - y_J) \\ & \rightarrow M_y \frac{\partial \delta(x - x_J, y - y_J)}{\partial x} \end{aligned} \quad (\text{A.1})$$

FIG. A.2: Point moment M_y

3. Similarly, a point moment around the X axis, M_x , is equivalent to a distributed load in the Z direction

$$-M_x \frac{\partial \delta(x - x_J, y - y_J)}{\partial y} \quad (\text{A.2})$$

4. Integral of Dirac delta functions

$$\int_{\sigma} \Gamma_k(\sigma) \delta(\sigma - \sigma_J) d\sigma = \Gamma_k(\sigma_J) \quad (\text{A.3})$$

5. Integral of the partial derivatives of Dirac delta functions

$$\begin{aligned} & \int_{\sigma} \Gamma_k(\sigma) \frac{\partial \delta(\sigma - \sigma_J)}{\partial x} d\sigma \\ &= \lim_{\epsilon \rightarrow 0} \int_{\sigma} \frac{1}{2\epsilon} \Gamma_k(\sigma) \left\{ \delta(x - x_J + \epsilon, y - y_J) \right. \\ & \quad \left. - \delta(x - x_J - \epsilon, y - y_J) \right\} d\sigma \\ &= \lim_{\epsilon \rightarrow 0} \frac{1}{2\epsilon} \{ \Gamma_k(x_J - \epsilon, y_J) - \Gamma_k(x_J + \epsilon, y_J) \} \\ &= -\frac{\partial \Gamma_k(\sigma_J)}{\partial x} \\ &= -\Gamma_{kx}(\sigma_J) \end{aligned} \quad (\text{A.4})$$

Appendix B

PC Specifications of the Condor Pool

The pool of computers that was used to run the simulations is operated by the Computer Aided Teaching Suite (CATS) within the Faculty of Engineering. There are several types of computers that are operated, and are listed below:

PC Suite A 15 PCs running Windows XP Professional. 15 Compaq Deskpros - PIII-866. 256Mb RAM 16Mb Graphics 17" Monitors 1 Compaq Deskpro - PII - 350MHz 512Mb RAM with Windows 2000 This suite is for group work and specialist applications.

PC Suite B 40 PCs running Windows XP Professional 40 Compaq Evos - P4 - 1.5GHz. 512Mb RAM 16Mb Graphics 17" Monitors, CD Burner.

PC Suite C 40 PCs running Windows XP Professional 40 Compaq Evos - P4 - 1.5GHz. 512Mb RAM 16Mb Graphics 17" Monitors, CD Burner.

PC Suite D 30 PCs running Windows XP Professional 30 Compaq Evos - P4 - 2.4GHz 512Mb RAM 64Mb Graphics 17" monitors.

PC Suite E 30 PCs running Windows XP Professional 30 Compaq Evo's P4 - 2.4GHz 512Mb RAM 64Mb Graphics 17" monitors.

Appendix C

Symbols

C.1 Acronyms

APE	Acoustic Potential Energy
CATS	Computer Aided Teaching Suite
DOF	Degree of Freedom
FEA	Finite Element Analysis
FSI	Fluid-Structure Interaction
GA	Genetic Algorithm
GAOT	Genetic Algorithm Optimisation Toolbox
HR	Helmholtz Resonator
MPI	Message Passing Interface
PVAD	Passive Vibro-Acoustic Device
SPL	Sound Pressure Level
SUS	Stochastic Universal Sampling
TMD	Tuned Mass Damper

C.2 List of Symbols

ψ	matrix of structural mode shapes
ϕ	matrix of acoustic mode shapes
η	loss factor
A	area
$\mathbf{A}_{11} \cdots \mathbf{A}_{22}$	sub-matrices to couple the TMDs to the structure
$\mathbf{B}_{11} \cdots \mathbf{B}_{22}$	sub-matrices to couple the HRs to the acoustic cavity
\mathbf{D}_0	displacement vector of the TMD
\mathbf{F}	modal force
F_c	force that is applied by the structure to the TMD
F_1	force that is directly applied to the TMD
j	complex number = $\sqrt{-1}$
k	stiffness
\mathbf{Q}	volume velocity
\mathbf{v}	velocity
x	displacement
x_0	displacement of the acoustic mass inside the neck of the HR
Z_0	impedance of the TMD isolator
\mathbf{Z}_a	structure to acoustic transfer function
\mathbf{Z}_b	acoustic to structure transfer function
\mathbf{Z}_I	structural modal input impedance
\mathbf{Z}_q	acoustic modal input impedance that couples the interior volume velocity sources and the regeneration of sound from sources to the structure back to the cavity

Appendix D

Checking the Models

D.1 Introduction

The modelling of Helmholtz resonators (HRs) and Tuned Mass Dampers (TMDs) involves creating a mathematical model of these devices, and developing an independent method to check that the mathematical model correctly predicts the response. It was decided early in the project that ANSYS would be used to conduct a full fluid-structure interaction analysis and the results would be compared with the results from the Matlab code of the modal coupling theory.

The processes of mathematical modelling and subsequent testing was completed in stages, which were:

- Tuned mass damper: single and multiple
- Helmholtz resonator: single and multiple
- TMD and HR: single and multiple

The mathematical modelling and testing that occurred in these stages is discussed below.

D.2 Tuned Mass Dampers

Several cases were analysed and the details are listed in Table D.1. For Case 7, two TMDs were attached to the plate with the details listed in Table D.2. A force $F_z = 1\text{N}$ was applied at node 673 in all cases. Case 4 was without any TMD attached to the structure.

Case	Node	k (N/m)	m (kg)	Freq (Hz)
1	808	852.35×10^3	50	20.78
2	808	6.6×10^6	50	57.82
3	808	17.047×10^3	1	20.78
4	-	-	-	-
6	880	8.6223×10^6	5	209

Table D.1: Details of the cases analysed for testing the modelling of TMDs.

TMD	1	2
Node	808	880
k (N/m)	6.6×10^6	8.6223×10^6
m (kg)	50	5

Table D.2: Details of the two TMDs for Case 7.

Figure D.1 shows the velocity of structure at node 808, for the MATLAB modal coupling theory and the ANSYS model, when no TMDs were attached to the structure. This result can be considered the baseline response of the structure. Alternative baseline configurations could be: a plate of equally distributed mass that has a total mass of the plate and the mass of the TMD, or a plate that has the mass attached to the plate at the attachment point of the TMD.

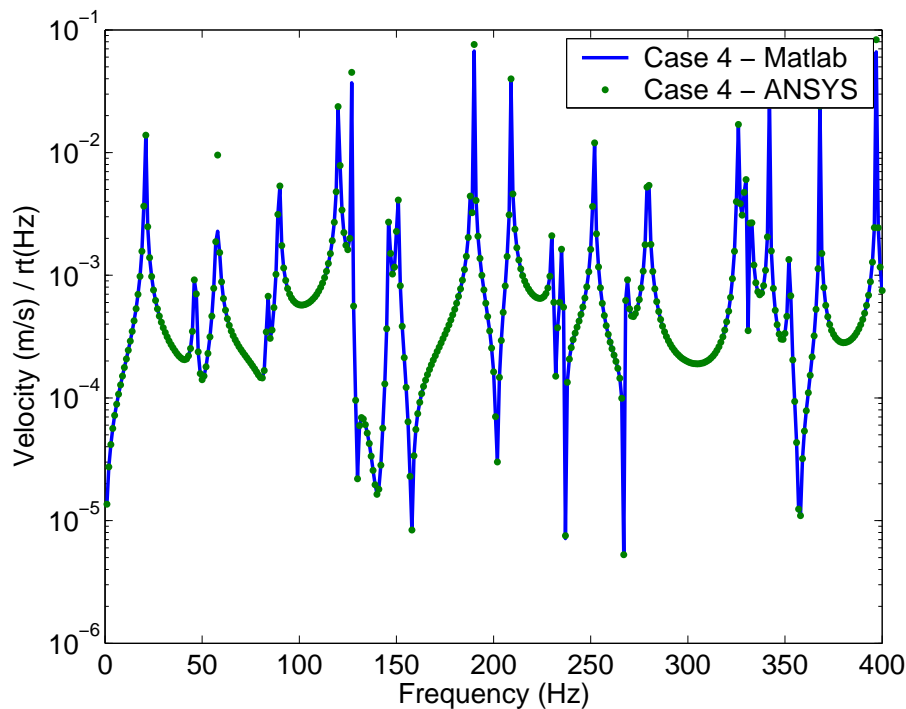


FIG. D.1: Comparison of the MATLAB and ANSYS models for Case 4, without any TMD attached to the plate.

Figure D.2 shows the velocity of structure at node 808, for the MATLAB modal coupling theory and the ANSYS model. Comparison of Figures D.1 and D.2 show that there is a large decrease in the velocity at about 20Hz, that coincides with the resonance frequency of the TMD.

Figure D.3 shows the velocity of structure at node 808, for the MATLAB modal coupling theory and the ANSYS model for case 2. The results show that there is a large decrease in the velocity at about 57Hz, that coincides with the resonance frequency of the TMD. At frequencies above 170Hz, the results from the two methods do not compare favourably. This is because the number of modes included in the analysis is insufficient to account for the energy within the system. The TMD acts to alter the impedance of the structure at a point, which is similar to applying a point force to the structure. Energy

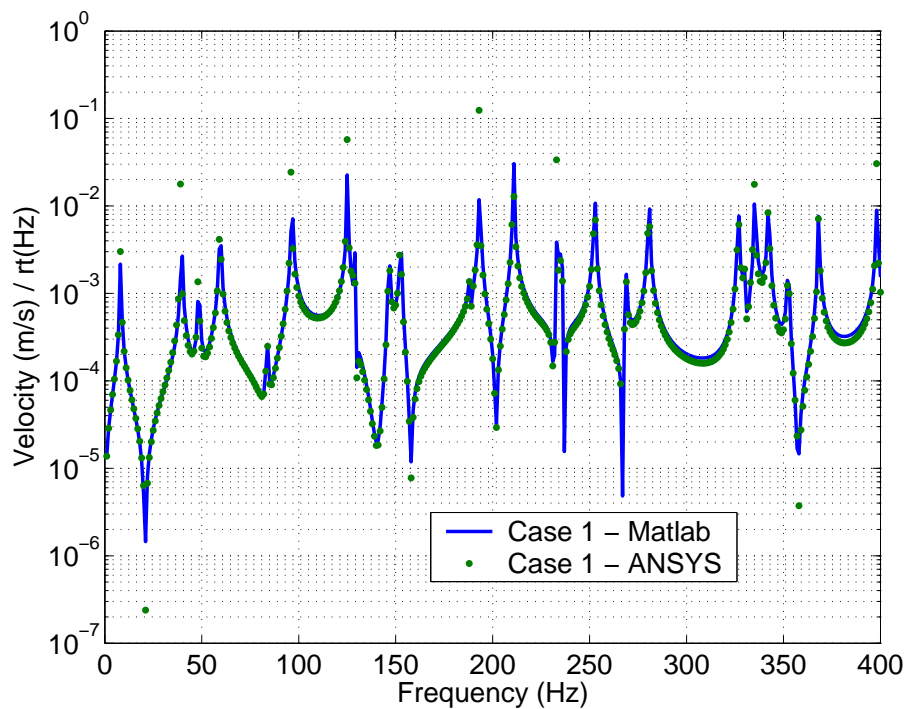


FIG. D.2: Comparison of the MATLAB and ANSYS models for Case 1, where a TMD is attached that has a resonance frequency of 20.8Hz.

flows from the point into the structure. In the calculation of the response of the structure, a modal superposition technique is used and energy can only be transferred into the modes that are included in the analysis. Hence if an insufficient number of modes are included, then the response of the structure will be under-predicted. Another way of considering this is that the Matlab model of the structure will be too 'stiff' compared to the ANSYS model, and hence the resonance frequencies for the MATLAB model will be slightly higher than the ANSYS model. Figure D.4 shows a similar plot to Figure D.3, except modes up to 2000Hz were included in the modal analysis, and the results show that the response at all frequencies has better agreement than when only modes up to 400Hz were used in the modal superposition. It has been found that the modal analysis should be conducted to include frequencies that are at least two octaves higher than what is intended to be presented in the results. (An octave is a doubling of frequency.) For example, if results up to 400Hz are to be presented, then one should conduct modal analyses to include frequencies up to $400 \times 2 \times 2 = 1600\text{Hz}$.

Figure D.5 shows the response of the plate at node 880 for Case 6, when a TMD with a resonance frequency of 209Hz was attached to the plate at node 880, and modes up to 1600Hz were included in the analysis. The results show that there is some degradation in the agreement at frequencies above 370Hz. Figure D.6 shows the response at a random location, node 1000, also has good agreement.

The results presented so far show that there is good agreement between the mathematical model that was realised in MATLAB, and the ANSYS model that uses the full harmonic analysis. The next step in the tests is to analyse a structure with more than 1 TMD to ensure that the mathematics and the MATLAB code work correctly.

Analyses were conducted using 2 TMDs, as described in Case 7 and Table D.2.

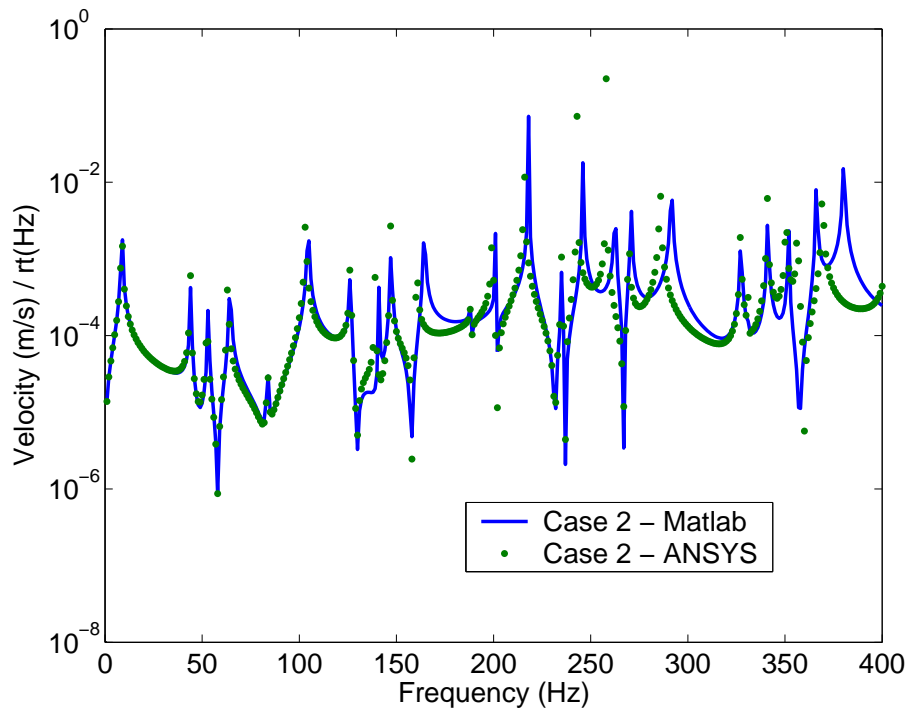


FIG. D.3: Comparison of the MATLAB and ANSYS models for Case 2, where a TMD is attached that has a resonance frequency of 20.8Hz, and only modes up to 400Hz were included in the modal analysis.

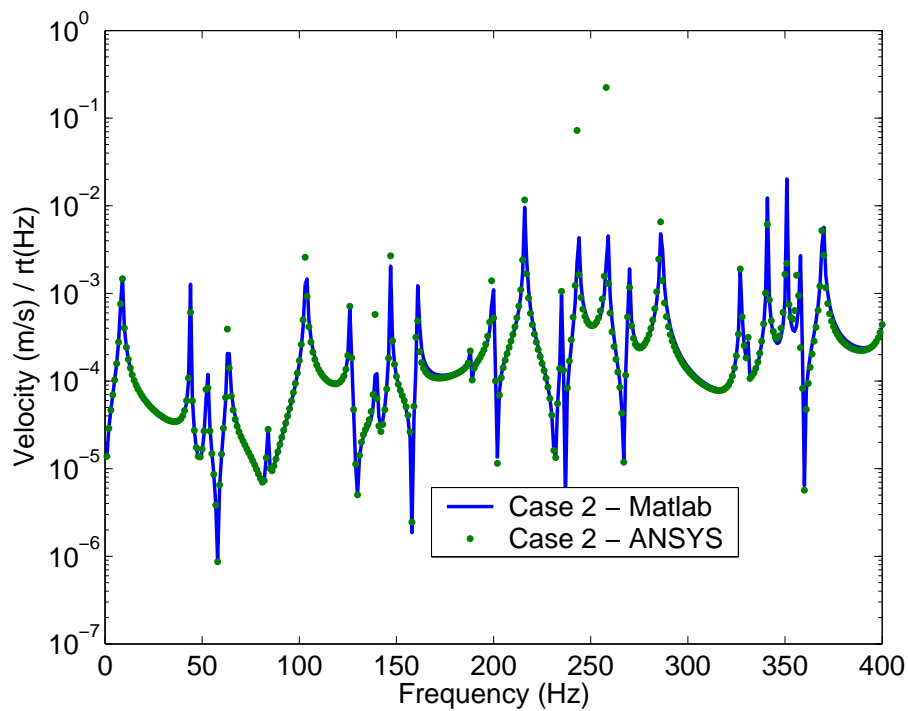


FIG. D.4: Comparison of the MATLAB and ANSYS models for Case 2, where a TMD is attached that has a resonance frequency of 20.8Hz, and only modes up to 2000Hz were included in the modal analysis.

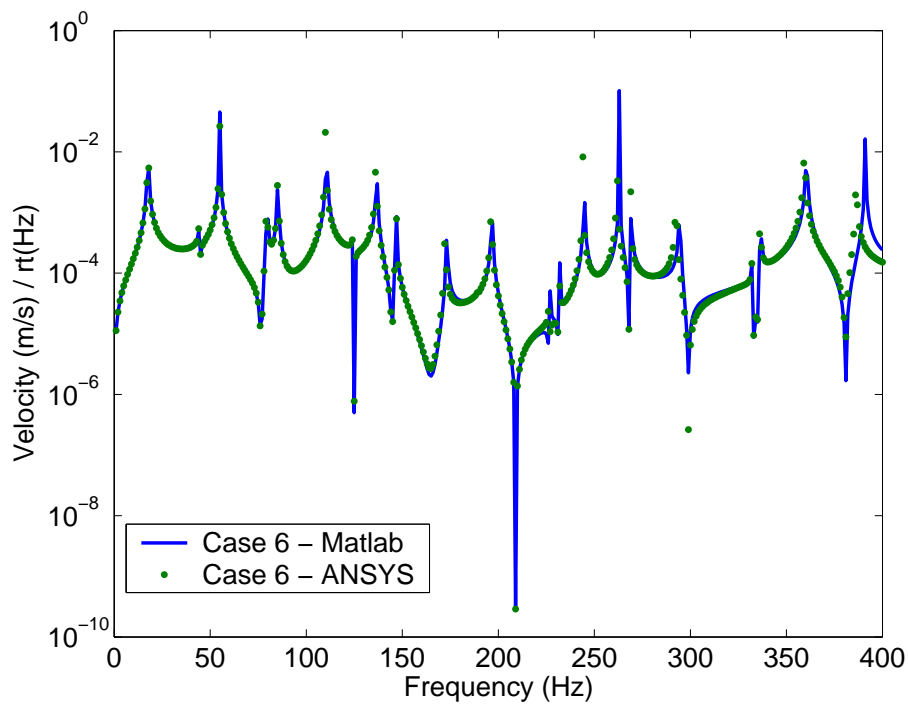


FIG. D.5: Velocity of the plate at node 880 for the MATLAB and ANSYS models for Case 6, where a TMD is attached that has a resonance frequency of 209Hz, and only modes up to 1600Hz were included in the modal analysis.

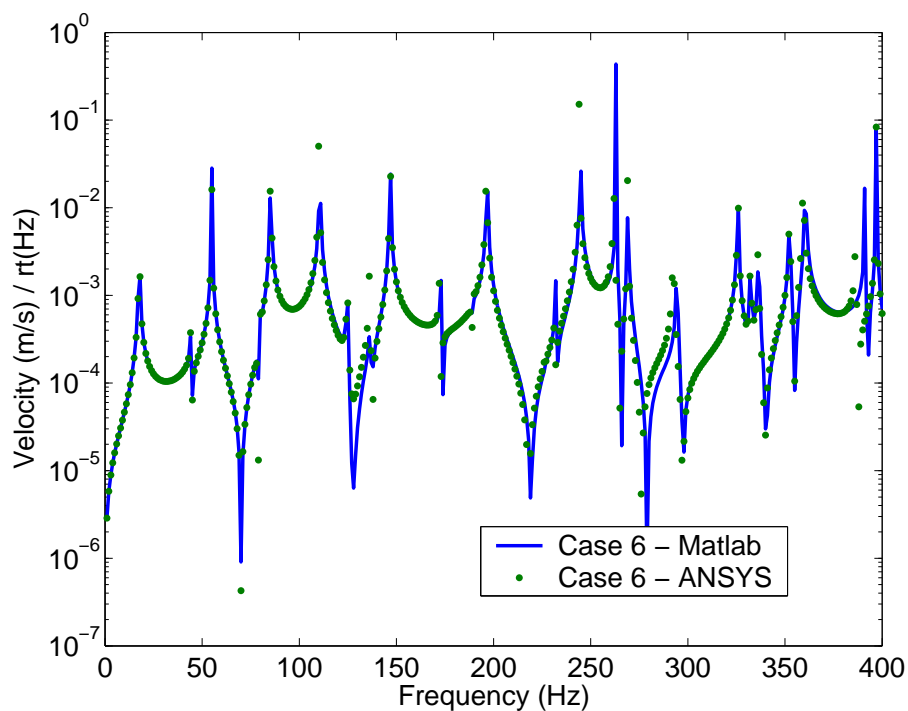


FIG. D.6: Velocity of the plate at node 1000 for the MATLAB and ANSYS models for Case 6, where a TMD is attached that has a resonance frequency of 209Hz, and only modes up to 1600Hz were included in the modal analysis.

Figure D.7 shows a picture of the ANSYS model, showing the locations of the applied force by the red arrow, and the two TMDs.

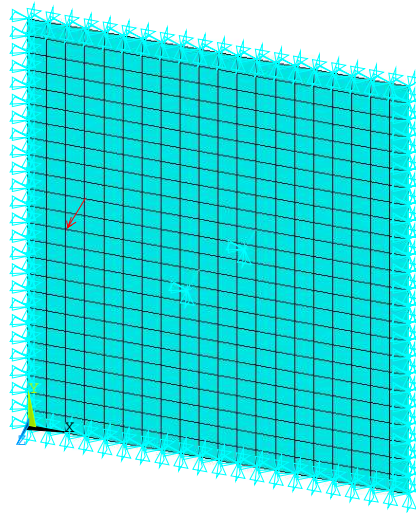


FIG. D.7: ANSYS model for Case 7.

Figures D.8 to D.10 show the velocity response at nodes 808, 880, and 1000, respectively. Nodes 808 and 880 are at the attachment points of the TMDs, and node 1000 is a randomly chosen location. The results show that there is good agreement between both methods of modelling.

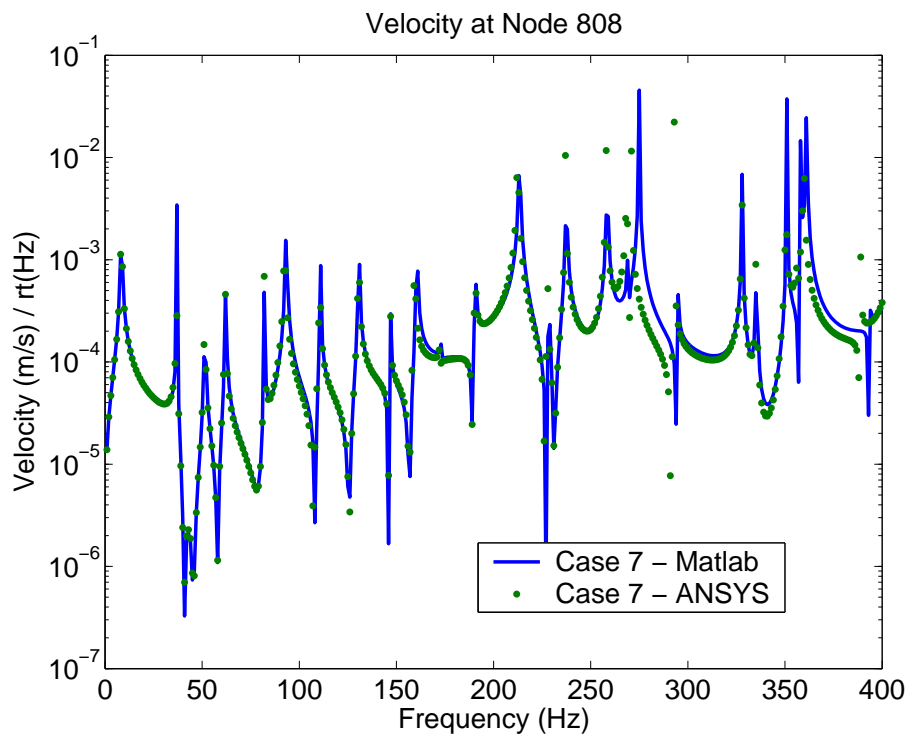


FIG. D.8: Velocity of the plate at node 808 for the MATLAB and ANSYS models for Case 7.

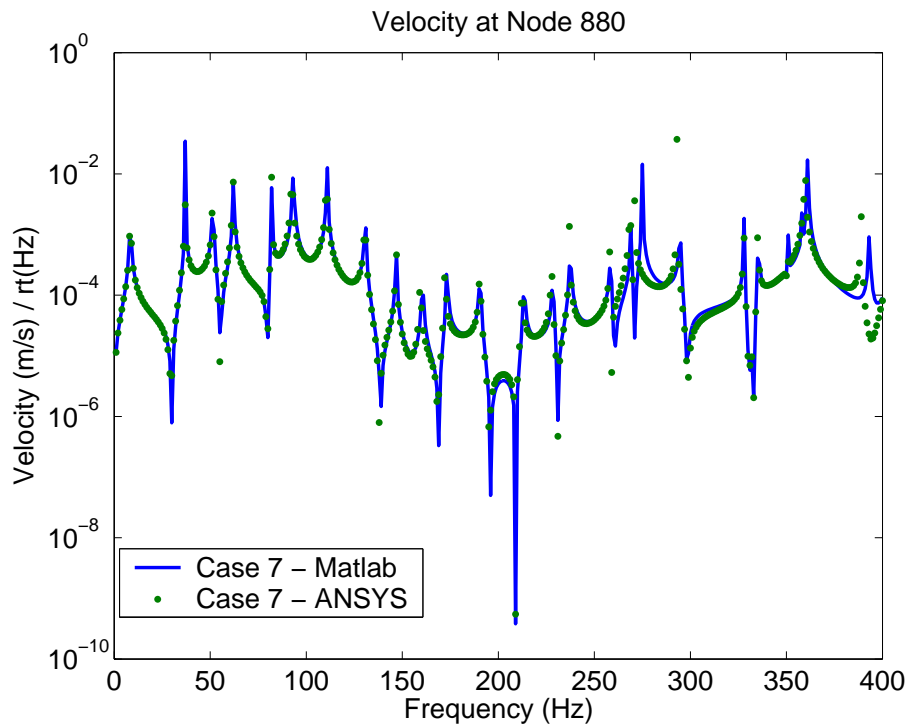


FIG. D.9: Velocity of the plate at node 880 for the MATLAB and ANSYS models for Case 7.

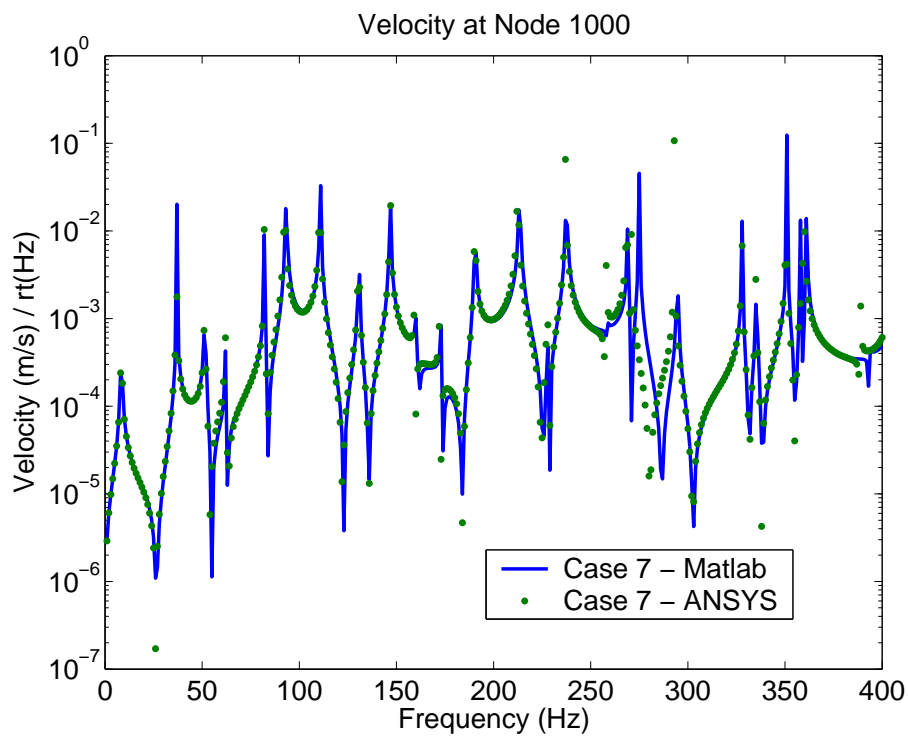


FIG. D.10: Velocity of the plate at node 1000 for the MATLAB and ANSYS models for Case 7.

The results presented in this section demonstrate that the modal coupling software implemented in MATLAB can correctly predict the sound pressure levels and velocity of the structure when tuned mass dampers are attached to the structure and when Helmholtz resonators are attached to the cavity.

D.3 Helmholtz Resonators

This section describes comparisons that are made between the mathematical model of a Helmholtz resonator attached to a large cavity developed in section 3.3 and equivalent ANSYS models, to ensure that the Matlab modal coupling software can correctly predict the sound pressure level inside a large cavity.

D.3.1 Application of the acoustic load to the fluid

The first stage is to develop methods in ANSYS to apply a volume velocity to a model of a large acoustic cavity. An equivalent mathematical model that uses modal summation (which is used in the modal coupling method used in this work) was developed and compared with the predictions made using ANSYS. Two methods are developed in ANSYS to model the application of a volume velocity source to a large cavity. The first involves using elements that are capable of coupling a fluid and structure - Fluid-Structure Interaction (FSI) elements. The second method involves applying a volume acceleration source boundary condition to a node, called a FLOW condition in ANSYS, which is the time derivative of a volume velocity source, a familiar term to acousticians. Comparisons are made between these three methods: the Matlab modal coupling software, a FLOW boundary condition in ANSYS, and using 4 Fluid-Structure Interaction (FSI) elements in ANSYS.

The previous two reports [3, 5] demonstrated that the modal coupling method can be used successfully to predict the sound pressure level inside the cavity at a couple of remote locations. The work conducted during the present stage was a thorough set of tests to check that the methods used can accurately predict the response of the system. The results presented here show that the prediction of the SPL at, and close to the drive point is poor due to an insufficient number of modes being used in the analysis. However, the sum of squared pressures at all nodes, which is proportional to the acoustic potential energy of the cavity, is the same for all methods examined. Hence, one must consider what is the appropriate cost function to be minimised. If the SPL in a localised region is the cost function to be minimised, then care must be taken to include a sufficient number of modes in the analysis.

A rectangular acoustic cavity with rigid walls was modelled in ANSYS, as shown in Figure D.11. The dimensions of the box are $0.3\text{m} \times 0.2\text{m} \times 0.4\text{m}$, and air was used as the acoustic fluid. In this section we are only concerned with methods to generate a sound pressure level inside the cavity and will not discuss Helmholtz resonators. In later sections we will investigate the effects of attaching Helmholtz resonators to the cavity.

Three types of analyses were conducted on the model:

Matlab Modal Coupling This method involved using the ANSYS and Matlab code developed in Stages 1 and 2 of this project [3, 5]. ANSYS is used to conduct modal analyses of the acoustic cavity with rigid walls and in-vacuo structure, and the Matlab code reads in the ANSYS modal analysis results and calculates the pressure within the cavity. Actually, the software calculates the modal participation factors for pressure and vibration, which can be used with the mode shape vectors calculated in ANSYS to calculate the pressure at any location within the cavity.

Flow boundary condition An acoustic analysis in ANSYS can have a forcing function

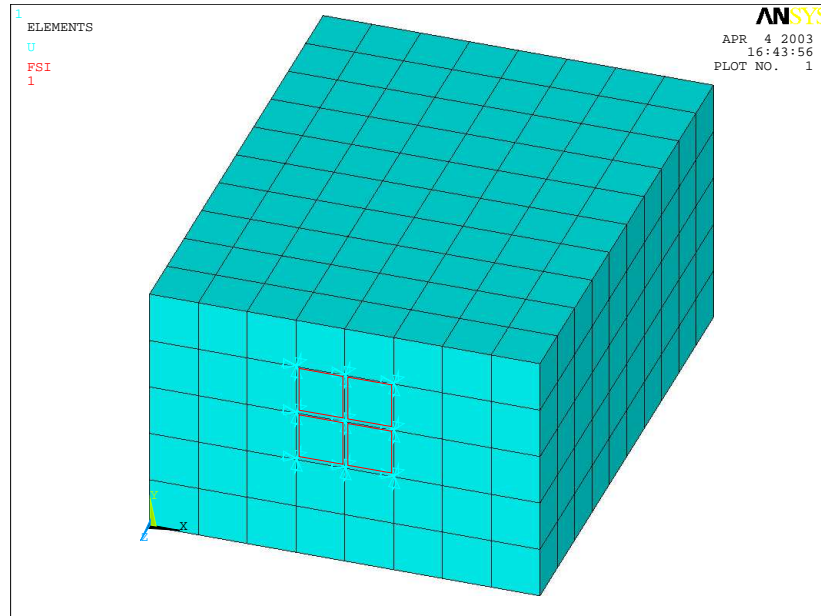


FIG. D.11: ANSYS model of the small box, showing the 4 FSI elements on the $z = 0$ face.

applied to the fluid. Typically one applies a volume velocity or a pressure source within the fluid, and the pressure response is calculated at another location within the cavity. In ANSYS, one can apply a ‘FLOW’ forcing function to the model which is described as [8, page 3.4],

“FLOW fluid loads are normally applied to nodes that are on the fluid mesh boundary. A FLOW fluid load is equal to the negative of the fluid particle acceleration normal to the mesh boundary (+ outward), times an effective surface area associated with the node, times the mean fluid density.”

Hence the FLOW boundary condition in ANSYS is a volume acceleration, rather than a volume velocity. The case that was analysed was to apply a FLOW loading on a node.

Fluid-Structure Interaction Elements The intended method for modelling a Helmholtz resonator is to place four fluid-structure interaction (FSI) elements within the model, and fix the displacement degrees of freedom on all the circumferential nodes, and apply a harmonic displacement to the central node.

Note that for the last method, using 4 FSI elements, a volume displacement is applied to the cavity, rather than a volume velocity, or volume acceleration. Hence two of the three methods need to be converted so that the results can be compared.

The analyses compare the pressures at three locations: 1. at the driving point; 2. directly in front of the driving point; and 3. at a remote location. The locations and node numbers are listed in Table D.3.

Description	Node	X	Y	Z
Driving point	95	0.15	0.12	0.0
In front of driving point	477	0.15	0.12	-0.04
Remote location	488	0.1875	0.04	-0.32

Table D.3: Locations of the nodes.

Figures D.12 to D.14 show the predicted pressure at the driving point, in front of the driving point, and at a remote location, respectively. Figure D.12 shows that the frequency at which the pressure is a minimum is different for the 3 methods, which is slightly disturbing. One wants the three methods to be equivalent. Figure D.13 shows that directly in front of the driving point, the results are different for the three methods. However, Figure D.14 shows that at a location remote from the driving point, the predicted pressures are the same for all three methods.

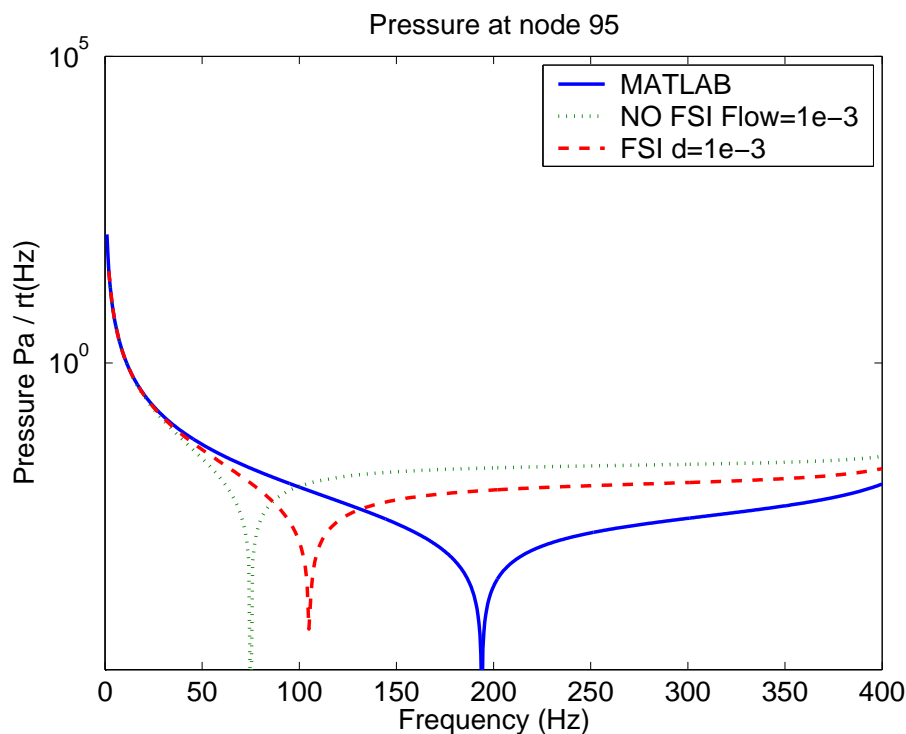


FIG. D.12: Pressure at the driving point for the three methods.

The results shown in Figure D.12 were examined in more detail to determine if there were fundamental problems with the mathematics for the modal coupling, or if the ANSYS model poorly captured the physics of the problem. An additional model was created of a rectangular box using a theoretical model presented in Ref [7, page 151].

Figure D.15 shows that the pressure at the driving point varies depending on the number of modes included in the analysis. Inclusion of more than 8000 modes does not provide significant changes in the response, however this is an impractical number of modes to include in the general analysis of the problem at hand. This theoretical model can be compared with the previous results shown in Figures D.12 to D.14.

Figures D.16 and D.17 show the predicted response for the theoretical model for the

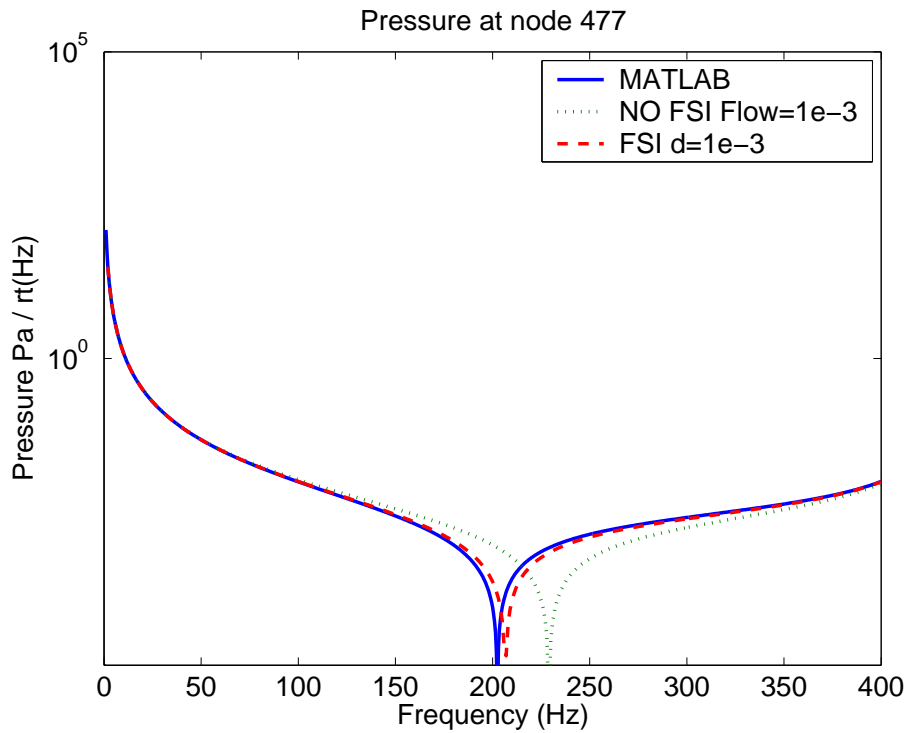


FIG. D.13: Pressure at the node directly in front of the driving point for the three methods.

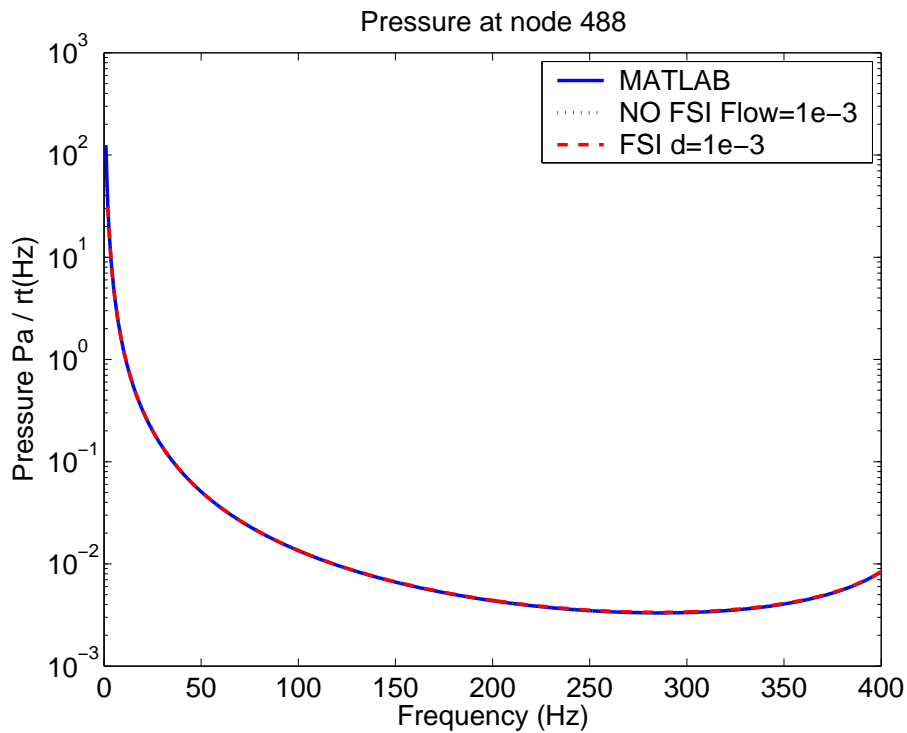


FIG. D.14: Pressure at a remote location for the three methods.

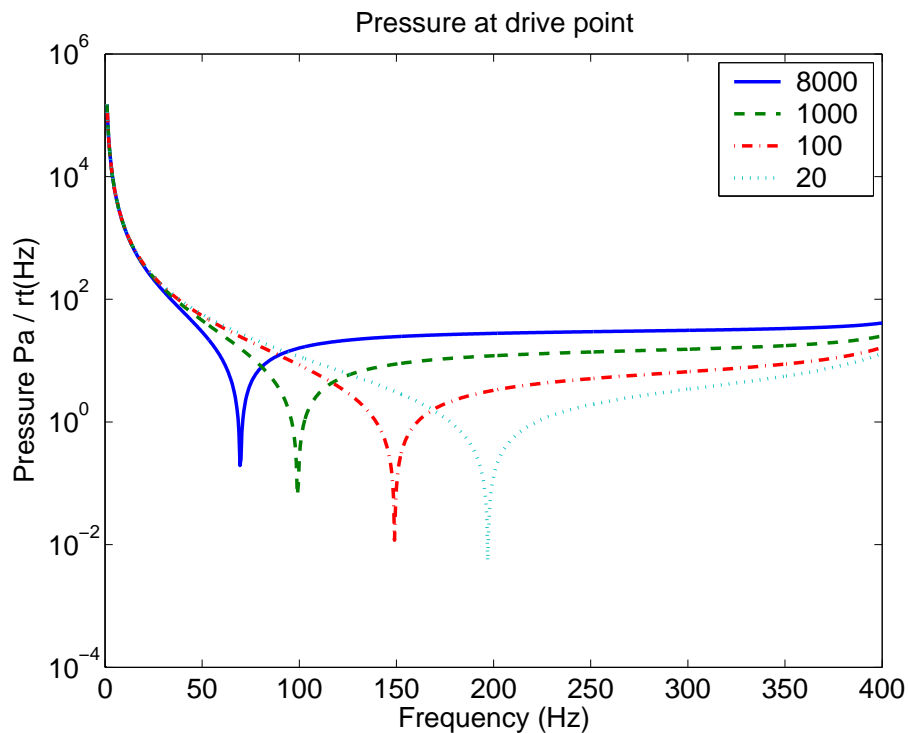


FIG. D.15: Pressure at the driving point for the theoretical model, for varying number of modes included in the analysis.

location directly in front of the driving point and at a remote location, respectively. Figure D.16 shows that the response at the driving point varies depending on the number of modes included in the analysis, whereas Figure D.17 shows that the results at a remote location are independent of the number of modes included in the analysis.

Figure D.18 shows that inclusion of 8000 modes in the theoretical model has a response that is close to the response predicted using the FLOW=1 boundary condition applied to a node in the ANSYS model.

Figure D.19 shows that inclusion of 700 modes in the theoretical model has a response that is close to the response predicted using the ANSYS model with the 4 FSI elements and driving the central node.

Figure D.20 shows that inclusion of 20 modes in the theoretical model has a response that is close to the response predicted using the ANSYS model with the modal coupling theory.

The reason that a different number of modes are required in the theoretical analysis to produce results that correspond to each of the three different analysis methods is related to the wavelength of the modes included in the analysis.

For the case where the FLOW boundary condition is applied to a node, this is equivalent to a point source in the model, where the power is emitted from a single point. To omit modes from the model, and hence omit these energy transport mechanisms at this location causes inaccuracies in the prediction.

It was found that when 700 modes were used in the theoretical model the results matched the ANSYS predictions using the four FSI elements. The maximum modal indices for 700 modes are 10, 7, 14 along the x,y,z directions, respectively. Hence the ratio

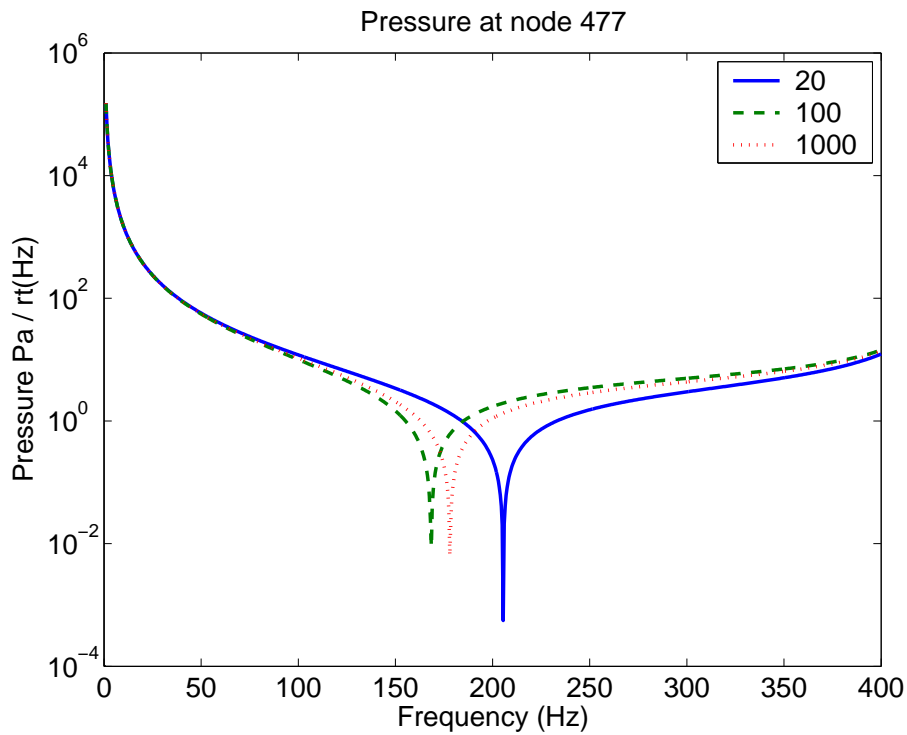


FIG. D.16: Pressure in front of the driving point for the theoretical model, for varying number of modes included in the analysis.

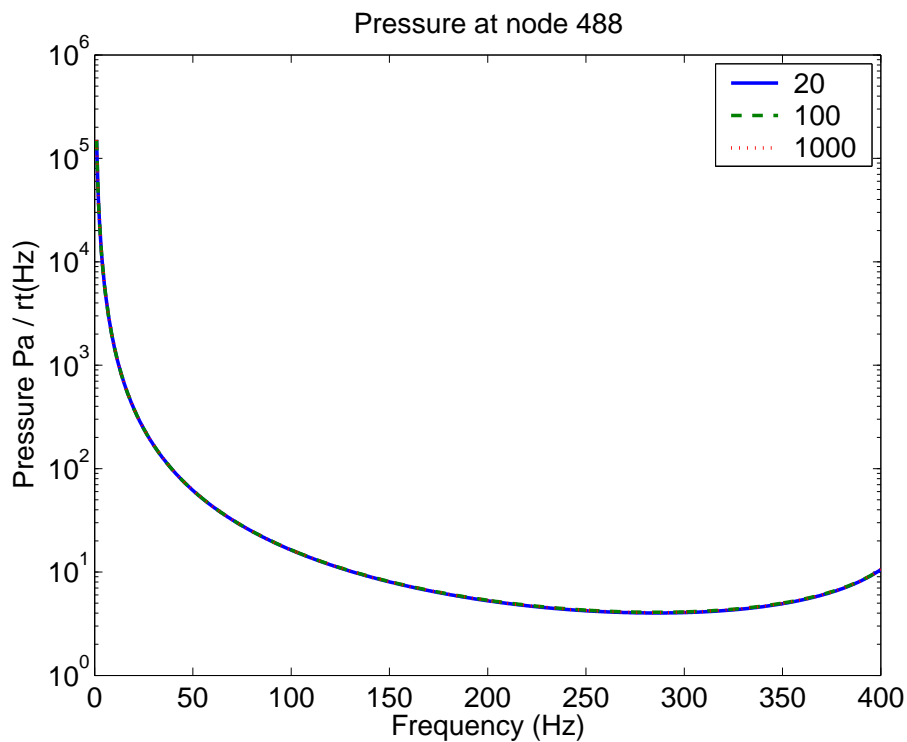


FIG. D.17: Pressure at a remote location for the theoretical model, for varying number of modes included in the analysis.

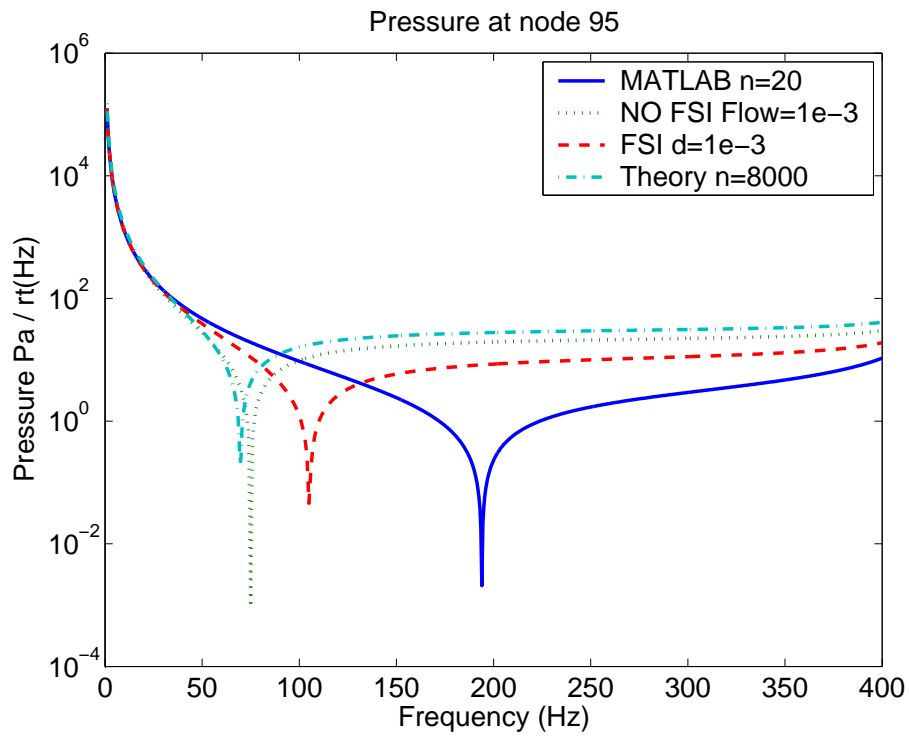


FIG. D.18: Pressure at the driving point for 8000 modes in the theoretical model, and for the 3 previous methods.

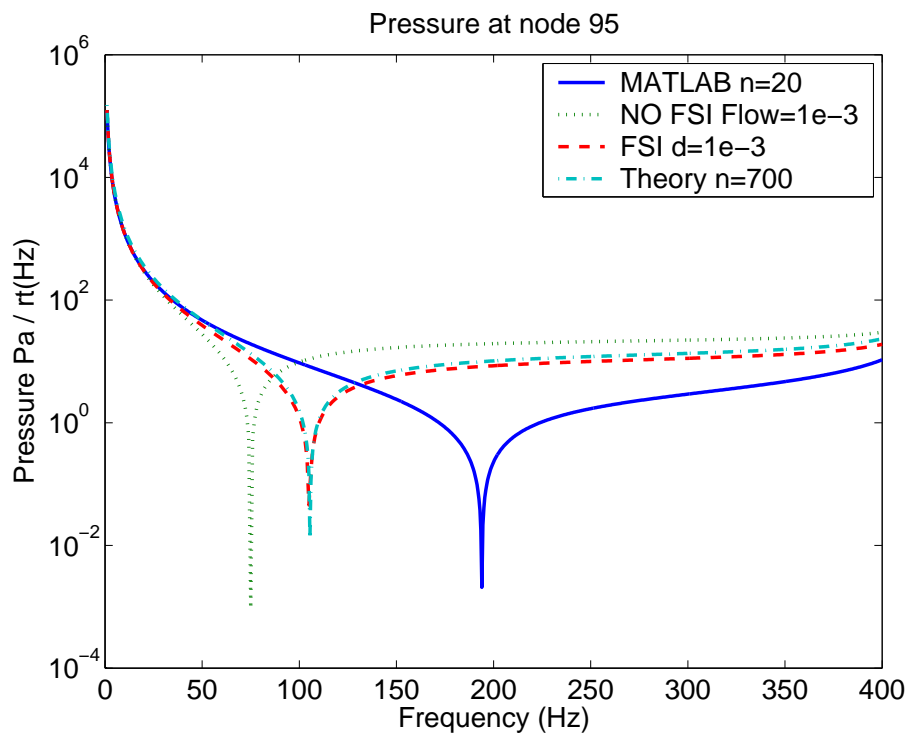


FIG. D.19: Pressure at the driving point for 1000 modes in the theoretical model, and for the 3 previous methods.

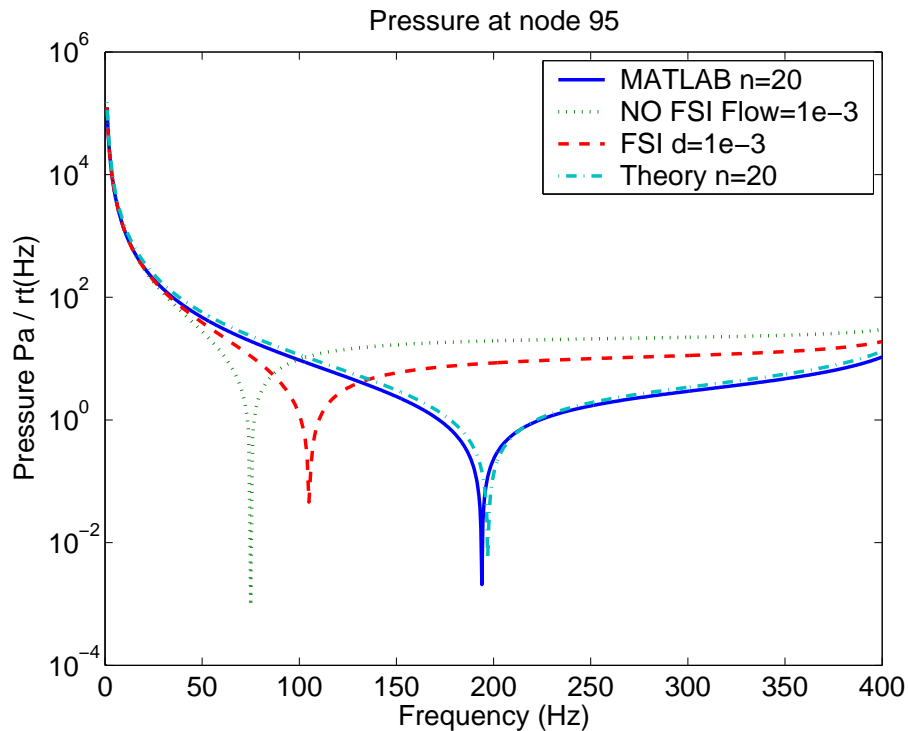


FIG. D.20: Pressure at the driving point for 20 modes in the theoretical model, and for the 3 previous methods.

between the modal indices and the size of the maximum dimension in the corresponding direction yields: 0.03m, 0.029m, 0.029m. The element size in the x,y,z direction at node 95 is 0.0375, 0.04, 0.04. This means the modes have a wavelength that is slightly smaller than the effective radiating area of the node.

It was found that when 20 modes were used in the theoretical model the results matched the ANSYS predictions using the modal coupling theory. This is not at all surprising, because only 20 modes were included in the modal coupling theory analysis.

These analyses have shown that in fact all of the prediction methods used were accurate, and the results varied because of the differences in the various loading conditions.

The next part is to compare the acoustic potential energy transmitted into the cavity for the various loading conditions. The acoustic potential energy is proportional to the sum of the squared pressure at each node in the model. Figure D.21 shows that the calculated sum of squared pressures for the three methods are the same.

It has been shown that it is important to consider the number of modes required to get accurate results, depending on where the pressure is evaluated.

D.3.2 Single Helmholtz resonator

A large rectangular acoustic cavity with dimensions $(x, y, z) = (0.6, 0.75, 0.8)$ m was modelled in ANSYS. The element spacing was 0.04m, which means that acoustic predictions can be made up to 1400Hz. It would have been preferable to obtain a modal analysis of the cavity up to 2000Hz, however the Department's ANSYS license has a limit of 32,000 nodes, which limits the size of models that can be constructed.

Assuming that a cubic volume is modelled in ANSYS, if one wants to obtain results up

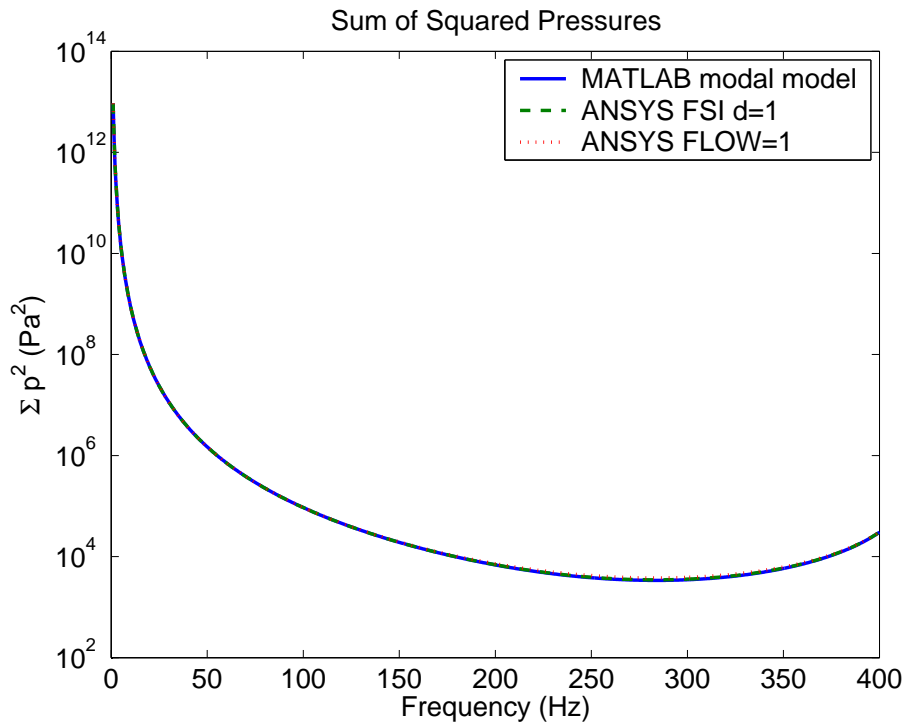


FIG. D.21: Sum of the squared pressures for the three methods.

to 400Hz, then using the guide that modes up to two octaves higher need to be included in the analysis, the modal analysis should be conducted up to 1600Hz. A general rule for acoustic finite element analyses is that one should use an absolute minimum of 6 elements per wavelength (generally 8-12 for accurate results). The element size should be no larger than

$$\frac{c}{f_{\max} \times 6} = \frac{344 \text{ (m/s)}}{1600 \text{ (Hz)} \times 6 \text{ (elem}/\lambda)} = 0.0358\text{m} \quad (\text{D.1})$$

The number of nodes n in a volume is proportional to the cube of the linear dimensions, hence one can write an expression

$$32000 > n^3 = \left(\text{int} \left(\frac{L}{0.03583} \right) + 1 \right)^3 \quad (\text{D.2})$$

Solving this inequality, $L < 1.075\text{m}$, and hence the volume must be less than $V = L^3 = 1.24\text{m}^3$, which is smaller than the volume inside the payload bay of a rocket. Hence, it is necessary to use a version of ANSYS than is unrestricted in the number of nodes, or a different finite element analysis software package if accurate results are to be obtained up to 400Hz.

Figure D.22 shows the pressure response at node 1044, the location where the Helmholtz resonator was attached. The resonator was tuned to a frequency of 215Hz by using a spring with stiffness $k = 18248.9\text{N/m}$ and a mass of $m = 0.01\text{kg}$. Figure D.23 shows the same data viewed over a narrow frequency range, and the results show that the pressure decreases at the resonance frequency of the Helmholtz resonator. Note that the results for the Helmholtz resonator were calculated in Matlab using a frequency spacing of 0.5Hz, and the ANSYS results were calculated using a frequency spacing of 1Hz. Figures D.24 and

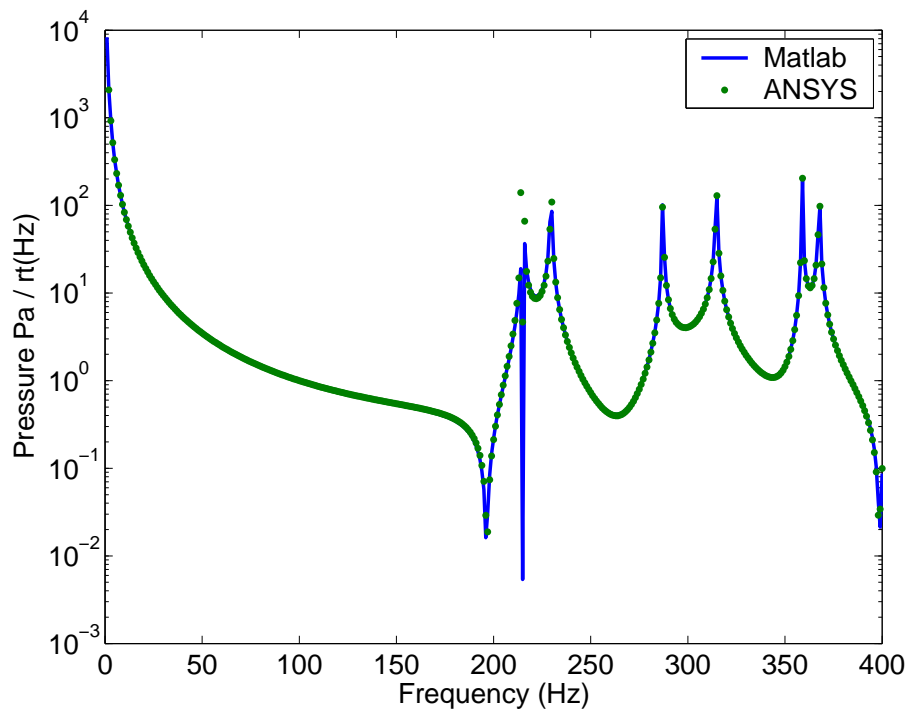


FIG. D.22: Pressure at node 1044, when one Helmholtz resonator was attached to the cavity.

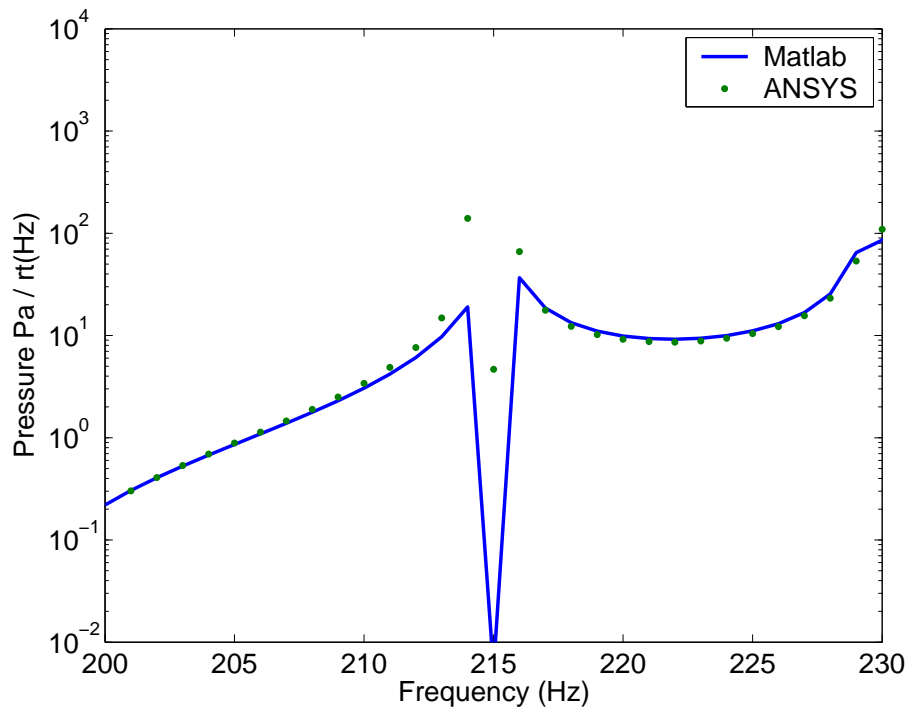


FIG. D.23: Pressure at node 1044, when one Helmholtz resonator was attached to the cavity, viewed over a narrow frequency range.

D.25 show the pressure response at node 5414, which was selected as a random location (0.4400, 0.15789, -0.60000), and shows that the response is predicted correctly.

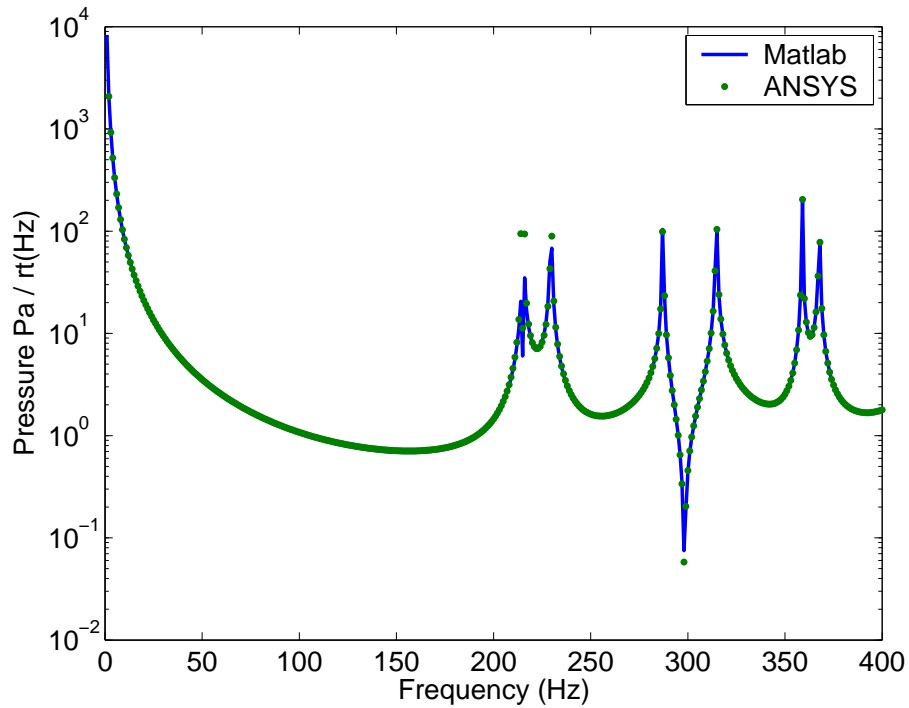


FIG. D.24: Pressure at node 5414, when one Helmholtz resonator was attached to the cavity.

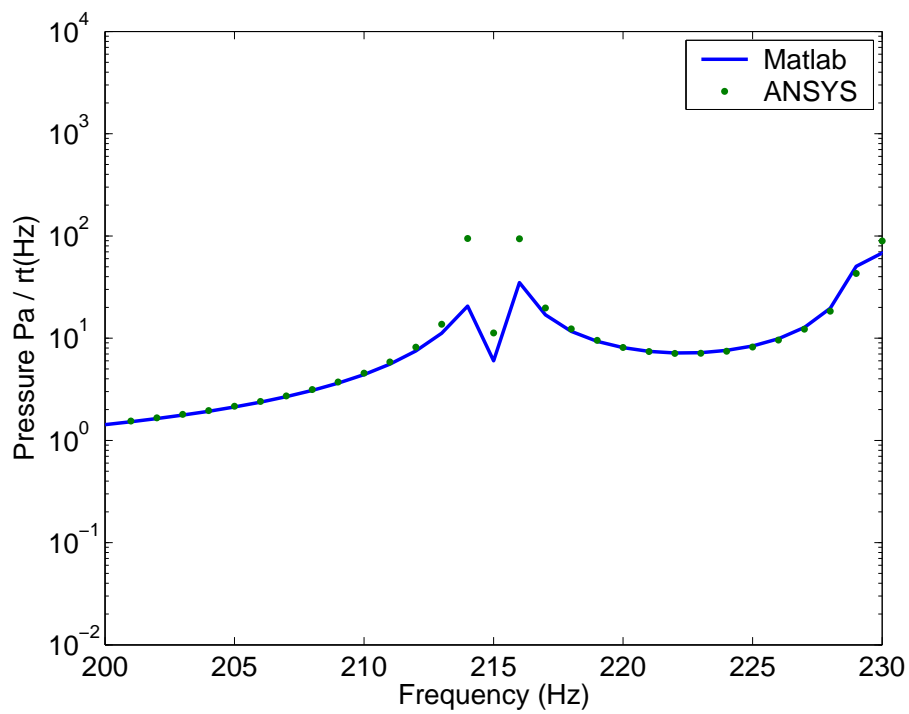


FIG. D.25: Pressure at node 5414, when one Helmholtz resonator was attached to the cavity, viewed over a narrow frequency range.

D.3.3 Two Helmholtz resonators

The parameters used for two Helmholtz resonators attached to nodes 1044 (as above) and 1667 are shown in Table D.4.

Helmholtz Resonator	1	2
Node	1044	1667
Stiffness	18248.9 N/m	10381.6 N/m
Mass	0.01 kg	0.005 kg
Frequency	215 Hz	229.3 Hz
Loc X	0.16	0.75
Loc Y	0.6	0.19737
Loc Z	-0.2	-0.2

Table D.4: Parameters for the model of the cavity with two Helmholtz resonators attached to it.

Figure D.26 shows the ANSYS model of the cavity with two Helmholtz resonators attached to it.

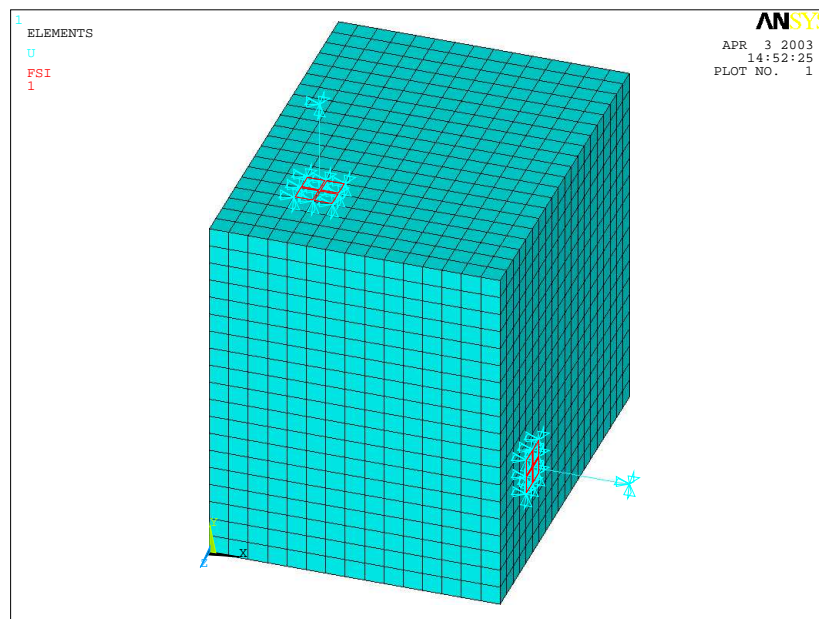


FIG. D.26: ANSYS model of a cavity with two Helmholtz resonators attached to it.

Figures D.27 to D.32 show the pressure at the node that connects the large acoustic cavity to Helmholtz resonators 1 and 2, and at a random node inside the large cavity. The results show that Matlab modal coupling software and the ANSYS predictions are the same.

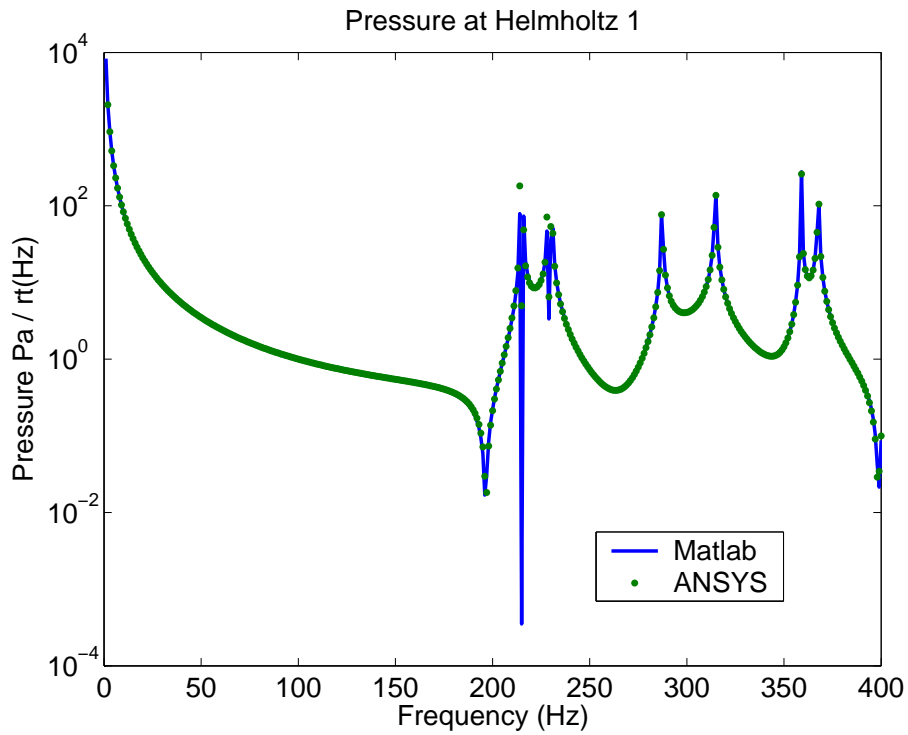


FIG. D.27: Pressure at node 1044 with two Helmholtz resonators attached.

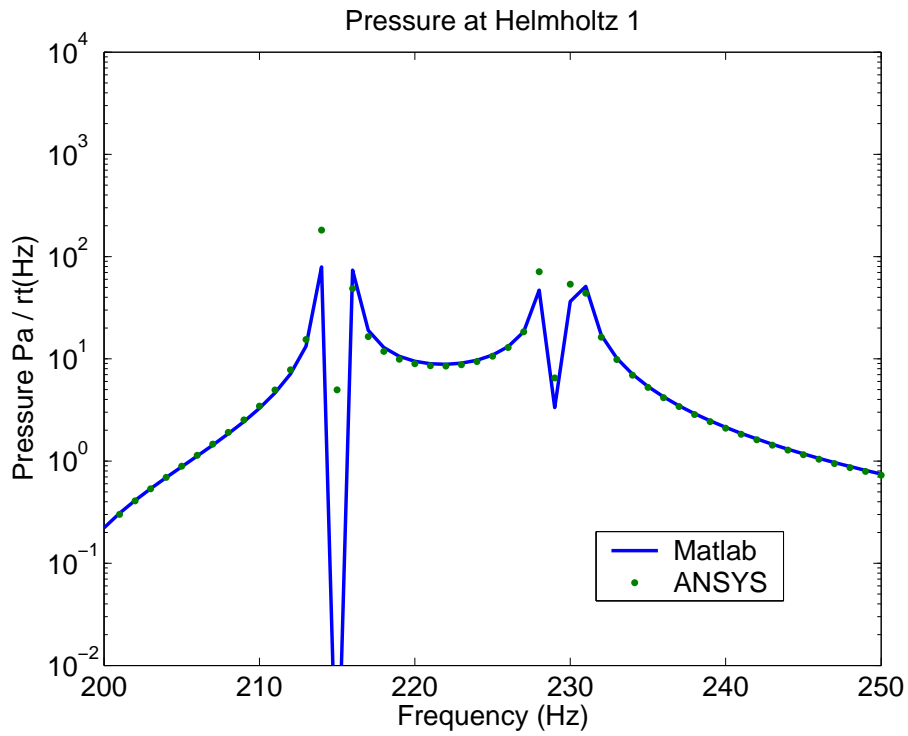


FIG. D.28: Pressure at node 1044 with two Helmholtz resonators attached.

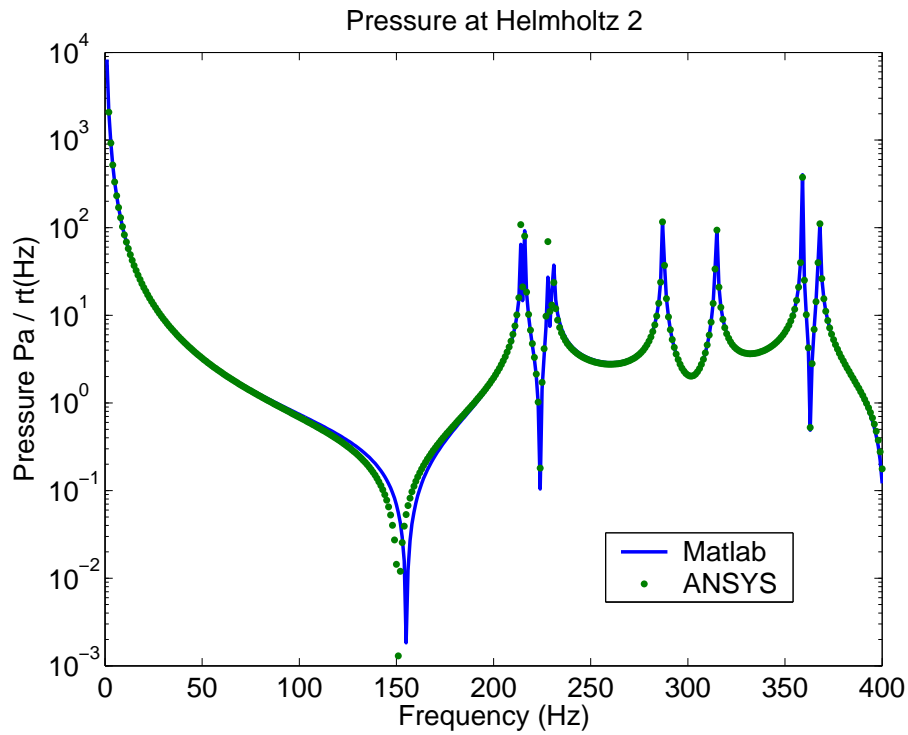


FIG. D.29: Pressure at node 1667 with two Helmholtz resonators attached.

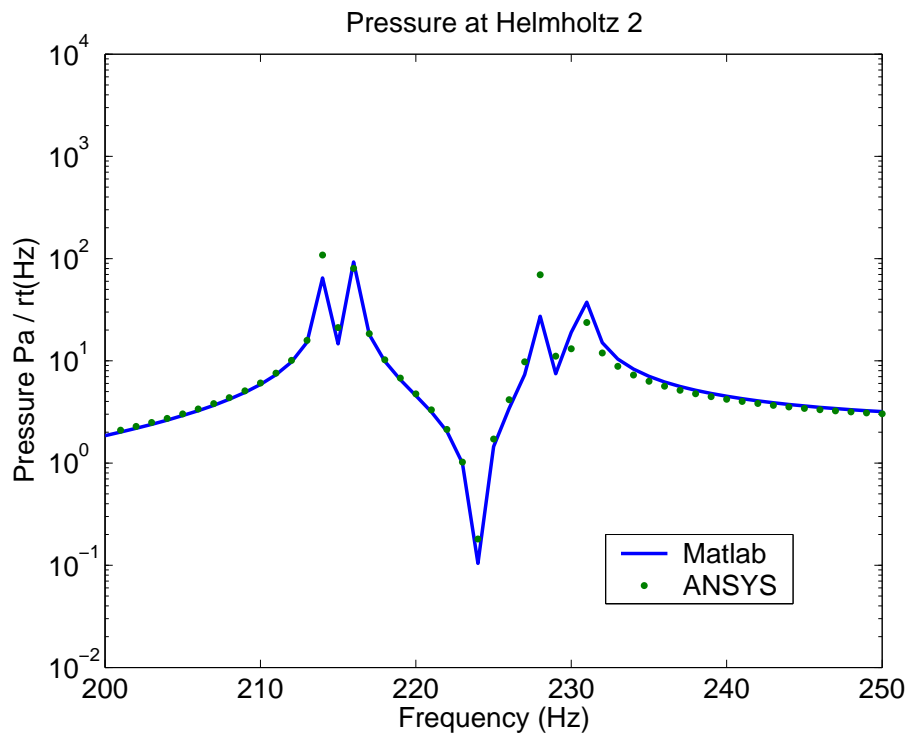


FIG. D.30: Pressure at node 1667 with two Helmholtz resonators attached.

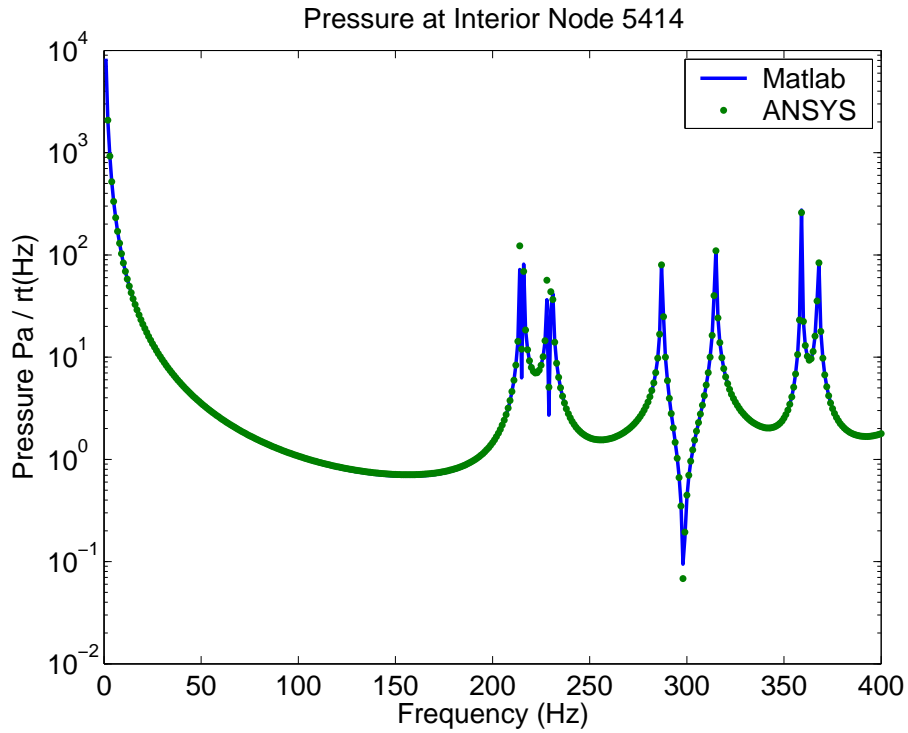


FIG. D.31: Pressure at random node 5414 with two Helmholtz resonators attached.

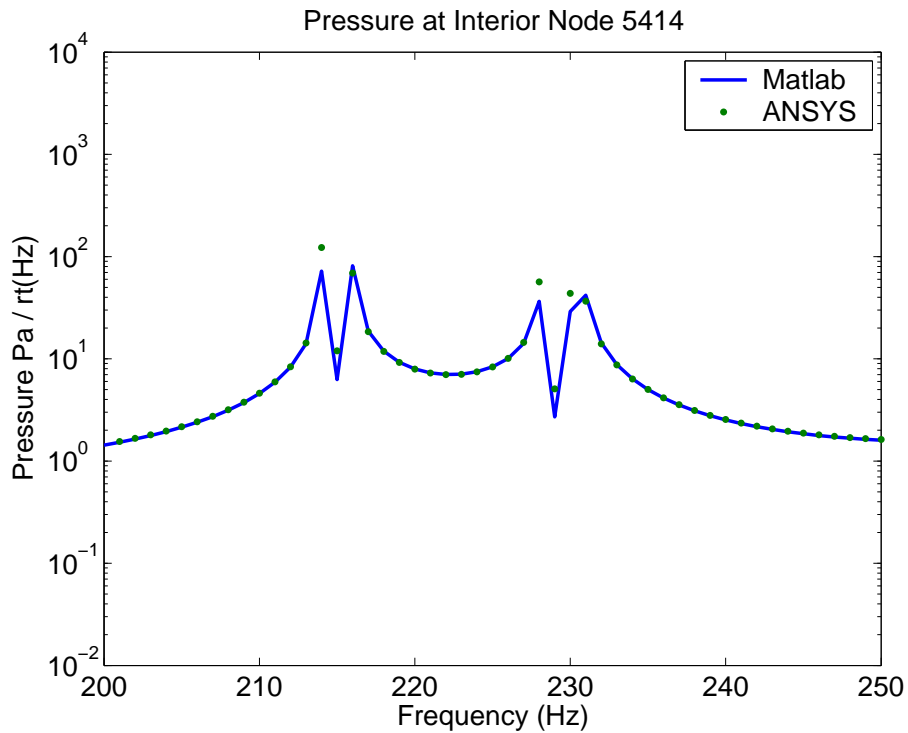


FIG. D.32: Pressure at a random node 5414 with two Helmholtz resonators attached.

D.3.4 Multiple Helmholtz resonators

The parameters used in for the three Helmholtz resonators attached to the cavity are shown in Table D.5, and the ANSYS model is shown in Figure D.33.

Helmholtz	1	2	3
Node	1044	1667	447
Stiffness	18248.9 N/m	10381.6 N/m	16221.243 N/m
Mass	0.01 kg	0.005 kg	0.005 kg
Frequency	215 Hz	229.3 Hz	286.6 Hz
Loc X	0.16	0.75	0.16
Loc Y	0.6	0.19737	0.19737
Loc Z	-0.2	-0.2	0

Table D.5: Parameters for the model of the cavity with three Helmholtz resonators attached to it.

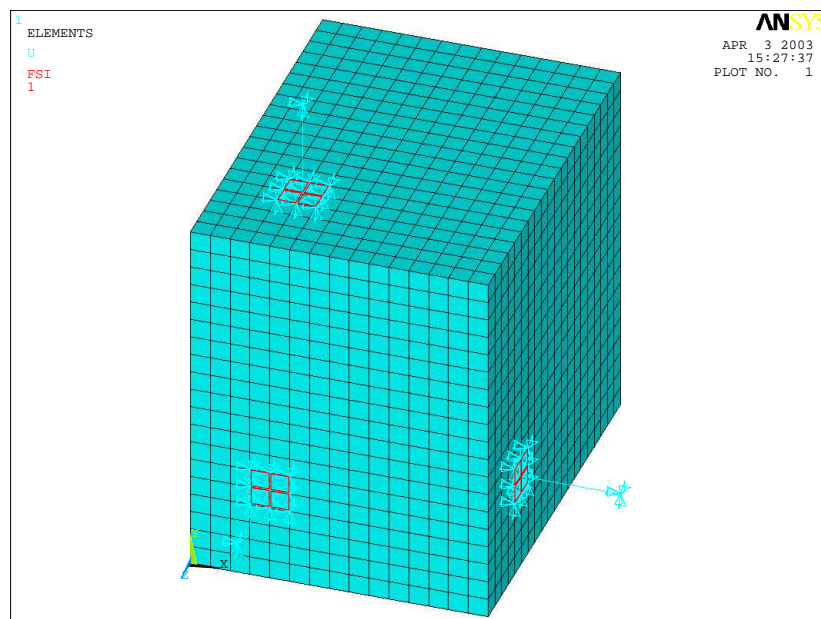


FIG. D.33: ANSYS model of a cavity with three Helmholtz resonators attached to it.

Figures D.34 to D.41 show the pressure at the node that connects the large acoustic cavity to Helmholtz resonators 1, 2, and 3, and at a random node inside the large cavity. The results show that Matlab modal coupling software and the ANSYS predictions are the same.

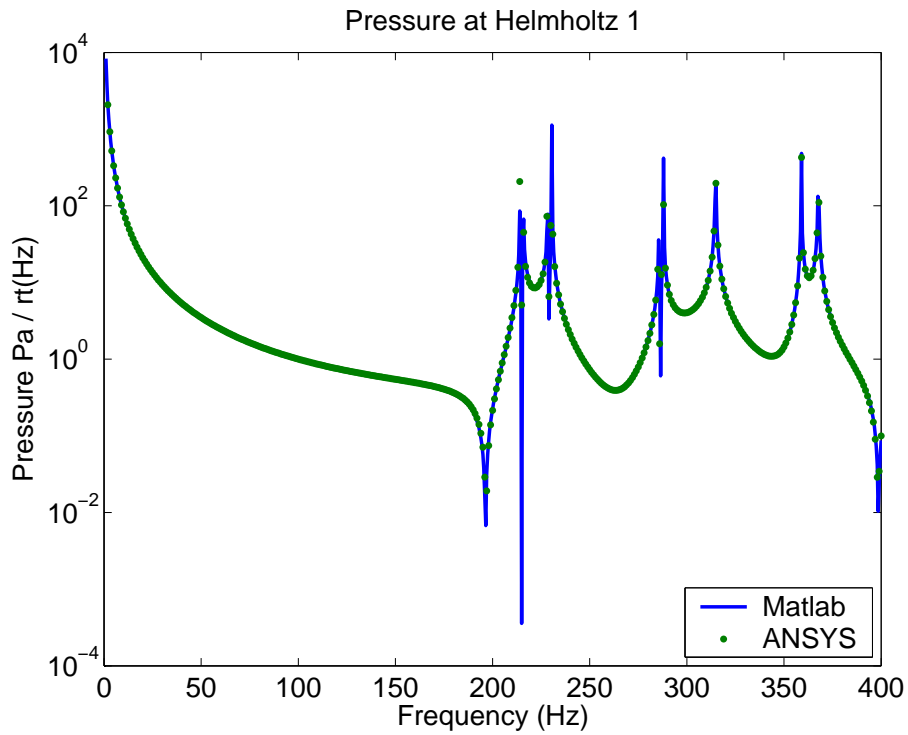


FIG. D.34: Pressure at node 1044 with three Helmholtz resonators attached.

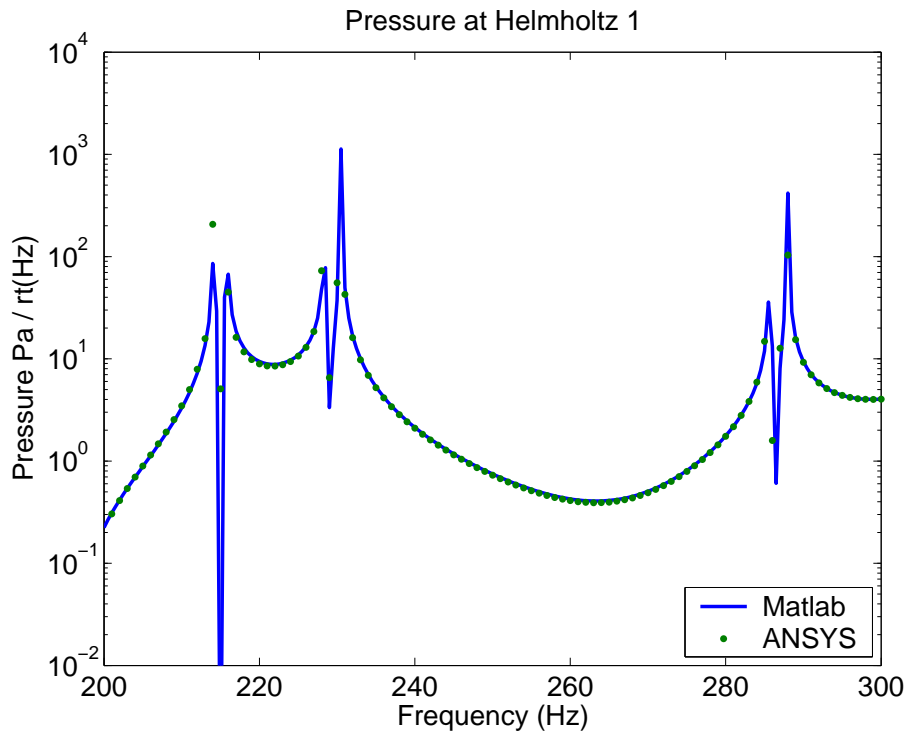


FIG. D.35: Pressure at node 1044 with three Helmholtz resonators attached.

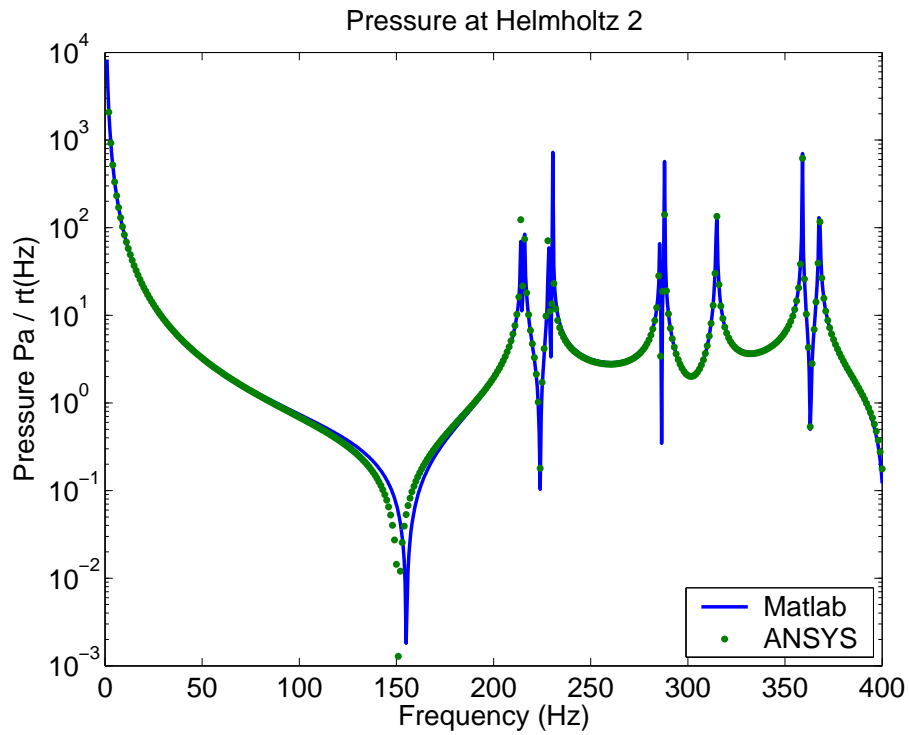


FIG. D.36: Pressure at node 1667 with three Helmholtz resonators attached.

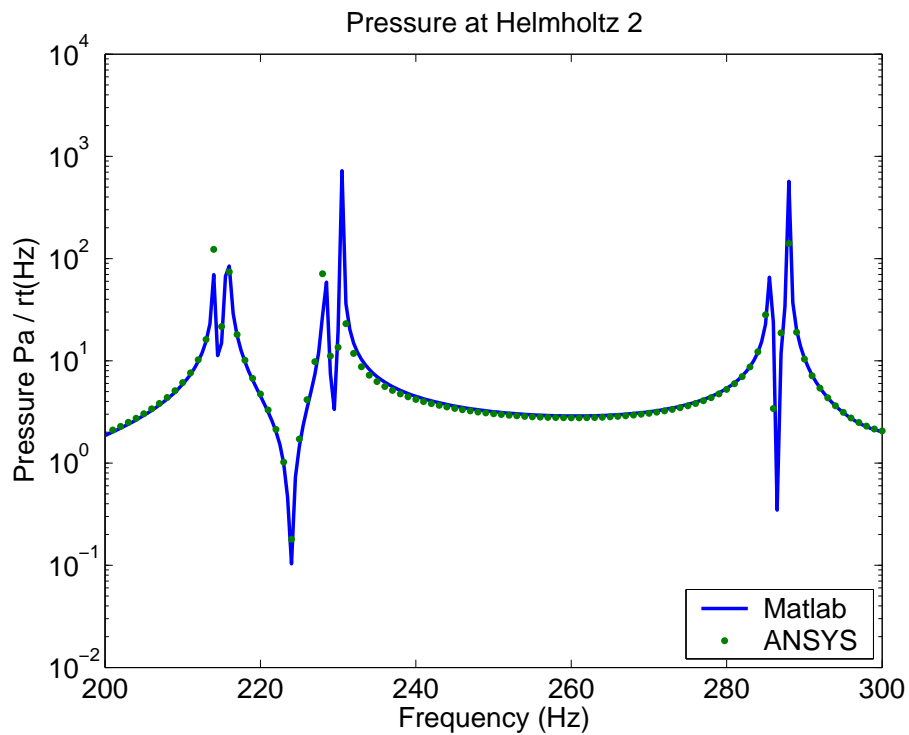


FIG. D.37: Pressure at node 1667 with three Helmholtz resonators attached.

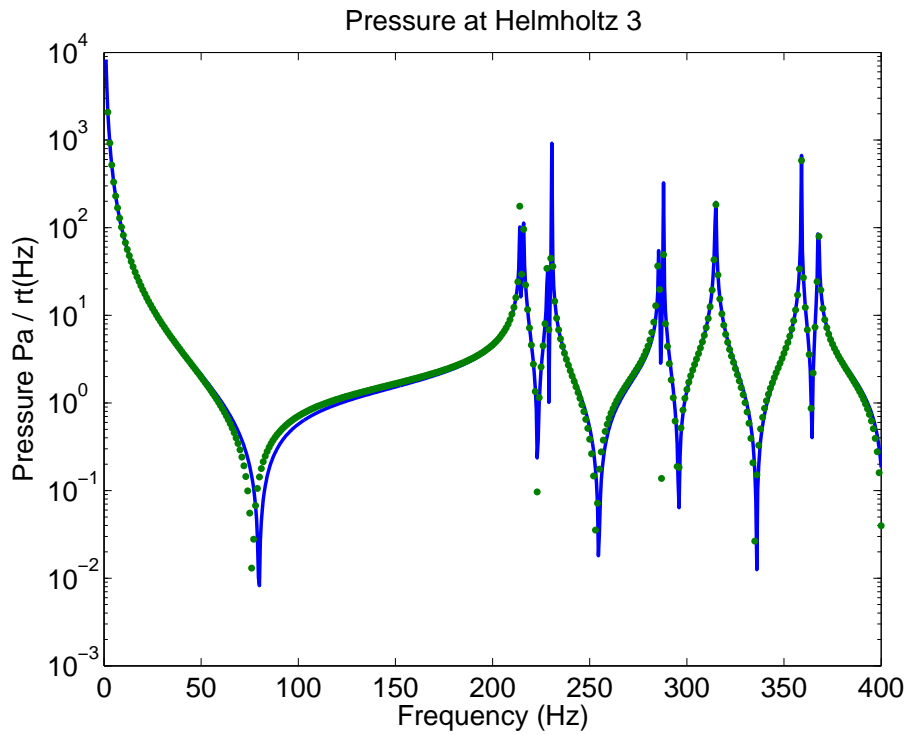


FIG. D.38: Pressure at node 447 with three Helmholtz resonators attached.

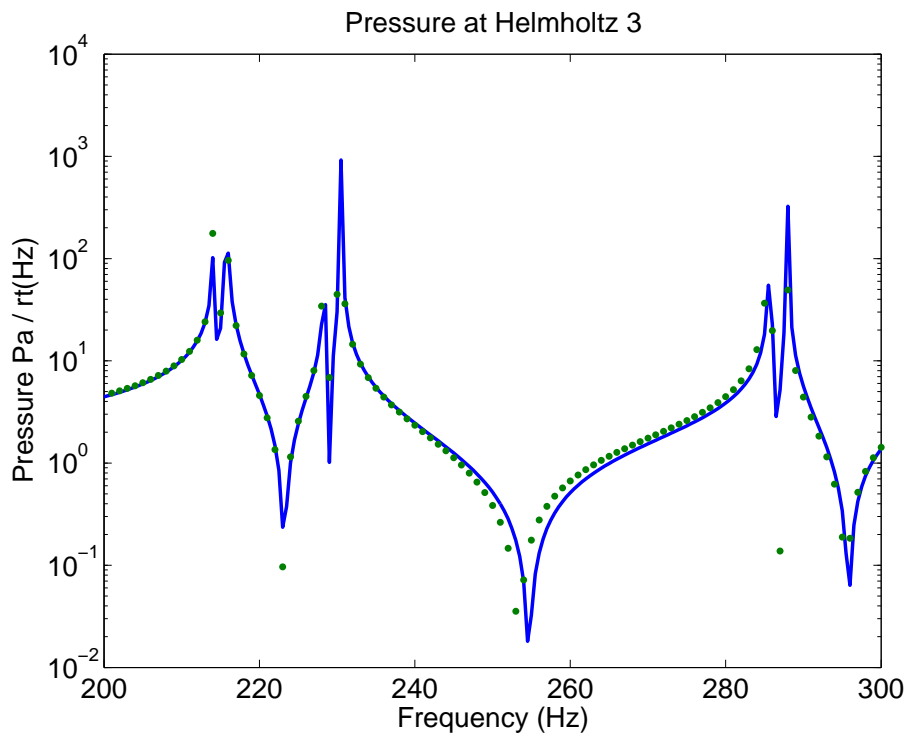


FIG. D.39: Pressure at node 447 with three Helmholtz resonators attached.

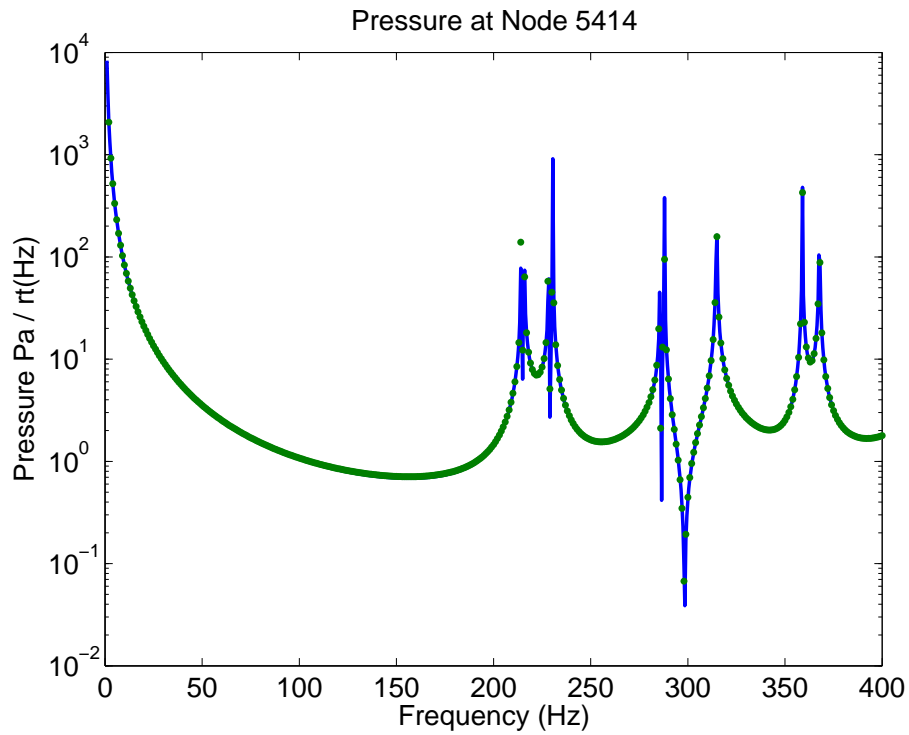


FIG. D.40: Pressure at a random node 5414 with three Helmholtz resonators attached.

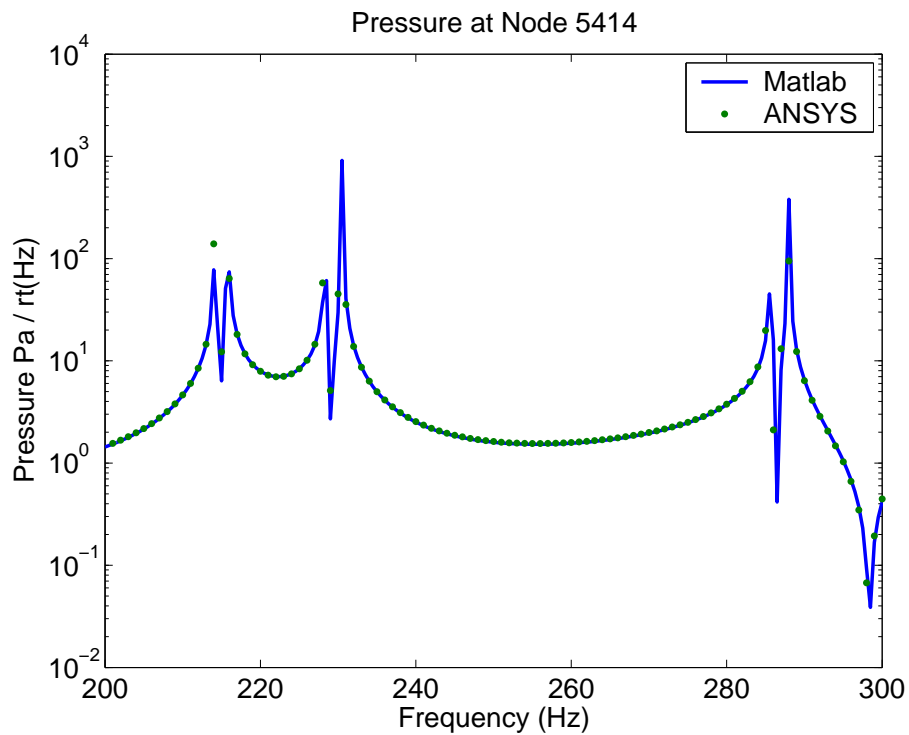


FIG. D.41: Pressure at a random node 5414 with three Helmholtz resonators attached.

As described previously, the Helmholtz resonator is modelled as a mass attached to an extensional spring. In ANSYS the mass is connected the central node of 4 FSI elements that connect displacement degrees of freedom to acoustic pressure degrees of freedom. The spring element in ANSYS can stretch and hence the node at the centre of the 4 FSI elements will move in unison with the mass. Figures D.42 to D.44 show the comparison between the displacement at the central node, predicted using the modal coupling theory and predicted using the ANSYS have the same results.

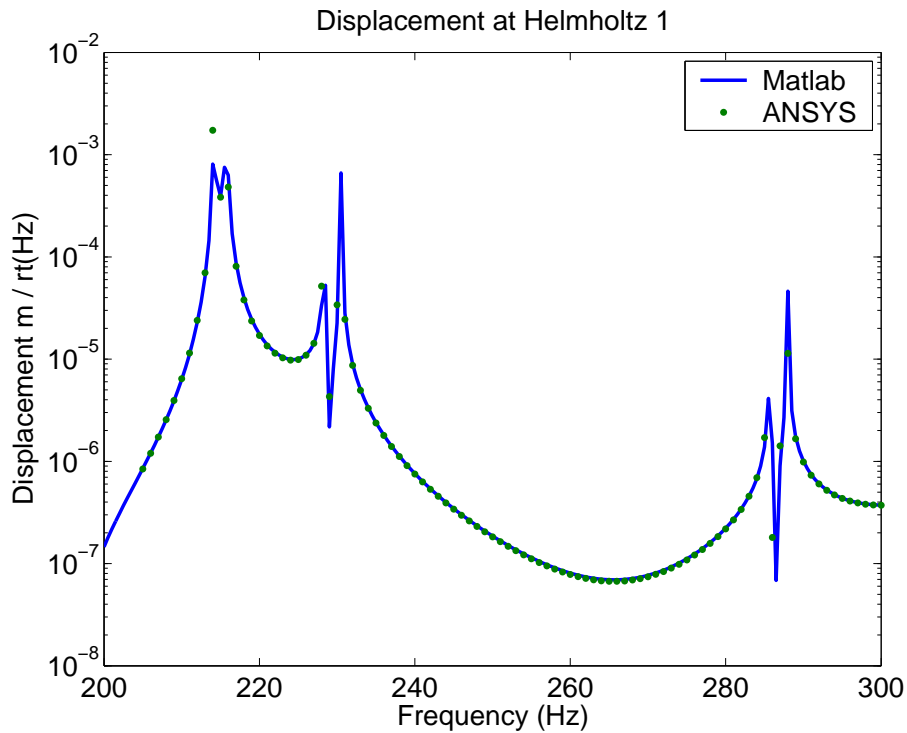


FIG. D.42: Stretch of the acoustic spring for Helmholtz resonator 1.

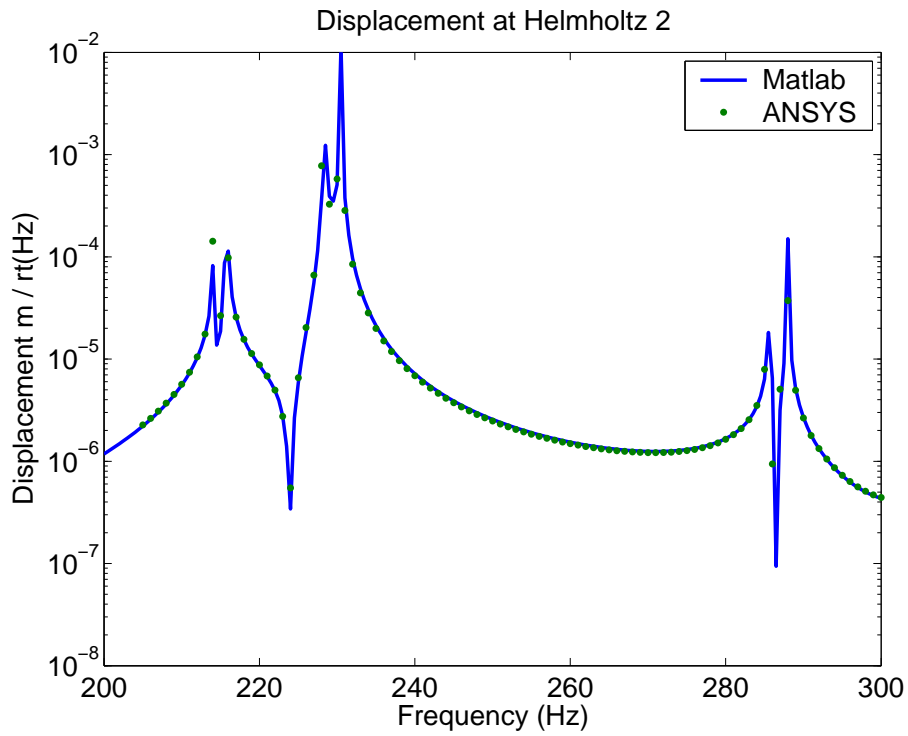


FIG. D.43: Stretch of the acoustic spring for Helmholtz resonator 2.

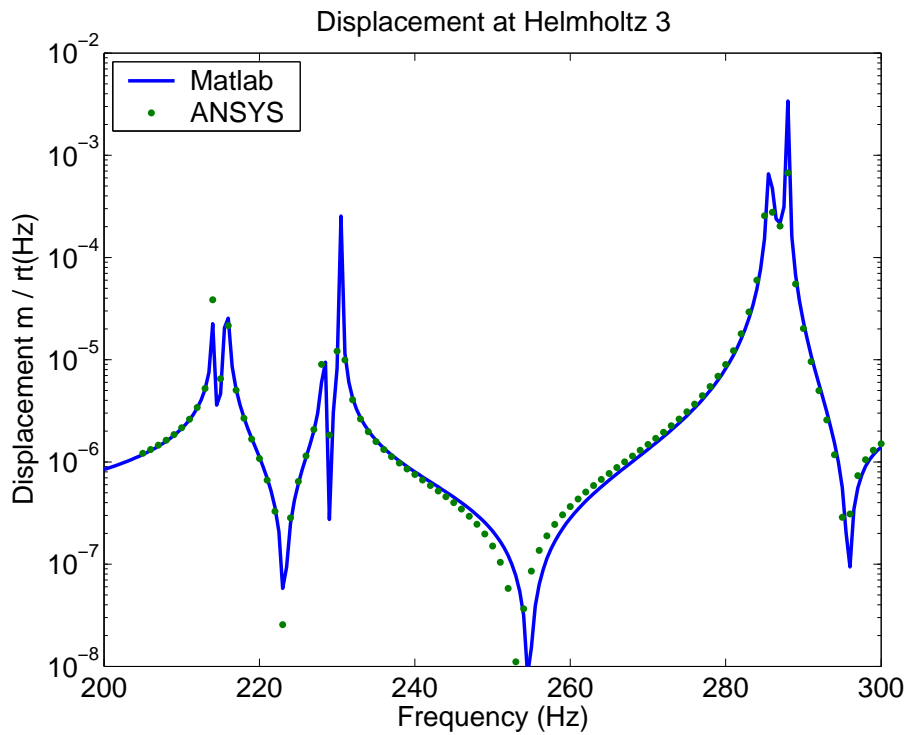


FIG. D.44: Stretch of the acoustic spring for Helmholtz resonator 3.

D.3.5 Placement of the device on the interior of the cavity

All the results discussed in this analysis and those in previous reports [3, 5] have concerned placement of the HR on the edge of the acoustic cavity, as it was assumed that there would be little difference in the results if the device were placed on the edge of the cavity, or slightly inside the cavity. The work done here shows a method of modelling the HR placed in the interior of the acoustic cavity.

There is a need to separate the location of the TMDs, which attached to the structure, and the HRs, which attach to the acoustic cavity, as the TMDs act to modify the vibration of the structure with additional stiffness and mass. Hence a HR which is modelled as a mass and spring element cannot be attached to a structural shell, and can only be attached to the acoustic cavity.

Figure D.45 shows the model of the cavity shown in Figure D.11, with four elements removed on the interior. This model is used to analyse the pressure distribution within the cavity when a FLOW boundary condition is applied to a node.

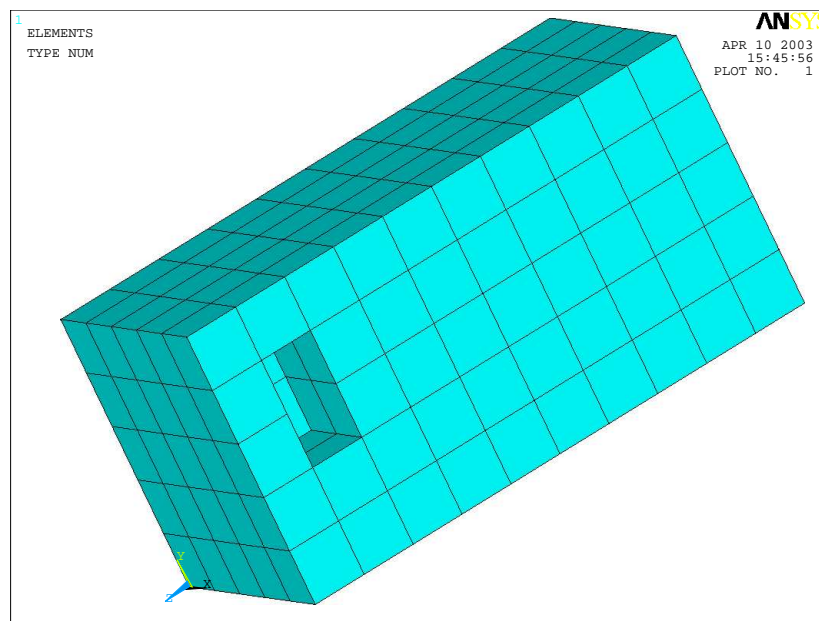


FIG. D.45: ANSYS model showing the 4 elements removed on the interior of the cavity.

Figure D.46 shows the ANSYS model where four FSI elements have been placed in front of the void. The node at the centre of these FSI elements is used to apply a harmonic volume displacement to the cavity.

Figure D.47 shows the pressure at the driving point, calculated using the three methods described in section D.3.1. Each method has a different result, which was explained in section D.3.1. The pressure was also calculated at the node directly in front of the driving point and at a remote location, and the results are shown in Figures D.48 and D.49, respectively.

The sum of the squared pressures at all the nodes is shown in Figure D.50 and shows that the three methods give the same results.

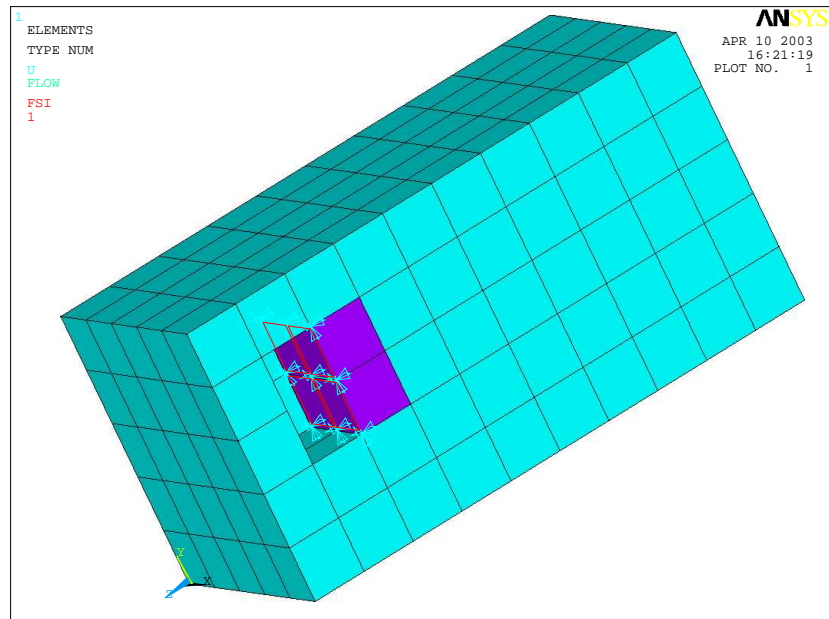


FIG. D.46: ANSYS model showing the four elements removed on the interior of the cavity, and the four FSI elements.

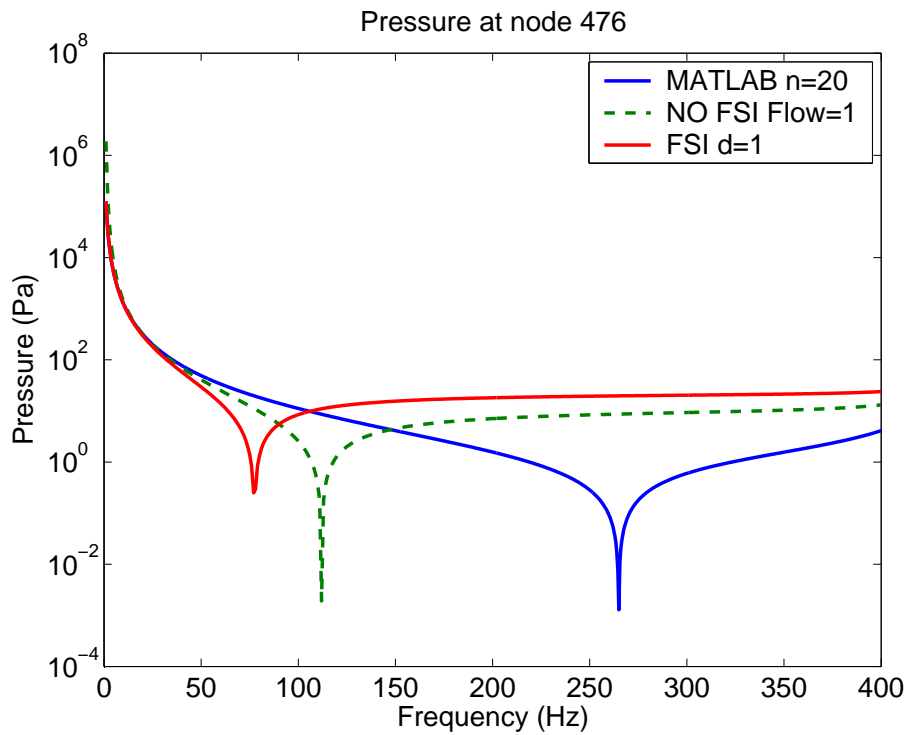


FIG. D.47: Pressure at the driving point for the three methods.

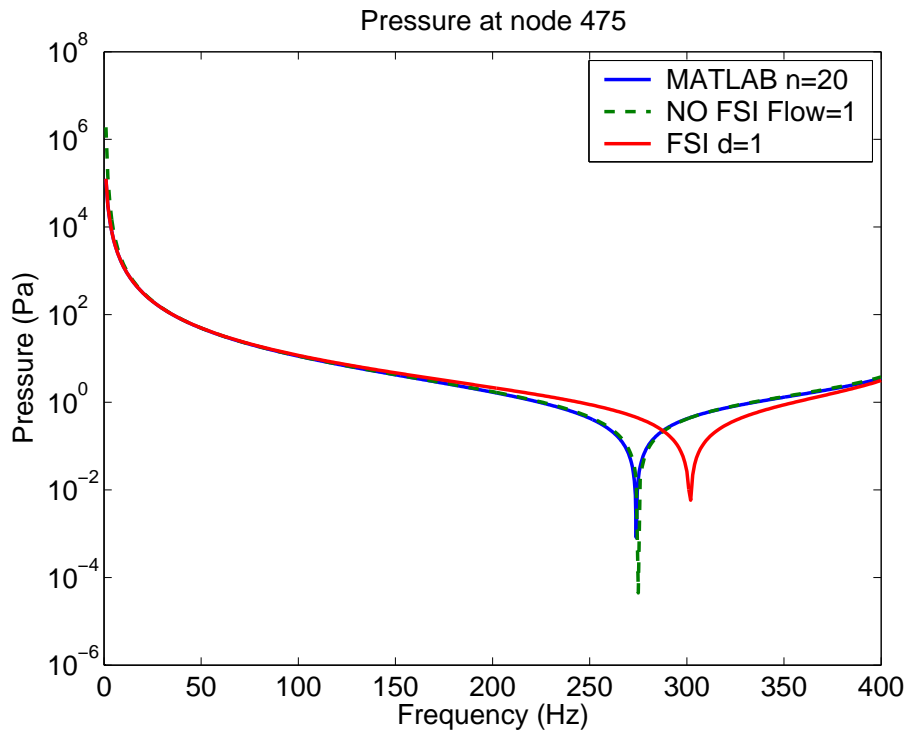


FIG. D.48: Pressure at a node directly in front of the driving point, for the three methods.

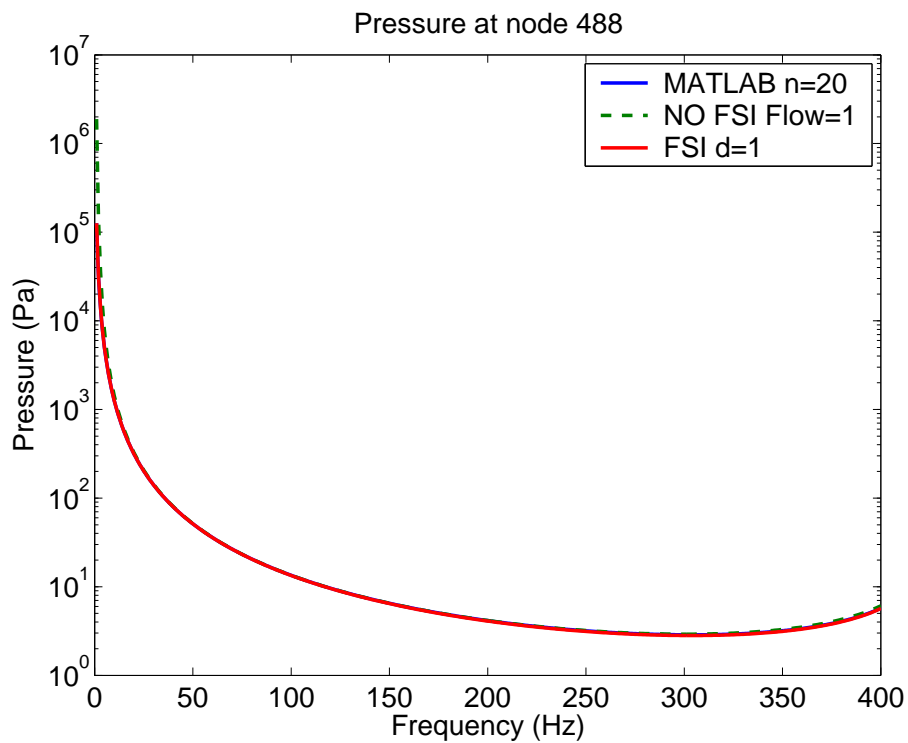


FIG. D.49: Pressure at a remote location for the three methods.

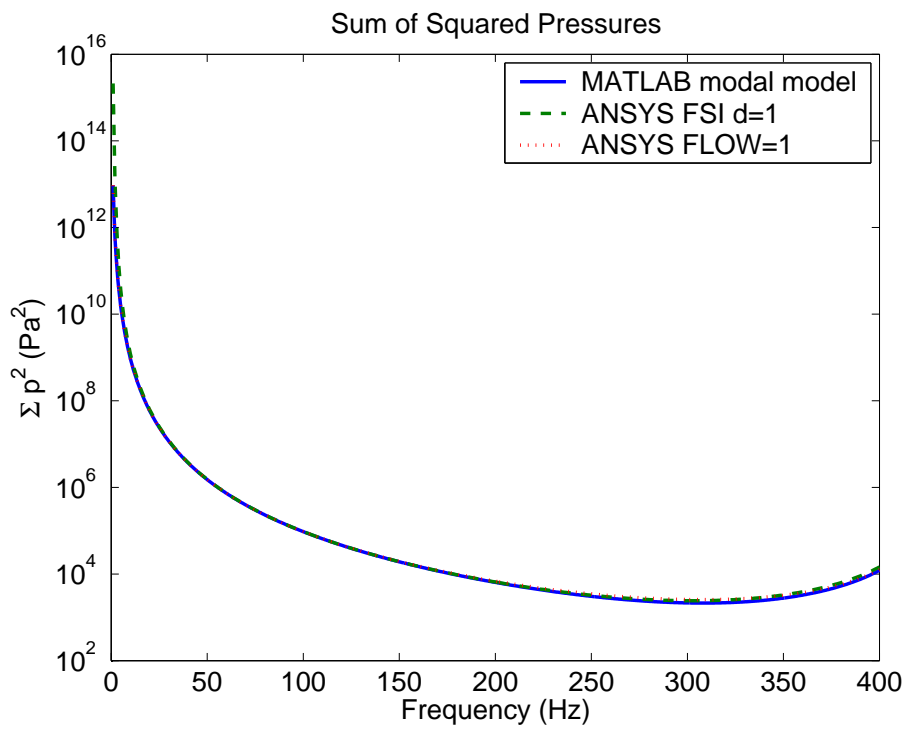


FIG. D.50: Sum of the squared pressures for the three methods.

D.4 Fully Coupled Model

Section 3.2 described a mathematical model to couple TMDs to a structure, and section 3.3 described a mathematical model to couple HRs to an acoustic cavity. The next step was to develop a mathematical model to couple both the TMDs and HRs to a vibro-acoustic system, which is described in section 3.4. The fully coupled vibro-acoustic model accounts for the influence of the TMDs on the structural vibration and the acoustic response, and will account for the the influence of the HRs on the acoustic response and the structural vibration.

This section describes the results from the comparison of the MATLAB modal coupling software with the results from an ANSYS model using fluid-structure interaction. The model was a rectangular cavity with dimensions $0.5 \times 0.3 \times 1.1\text{m}$ with a simply supported aluminium plate of 3mm thickness attached to one end of the cavity, as shown in Figure D.51. The boundary conditions applied to the panel are shown in Figure D.52. The sound pressure level at $(0.175, 0.18, 0.88)$, a random location within the cavity, was predicted using the ANSYS software, and compared with the modal coupling software and the results are shown in Figure D.53.

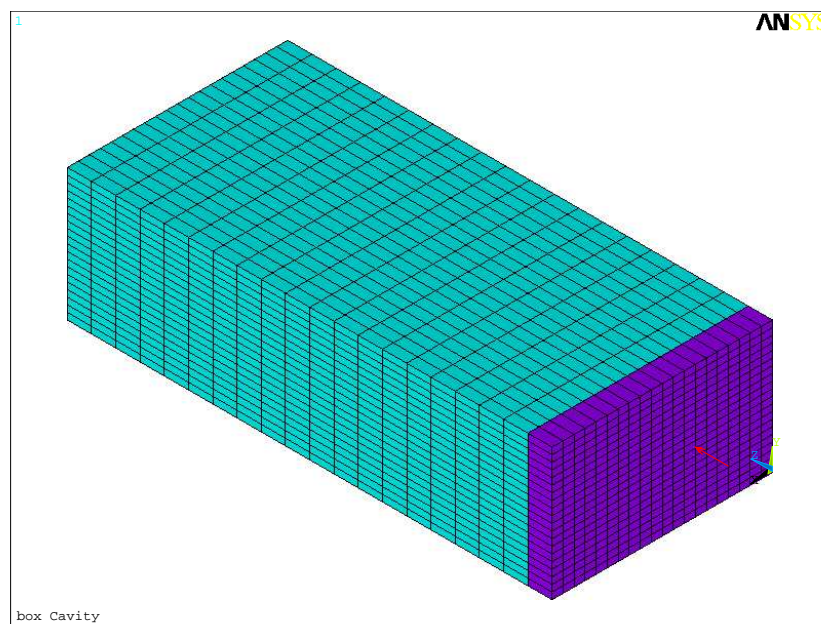


FIG. D.51: Picture of the ANSYS finite element model used for the comparison of the two methods.

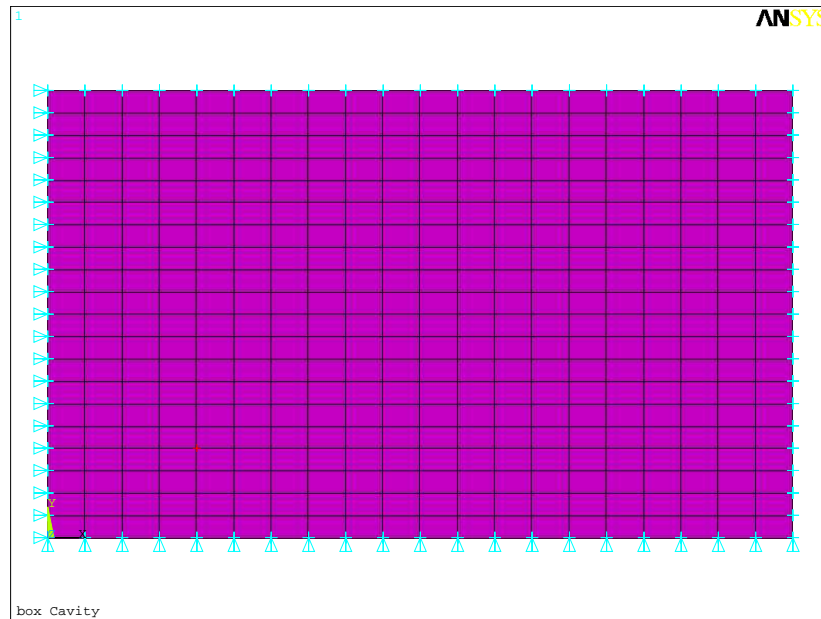


FIG. D.52: Picture of the ANSYS model of the plate that shows the boundary conditions on the edge of the plate.

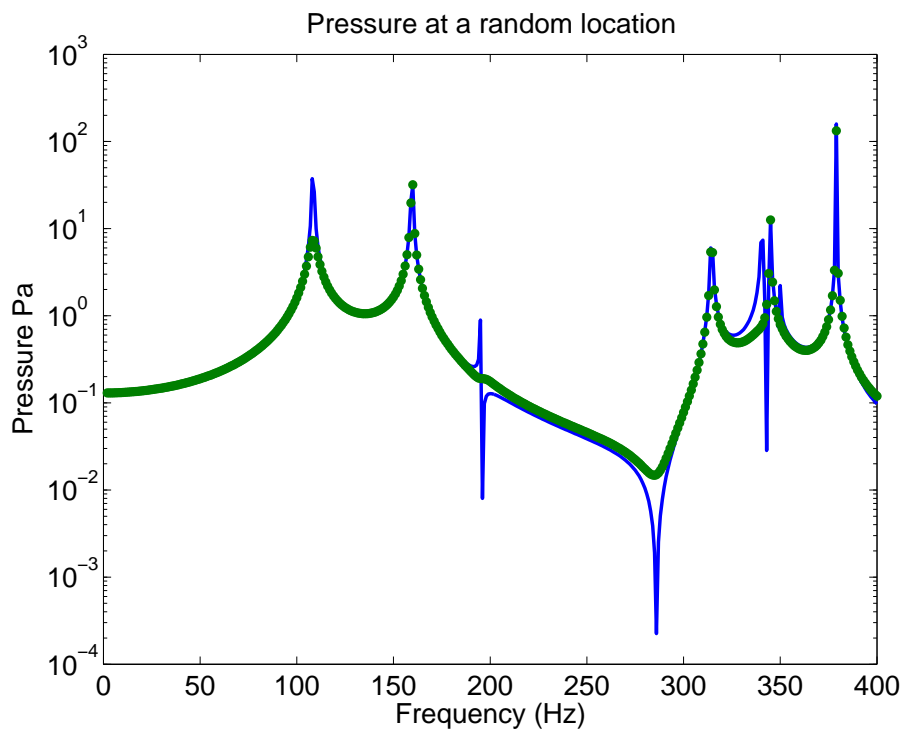


FIG. D.53: Sound pressure level at a random location within the cavity predicted using the MATLAB modal coupling and ANSYS software. The solid line are the Matlab results and the dots are the ANSYS results.

The material properties used in the analysis are listed in Table D.6.

Property	Value
Aluminium Youngs Modulus	70.9 GPa
Aluminium Density	2700 kg / m ³
Aluminium Thickness	3 mm
Air Density	1.21 kg / m ³
Air Speed of Sound	344 m/s

Table D.6: Material properties of the Aluminium and Air used in the models.

A similar ANSYS model was created with two Helmholtz resonators attached to the acoustic cavity and a single Tuned Mass Damper attached to the simply supported plate, as shown in Figure D.54. The average element size was 0.025m.

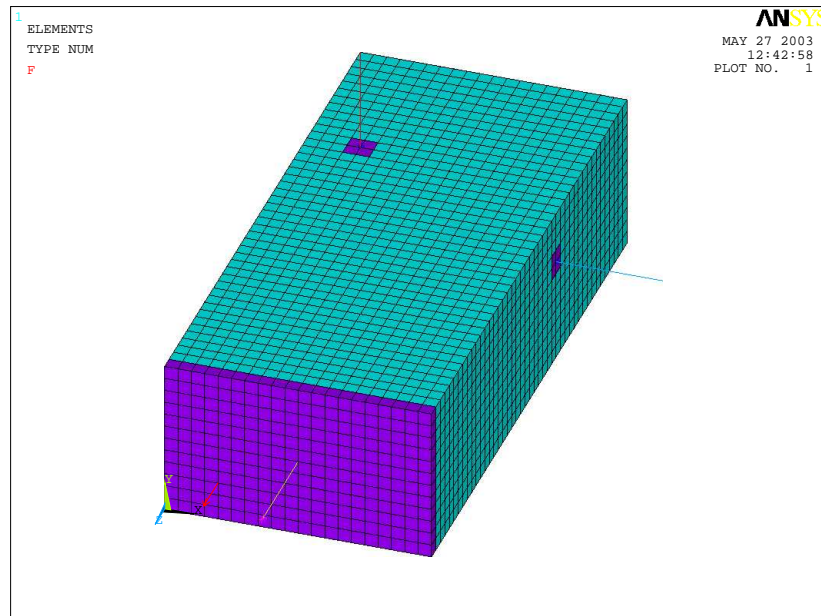


FIG. D.54: ANSYS model of a rectangular cavity showing the two Helmholtz resonators attached to the side walls, and the Tuned Mass Damper attached to the front of the box.

The properties of the HRs and TMD are listed in Table D.7.

Property	HR 1	HR 2	TMD 1
Stiffness	10081 N/m	39048 N/m	232375 N/m
Mass	0.01 kg	0.01 kg	0.5 kg
Frequency	159.8 Hz	314.5 Hz	108.5 Hz
Node	1696	3130	442
Location	(0.10, 0.30, -0.80)	(0.50, 0.20, -0.70)	(0.25, 0.15, 0.0)

Table D.7: Properties of the HR and TMD used in the testing of the fully coupled code.

The modal analysis portion of the coupling calculation extracted results up to 2000Hz, in which there were 187 cavity modes with the highest frequency being 1996Hz, and 26 structural modes with the highest frequency being 1960Hz.

Figure D.55 shows the sound pressure level evaluated at node 4793 (0.1, 0.05, -0.275) when a 1N force was applied to the plate at node 373 (0.10 , 0.075, 0.0). Figures D.56 and D.57 show the sound pressure level at the node that attaches to Helmholtz resonators 1 and 2, respectively. Figure D.58 shows the velocity at Tuned Mass Damper 1.

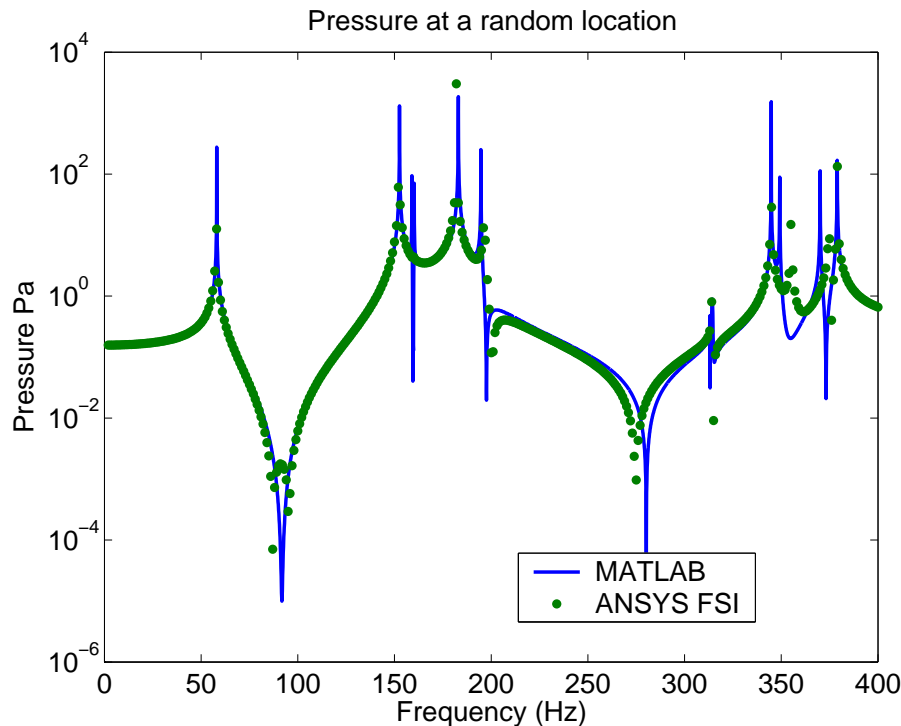


FIG. D.55: Pressure at a random location within the cavity for two Helmholtz resonators and one Tuned Mass Damper.

Figure D.59 shows the sound pressure level at (0.1, 0.05, -0.275), a random location within the cavity, for the MATLAB modal coupling and ANSYS FSI analyses, with and without the PVADs. The vertical dashed lines show the frequencies that were targeted by the two HRs and the single TMD.

The results in Figure D.59 indicate that the Matlab modal coupling software and the ANSYS FSI analyses are in good agreement. The results also indicate that the applied Helmholtz resonators and Tuned Mass Dampers have been effective in reducing the interior pressure within the cavity at the target frequencies.

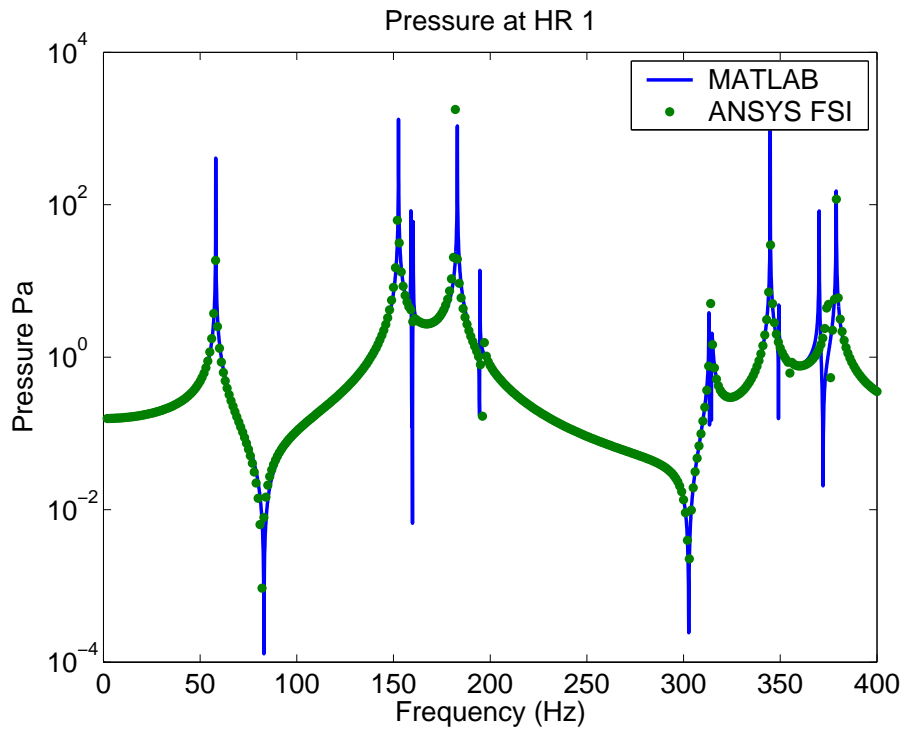


FIG. D.56: Pressure at Helmholtz resonator 1.

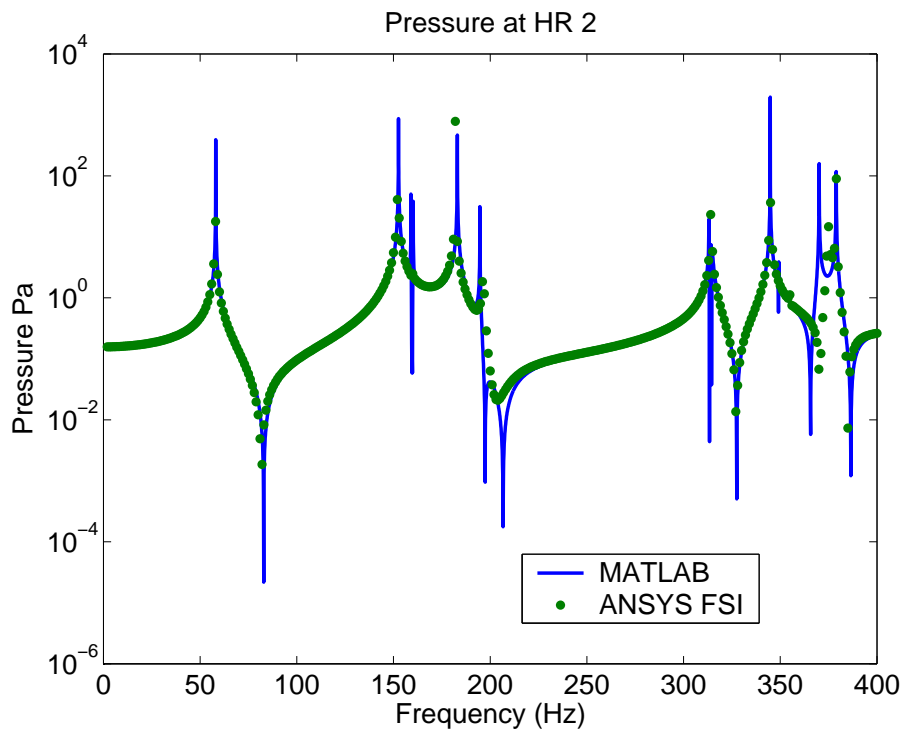


FIG. D.57: Pressure at Helmholtz resonator 2.

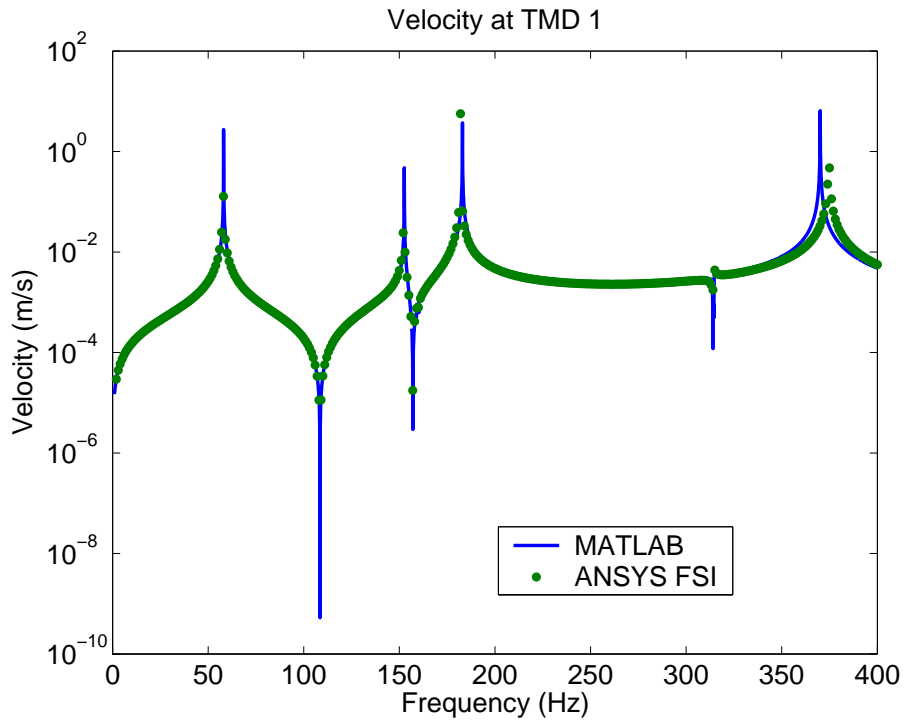


FIG. D.58: Velocity at Tuned Mass Damper 1.

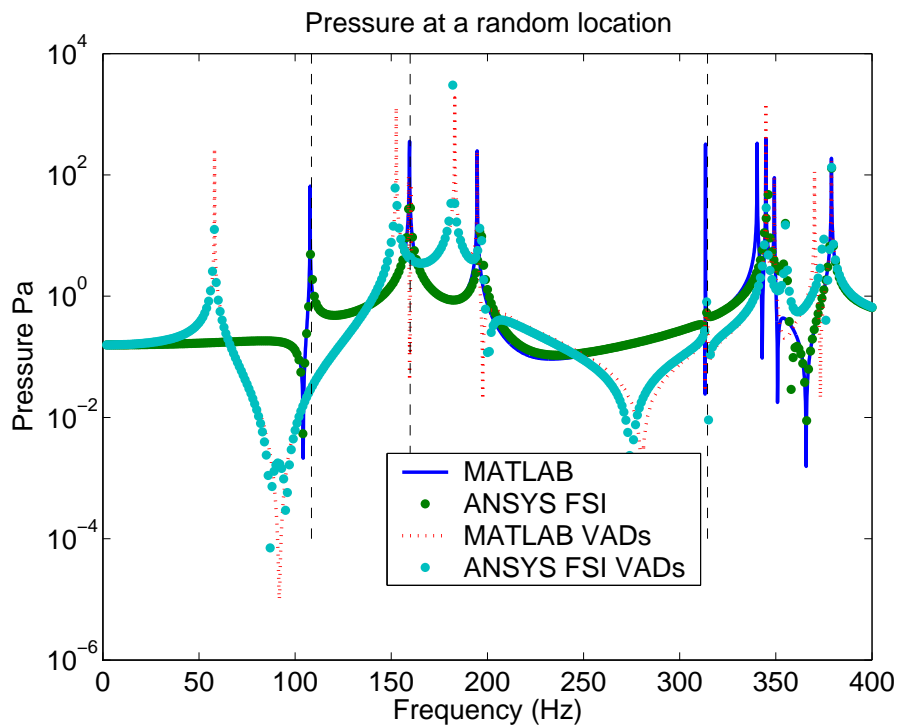


FIG. D.59: Pressure at a random location within the cavity, with and without the PVADs, for the MATLAB modal coupling and ANSYS FSI analyses.

D.5 Calculation of Acoustic Potential Energy

The acoustic potential energy is one method of evaluating the energy contained within a cavity and is given by [4]

$$E_p = \frac{1}{4\rho_0 c_0^2} \int_V |p(\vec{r})|^2 dV \quad (\text{D.3})$$

This can be implemented in a finite element formulation as

$$E_p = \frac{1}{4\rho_0 c_0^2} \sum_{i=1}^n p_n^2 V_n \quad (\text{D.4})$$

where p_n is the pressure at the n th node and V_n is the volume associated with the n th node. This equation can be re-arranged so that the acoustic potential energy is calculated in terms of the modal pressure amplitudes as

$$E_p = \sum_{i=1}^{\infty} \Lambda |p_i|^2 \quad (\text{D.5})$$

$$= \mathbf{p}^H \Lambda \mathbf{p} \quad (\text{D.6})$$

where Λ is a ($N_a \times N_a$) diagonal matrix of which the diagonal terms are

$$\Lambda(i, i) = \frac{\Lambda_i}{4\rho_0 c_0^2} \quad (\text{D.7})$$

where Λ_i is the modal volume of the i th cavity mode.

Figure D.60 shows the results for calculations using Eq. (D.4) and Eq. (D.6) and shows that the quicker method, the summation of the 20 modal amplitudes, gives the same results as the longer method, the calculation of all the nodal pressures at 594 nodes (which involves multiplication of the mode shape vector and modal amplitudes at each nodal location), squaring, and summing.

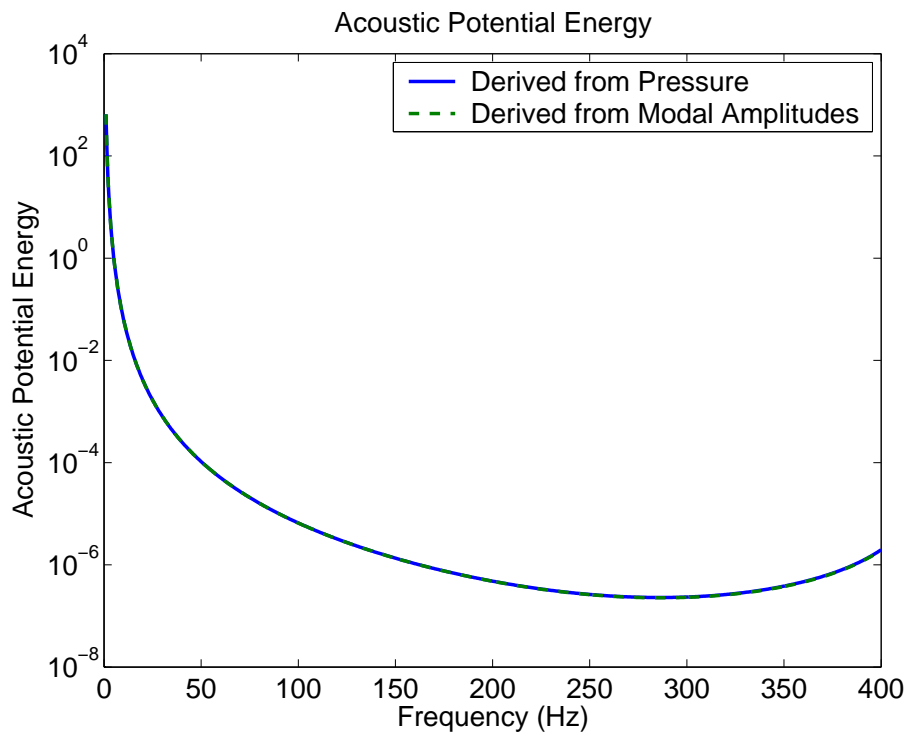


FIG. D.60: Calculation of the potential energy using two different methods.

Bibliography

- [1] Simon J Estéve and Marty E Johnson. Reduction of sound transmission into a circular cylindrical shell using distributed vibration absorbers and helmholtz resonators. *Journal of the Acoustical Society of America*, 112(6):2840–2848, December 2002.
- [2] Carl Q. Howard. *Active isolation of machinery vibration from flexible structures*. PhD thesis, Department of Mechanical Engineering, University of Adelaide, Adelaide, South Australia, Australia, 1999.
- [3] Colin Hansen, Anthony Zander, Ben Cazzolato, and Rick Morgans. Investigation of passive control devices for potential application to a launch vehicle structure to reduce the interior noise levels during launch: Final report for stage 1. Technical report, Department of Mechanical Engineering, University of Adelaide, Adelaide, S.A. 5000, Australia, November 2000.
- [4] Ben S. Cazzolato. *Sensing systems for active control of sound transmissino into cavities*. PhD thesis, Department of Mechanical Engineering, University of Adelaide, Adelaide, South Australia, Australia, 1999.
- [5] Colin Hansen, Anthony Zander, Ben Cazzolato, and Rick Morgans. Investigation of passive control devices for potential application to a launch vehicle structure to reduce the interior noise levels during launch: Final report for stage 2. Technical report, Department of Mechanical Engineering, University of Adelaide, Adelaide, S.A. 5000, Australia, November 2000.
- [6] Carl Q. Howard, Colin H. Hansen, and J. Q. Pan. Power transmission from a vibrating body to a circular cylindrical shell through active elastic isolators. *Journal of the Acoustical Society of America*, 101(3):1479–1491, 1997.
- [7] Leo L. Beranek and Istvan L. Ver, editors. *Noise and vibration control engineering. Principles and applications*. John Wiley and Sons, U.S.A., 1992.
- [8] David B. Woyak. *Ansys: Acoustics and Fluid Structure Interaction: a revision 5.0 tutorial*. Swanson Analysis Systems Inc., Houston, PA, USA, June 1992.
- [9] Steffen Marburg. Six boundary elements per wavelength: Is that enough? *Journal of Computational Acoustics*, 10(1):25–51, 2002.
- [10] David E. Goldberg. *Genetic algorithms in search, optimization, and machine learning*. Addison-Wesley, January 1989.

- [11] Parallel Genetic Algorithm Library - PGAPack.
<http://www-fp.mcs.anl.gov/>.
- [12] Genetic Algorithm Optimization Toolbox (GAOT) for Matlab 5.
<http://www.ie.ncsu.edu/mirage/GAToolBox/gaot/>.
- [13] The Condor Project Homepage.
<http://www.cs.wisc.edu/condor/>.
- [14] Matlab compiler.
<http://www.mathworks.com/products/compiler/>.
- [15] Genetic Algorithm Toolbox for Matlab.
<http://www.shef.ac.uk/~gaipp/ga-toolbox/>.
- [16] Timothy J. Stanley and Trevor Mudge. A Parallel Genetic Algorithm for Multiobjective Microprocessor Design. In Larry J. Eshelman, editor, *Proceedings of the Sixth International Conference on Genetic Algorithms*, pages 597–604, San Mateo, California, 1995. Morgan Kaufmann Publishers.
- [17] Andrew Chipperfield, Peter Fleming, Hartmut Pohlheim, and Carlos Fonseca. *Genetic Algorithm TOOLBOX, Users Guide V1.2*. The Department of Automatic Control and Systems Engineering of The University of Sheffield, UK, The University of Sheffield, Sheffield, UK.
- [18] Philip M. Gerhat and Richard J. Gross. *Fundamentals of Fluid Mechanics*. Addison-Wesley USA, 1985. ISBN 0201114100.
- [19] Jianmin Gu, Zheng-Dong Ma, and Gregory M. Hulbert. Quasi-static data recovery for dynamic analyses of structural systems. *Finite Elements in Analysis and Design*, 37:825–841, 2001.
- [20] You-qun Zhao, Su-huan Chen, San Chai, and Qing-wen Qu. An improved modal truncation method for responses to harmonic excitation. *Computers and Structures*, 80:99–103, 2002.
- [21] Michel Tournour and Nouredine Atalla. Pseudostatic corrections for the forced vibroacoustic response of structure- cavity system. *Journal of the Acoustical Society of America*, 107(5):2379–2386, May 2000.
- [22] V. B. Bokil and U. S. Shirahatti. A technique for the modal analysis of sound-structure interaction problems. *Journal of Sound and Vibration*, 173(1):23–41, 1994.